

THESIS

DESIGN, FABRICATION, AND DEMONSTRATION OF LOW-MASS, LOW-POWER,
SMALL-VOLUME, DIRECT DETECTION MILLIMETER-WAVE RADIOMETERS AT
92 AND 130 GHZ

Submitted by

Darrin Albers

Department of Electrical and Computer Engineering

In partial fulfillment of the requirements

For the Degree of Master of Science

Colorado State University

Fort Collins, Colorado

Spring 2012

Master's Committee:

Advisor: Steven C. Reising

Christian Kummerow

Branislav Notaros

Pekka Kangaslahti

ABSTRACT

DESIGN, FABRICATION, AND DEMONSTRATION OF LOW-MASS, LOW-POWER, SMALL-VOLUME, DIRECT DETECTION MILLIMETER-WAVE RADIOMETERS AT 92 AND 130 GHZ

Advances in future ocean satellite altimetry missions are needed to meet oceanographic and hydrological objectives. These needs include accurately determining the sea surface height (SSH) on spatial scales of 10 km and larger, as well as monitoring the height of the world's inland bodies of water and the flow rate of rivers. The Surface Water and Ocean Topography (SWOT) mission was recommended by the National Research Council's Earth Science Decadal Survey and selected by the National Aeronautics and Space Administration as an accelerated Tier-2 mission to address these needs. Current surface altimetry missions use nadir pointing 18-37 GHz microwave radiometers to correct for errors in SSH due to wet-tropospheric path delay. Using current antennas at these frequencies, oceanic measurements include significant errors within 50 km of coastlines due to varying emissivity and temperature of land. Higher frequencies (90-170 GHz) can provide proportionally smaller footprints for the same antenna size. In turn, this provides improved retrievals of wet-tropospheric path delay near the coasts.

This thesis will focus on the design, fabrication, and testing of two direct detection radiometers with internal calibration at center frequencies of 92 and 130 GHz. Component design, testing and integration of the radiometers using multi-chip modules are discussed. The

performance of these radiometers is characterized, including noise figure, internal calibration and long-term stability. These performance parameters, along with their mass, volume, and power consumption, will be used as the basis for the development of future airborne and space-borne millimeter-wave direct detection radiometers with internal calibration.

ACKNOWLEDGEMENTS

First and foremost, I would like to express my gratitude to Dr. Steven C. Reising, my advisor, for providing me this learning experience as well as his guidance and high expectations. Secondly, I would like to thank Dr. Branislav Notaros and Dr. Chris Kummerow for their scientific suggestions and serving on my thesis committee.

I am deeply grateful to the National Aeronautic and Space Administration's Earth Science and Technology Office for providing this research opportunity as well as the contributions of our collaborators at the Jet Propulsion Laboratory. I especially would like to thank Dr. Pekka Kangaslahti and Douglas Dawson for their insightful suggestions as well as Mary Soria for her technical assembly experience without which these radiometers would not have been possible. Current and past students of the Microwave Systems Laboratory at Colorado State University have contributed to this work. I would especially like to thank Alexander Lee for his collaboration on the 92 GHz radiometer. Also, I am grateful for the assistance of Dr. Xavier Bosch, Swaroop Sahoo, Kyle Gilliam, Scott Nelson, Thaddeus Johnson, and Daniel Higley.

Darrin Albers

DEDICATION

To my parents, Ivo and Therese.

TABLE OF CONTENTS

ABSTRACT	ii
ACKNOWLEDGEMENTS	iv
DEDICATION	v
TABLE OF CONTENTS.....	vi
LIST OF FIGURES	xii
LIST OF TABLES	xxii
Chapter 1 Introduction.....	1
1.1 Surface Water and Ocean Topography (SWOT) Mission Background.....	1
1.2 Sea Surface Altimetry	2
1.3 Microwave Radiometer Fundamentals.....	6
1.3.1 Principles	6
1.3.2 Comparison of Direct Detection and Superheterodyne Architectures	7
1.3.3 Comparison of Total Power and Dicke Radiometers	9
1.3.4 Comparison of External and Internal Calibration.....	12
1.4 Technology Objectives for Millimeter-wave Radiometer Development.....	14
1.4.1 Tri-Frequency Feed Horn	14
1.4.2 PIN-Diode Switches at 92, 130, 166 GHz.....	15

1.4.3	Noise Sources at 92, 130, and 166 GHz	17
1.4.4	MMIC-Based Radiometers at 92, 130, and 166 GHz.....	18
Chapter 2	92 GHz Radiometer Design and Test	19
2.1	Block Diagram	19
2.2	Predicted Noise Temperature and Radiometric Resolution	20
2.3	Gain Requirements.....	24
2.4	Commercially-Available Components.....	27
2.4.1	ELVA Coupler.....	27
2.4.2	M/A-Com PIN-diode Switch.....	28
2.4.3	HRL LNA	30
2.4.4	HRL Detector	31
2.5	Components Designed at JPL	32
2.5.1	Tri-Frequency Feed Horn	32
2.5.2	Noise Source.....	32
2.5.3	PIN-Diode Switch.....	32
2.6	Components Designed at CSU MSL.....	33
2.6.1	Waveguide-to-Microstrip Transition Design.....	33
2.6.1.1	Design.....	34
2.6.2	Matched Load	36
2.6.2.1	Virtual Ground Design	36

2.6.2.2	Virtual Ground Measurement	37
2.6.2.3	Ground Via Matched Load Design.....	40
2.6.2.4	Ground Via Matched Load Measurement	40
2.6.3	Edge-Coupled Bandpass Filter	42
2.6.3.1	Design	42
2.6.3.2	Measurement	44
2.6.3.3	Test Fixture.....	46
2.6.4	Attenuator	48
2.6.4.1	Design.....	49
2.6.4.2	Measurement	50
2.6.5	Multi-Chip Module Design and Assembly.....	52
2.7	Testing.....	55
2.7.1	Mass, Volume and Power Consumption	56
2.7.2	Multi-Chip Module Bias Boards	57
2.7.3	Data Acquisition and Control System	60
2.7.3.1	Video Gain and Detection	61
2.7.3.2	Drain and Gate Biasing.....	62
2.7.4	Thermal Control	63
2.7.5	Results	67
2.7.5.1	Measured Receiver Noise Temperature	68

2.7.5.2	Internal Calibration.....	70
2.7.6	Long Term Radiometer Stability.....	76
2.7.6.1	Allan Deviation.....	77
Chapter 3	130 GHz Radiometer Design and Test	80
3.1	Block Diagram	80
3.2	Predicted Noise Temperature and Radiometric Resolution	81
3.3	Gain Requirements.....	83
3.4	Commercially Available Components	84
3.4.1	ELVA Coupler.....	84
3.4.2	Pacific Millimeter Products Detector	85
3.5	Components Designed at JPL	87
3.5.1	Tri-Frequency Feed Horn	87
3.5.2	Noise Source.....	87
3.5.3	PIN-Diode Switch.....	87
3.5.4	LNA.....	88
3.6	Components Designed at CSU MSL.....	89
3.6.1	Waveguide-to-Microstrip Transition Design.....	89
3.6.2	Matched Load with Virtual Ground – Design and Measurement	92
3.6.3	Interconnects and Interconnect Attenuators	94
3.6.3.1	Interconnect Design and Measurement	94

3.6.3.2	Interconnect Attenuator Design and Measurement	96
3.6.4	Narrow Edge-Coupled Bandpass Filter	98
3.6.4.1	Design and Optimization	98
3.6.4.2	Measurement	102
3.6.5	Wide Edge-Coupled Bandpass Filter – Design and Measurement.....	105
3.6.6	Attenuator – Design and Measurement	108
3.6.6.1	Multi-Chip Module Design and Assembly.....	110
3.7	Testing.....	114
3.7.1	Mass, Volume and Power Consumption	114
3.7.2	Multi-Chip Module Bias Board.....	116
3.7.3	Thermal Control	117
3.7.4	Results	122
3.7.4.1	Measured Receiver Noise Temperature	122
3.7.4.2	Internal Calibration.....	125
3.7.5	Long Term Radiometer Stability.....	126
3.7.5.1	Allan Deviation.....	126
Chapter 4	Summary and Future Work.....	130
4.1	Ocean Altimetry and Wet-tropospheric Path Delay.....	130
4.2	92 GHz Radiometer.....	131
4.3	130 GHz Radiometer.....	131

4.4	Future Work	132
Appendix A	MMIC Assembly	139
Appendix B	Backend Board I	144
Appendix C	User Interface	148
Appendix D	Bandpass Filter Design	151
D.1	Center BPF for HFSS.....	152
D.2	Offset BPF for HFSS	157
Appendix E	92 GHz Radiometer	161
E.1	Passive Components	162
E.2	92 GHz Bias Boards.....	166
E.3	Temperature Control Module Settings.....	168
Appendix F	130 GHz Radiometer	169
F.1	Passive Components	170
F.2	130 GHz Bias Board	174
F.3	Temperature Control Module Settings.....	175
Appendix G	Base Data acquisition and control PCB	176
	List of Abbreviations	185

LIST OF FIGURES

1.1: Principles of altimetry.....	3
1.2: Atmospheric attenuation as a function of frequency.	4
1.3: Wet path delay error using a high resolution WRF model for both low frequency (18-37 GHz) and high-frequency (90-170 GHz) radiometer channels.	5
1.4: Direct Detection Architecture.....	8
1.5: Superheterodyne Architecture.....	8
1.6: Total Power Radiometer Diagram.....	10
1.7: Dicke Radiometer Diagram.....	10
1.8: Assembled tri-frequency feed horn for the SWOT ACT.....	15
1.9: Diagram of switch topologies with asymmetric (<i>left</i>) and symmetric (<i>right</i>).	16
1.10: Block diagram of the tri-frequency radiometer with 92, 130, and 166 GHz center frequencies.	18
2.1: Block diagram of a direct detection Dicke radiometer with internal calibration.....	19
2.3: Radiometric resolution for the 92 GHz radiometer using theoretical component values with 727 K noise temperature and 5 GHz bandwidth.....	22
2.4: Radiometric resolution for the 92 GHz radiometer using measured component values with 1545 K noise temperature and 6.8 GHz bandwidth.....	24
2.5: W-band ELVA 10 dB directional coupler.	27
2.6: Insertion loss of the W-band ELVA coupler.	28
2.7: Coupling of the W-band ELVA coupler.....	28

2.8: Measurement test configuration for M/A-COM PIN-diode switch.....	29
2.9: Measured insertion loss of the 77 GHz M/A-COM PIN-diode switch for W-band.	29
2.10: 92 GHz MMIC LNA from HRL.....	30
2.11: 92 GHz MMIC zero bias power detector from HRL.....	31
2.12: 92 GHz asymmetric SPDT pin diode switch with integrated matched load and radial stub tuning to improve isolation. [13].....	33
2.13: 92 GHz waveguide-to-microstrip transition.	35
2.14: Input return loss of 92 GHz waveguide-to-microstrip transition.....	35
2.15: 92 GHz waveguide-to-microstrip transition insertion loss.....	36
2.16: HFSS 3D Model of 92GHz 50 Ω matched load with virtual ground.	37
2.17: 50 Ω load with virtual ground measurement configuration.....	38
2.18: Comparison among HFSS cavity simulation, HFSS open air simulation, and measured result for the 50 Ω load with virtual ground.	39
2.19: HFSS 3D Model of 92 GHz 50 Ω matched load with ground vias.	40
2.20: 50 Ω load with ground vias measurement configuration.....	41
2.21: Comparison among HFSS cavity simulation, HFSS open air simulation, and measured result for the 50 Ω load with virtual ground.	41
2.22: HFSS 3D Model of 92GHz BPF.....	43
2.23: 92 GHz bandpass filter measurement configuration.....	44
2.24: Comparison of the input return loss among HFSS open air simulation, HFSS cavity simulation, and open air measurement.....	44
2.25: Comparison of the insertion loss among HFSS open air simulation, HFSS cavity simulation, and open air measurement.....	45

2.26: A close-up view of the bottom half of the BPF test fixture.	46
2.27: Waveguide bandpass filter input return loss measurement compared to Ansoft Designer cascaded components simulation.	47
2.28: Waveguide bandpass filter insertion loss measurement compared to Ansoft Designer cascaded components simulation.	48
2.29: HFSS 3D model of 2 dB distributed attenuator.	50
2.30: 92GHz 2 dB attenuator used for measurements.	51
2.31: Comparison of input return loss for 2 dB attenuator for HFSS cavity, HFSS open air, and open air measurements.	51
2.32: HFSS cavity and HFSS open air simulations compared with open air measurements for the insertion loss of the 2 dB attenuator.	52
2.33: Bottom half of the 92 GHz MCM clamshell with one LNA and MMCX connectors.	52
2.34: 92 GHz MCM model.	53
2.35: 92 GHz radiometer, loaded RF trench with 2 LNAs and arrows pointing to a pressure ridge.	54
2.36: Dimensions of the 92 GHz radiometer.	56
2.37: 92 GHz LNA biasing trench with PCB bond pads (red) and capacitors (blue).	57
2.38: Video Board schematic for PCB in the 92 GHz MCM	59
2.39: Data acquisition and controller board (<i>left</i>) and SAM3U-EK (<i>right</i>).	60
2.40: Block Diagram of the data acquisition and control system for the 92 GHz radiometer.	61
2.41: 92 GHz radiometer test setup with thermal control.	64

2.42: Long term 92 GHz matched load equivalent noise temperatures using previous calibration coefficients.....	65
2.43: Long term 92 GHz MCM, PCB, and noise diode temperature data as well as drain current measurements. ³	66
2.44: 92 GHz radiometer configuration used for testing, without thermal control.....	67
2.45: 92 GHz testing without thermal control.	68
2.46: $NE\Delta T$ for the 92 GHz radiometer based upon measured receiver noise temperature.	70
2.47: 92 GHz noise diode temperature with error bars. ³	72
2.48: LN ₂ temperature based upon internal calibration with error bars. ³	72
2.49: Comparison between the measured equivalent noise temperature of the noise diode and that of the LN ₂ absorber.	73
2.50: Comparison between the physical temperature of the MCM and the matched load brightness temperature.....	74
2.51: Comparison between the physical temperature of the MCM and the noise diode temperature.	75
2.52: Comparison between the noise diode physical temperature and the cold absorber temperature.	76
2.53: MCM physical temperature data for Region 3 matched load data.	77
2.54: Noise diode and PCB temperature data for Region 3 matched load data. ⁴	77
2.55: Matched load equivalent noise temperature using previous calibration coefficients for Allan deviation analysis.	78
2.56: Allan deviation of matched load equivalent noise temperatures in 2.54. ⁵	79

3.1: Block diagram of the 130 GHz radiometer.....	80
3.2: Realistic radiometric resolution plot for the 130 GHz radiometer using 1328 K and a 5.25 GHz bandwidth.	83
3.3: 130 GHz 10-dB waveguide directional coupler from ELVA.....	84
3.4: Insertion loss of the 130 GHz ELVA 10 dB coupler.....	85
3.5: Coupling factor in dB of 130 GHz ELVA 10 dB coupler	85
3.6: 130 GHz zero bias waveguide detector with negative voltage output.....	86
3.7: 90-135 GHz symmetric MMIC PIN-diode switch design [13].	88
3.8: Gain and noise measurements for 140LNA [22].....	89
3.9: 130 GHz waveguide-to-microstrip probe transition	90
3.10: HFSS simulation of input return loss of the 130 GHz waveguide-to-microstrip probe transition with wire bond to alumina substrate.....	91
3.11: HFSS simulation of insertion loss of the 130 GHz waveguide-to-microstrip probe transition with wire bond to alumina substrate.....	92
3.12: 130 GHz matched load with virtual ground measurement configuration.....	92
3.13: 130 GHz matched load comparison of the input return loss between open air measured, HFSS open air simulation, and HFSS cavity results.	93
3.14: HFSS model of 130 GHz interconnect with wire bonds for simulation purposes. 95	
3.15: Input return loss comparison between the cavity and open air HFSS simulations of the 130 GHz interconnects.....	95
3.16: Insertion loss comparison between the cavity and open air HFSS simulations of the 130 GHz interconnects.....	96

3.17: Measurement setup of the 130 GHz narrow bandpass filter with interconnect attenuators circled in red.	97
3.18: HFSS cavity and open air simulation comparison of the input return loss for the 130 GHz interconnect attenuators.	97
3.19: HFSS cavity and open air simulation comparison to the de-embedded measured results of the insertion loss for the 130 GHz interconnect attenuators.	98
3.20: HFSS 3-D model of 130 GHz narrow bandpass filter.	99
3.21: Centered coupled line topology (left) and offset coupled line topology (right). .	101
3.22: Measurement configuration of the 130 GHz narrow bandpass filter.	103
3.23: Input return loss comparison between HFSS simulations and measured results for the 130 GHz narrow bandpass filter.	103
3.24: Insertion loss comparison between HFSS simulations and measured results for the 130 GHz narrow bandpass filter.	104
3.25: Zoomed in view of the insertion loss comparison between HFSS simulations and measured results for the 130 GHz narrow bandpass filter.	104
3.26: Measurement configuration of the 130 GHz narrow BPF with interconnect attenuators for improving matching and reducing gain.	105
3.27: Input return loss comparison between measured 130 GHz narrow bandpass filter with and without interconnect attenuators.	105
3.28: Measurement configuration of the 130 GHz wide bandpass filter.	106
3.29: Input return loss comparison between HFSS simulations and measured results for the 130 GHz wide bandpass filter.	106

3.30: Insertion loss comparison between HFSS simulations and measured results for the 130 GHz wide bandpass filter.....	107
3.31: Insertion loss of wide and narrow bandpass filters at 130 GHz.	108
3.32: Measurement configuration of the 130 GHz attenuator.	109
3.33: Input return loss comparison for the 130 GHz attenuator between the HFSS cavity simulation, HFSS open air simulation, and the measured component.	109
3.34: Insertion loss comparison for the 130 GHz attenuator among the HFSS cavity simulation, HFSS open air simulation, the measured component, and the measured corrected.....	110
3.35: 130 GHz MCM clamshell.....	111
3.36: Unloaded view of the bottom (left) and top (right) halves of the 130 GHz clamshell with a dime for reference.....	111
3.37: Zoomed in 3D CAD model of the 130 GHz MCM RF trench.	112
3.38: Assembled 130 GHz RF trench.	113
3.39: Zoomed view of the loaded RF trench in the bottom clamshell of the 130 GHz.	114
3.40: Photo of 130 GHz radiometer with a matched load on the coupled port and active thermal control.	115
3.41: Diagram of 130 GHz radiometer dimensions.	115
3.42: Loaded bottom clamshell of the 130 GHz MCM.	117
3.43: Thermal setup of the 130 GHz radiometer with insulating foam and Peltier control system.	118
3.44: MCM temperature data of 130 GHz MCM.	119

3.45: Temperature and drain current data for 16 hours of looking at room temperature microwave absorber. ⁶	120
3.46: Cold microwave absorber data.	121
3.47: Room temperature microwave absorber temperatures. ⁸	122
3.48: 130 GHz radiometric resolution in total power mode based on the measured receiver noise temperature of 1320 K and a 5.25 GHz bandwidth.	124
3.49: 130 GHz noise diode temperature. ⁹	126
3.50: Matched load equivalent noise temperatures using previous calibration coefficients for the 130 GHz radiometer.	127
3.51: Allan deviation of 130 GHz radiometer while viewing the matched load. ¹⁰	127
3.52: Warm microwave absorber brightness temperatures using previous calibration coefficients for the 130 GHz radiometer.	128
3.53: Allan deviation of the 130 GHz radiometer while viewing a warm microwave absorber. ¹¹	128
3.54: Allan deviation of the 130 GHz radiometer in Dicke mode.	129
A.1: Center BPF dimension variables for Ansoft HFSS.....	152
A.2: Center BPF position coordinates for Ansoft HFSS.	153
A.3: Offset BPF dimension variables for Ansoft HFSS.	157
A.4: Offset BPF position coordinates for Ansoft HFSS.....	158
B.1: Waveguide-to-Microstrip.....	162
B.2: 50Ω matched load with ground vias	163
B.3: 50 Ω matched load with virtual ground	163

B.4: Bandpass filter.....	164
B.5: 2 dB attenuator	164
B.6: 3 dB attenuator	164
B.7: 4 dB attenuator	165
B.8: 92 GHz MCM bias board with video gain. Green circle not implemented in layout of ordered PCB.	166
B.9: 92 GHz MCM bias board with LNA drain and gate bias as well as switch bias. ..	167
B.10: 92 GHz MCM bias board with switch bias.....	167
B.11: TCM settings for 92 GHz radiometer.	168
C.1: Waveguide-to-microstrip	170
C.2: Matched load with virtual grounds and TaN resistors of 50 Ω /sq	170
C.3: Interconnect.....	171
C.4: Interconnect with attenuation and TaN resistors of 100 Ω /sq.....	171
C.5: 5 GHz bandpass filter.....	171
C.6: 10 GHz bandpass filter.....	172
C.7: Attenuator with TaN resistors of 25 Ω /sq	172
C.8: Right angle bend	173
C.9: Transmission line	173
C.10: 130 GHz MCM bias board.....	174
C.11: TCM settings for 130 GHz radiometer.	175
D.1: Page 0 of data acquisition PCB.....	177
D.2: Page 1 of data acquisition PCB.....	178
D.3: Page 2 of data acquisition PCB.....	179

D.4:Page 3 of data acquisition PCB.....	180
D.5: Page 4 of data acquisition PCB.....	181
D.6: Page 5 of data acquisition PCB.....	182
D.7: Page 6 of data acquisition PCB.....	183
D.8: Page 7 of data acquisition PCB.....	184

LIST OF TABLES

2.1: Noise analysis for the 92 GHz radiometer using theoretical component values.	20
2.2: Noise analysis for the 92 GHz radiometer using measured component values.	23
2.3: Calculated power at the input of the power detector of the 92 GHz radiometer for the original design.	25
2.4: Calculated power at the input of the power detector of the 92 GHz radiometer for the final design.	26
2.5: Power and mass of the 92 GHz radiometer.	57
2.6: Y-factor measurements for the 92 GHz radiometer.	69
2.7: Internal calibration for the 92 GHz radiometer. ³	71
3.1: Final 130 GHz radiometer theoretical noise analysis based upon measured component values.	82
3.2: Input power calculation to the power detector of the 130 GHz radiometer based upon implemented and measured radiometer component configuration and values.	84
3.3: Theoretical bandpass filter calculations for a center frequency of 130 GHz.	100
3.4: Power and mass analysis of the 130 GHz radiometer.	116
3.5: Receiver noise temperature measurements for the 130 GHz radiometer using the Y-factor method.	123
3.6: Receiver noise temperature summary for the 130 GHz radiometer. ⁸	124
3.7: 130 GHz calculated noise diode temperature.	125

Chapter 1

Introduction

1.1 Surface Water and Ocean Topography (SWOT) Mission Background

The future National Aeronautics and Space Administration (NASA) Surface Water and Ocean Topography (SWOT) mission was recommended in the National Research Council's (NRC) 2007 Decadal Survey: "Earth Science and Applications from Space: National Imperatives for the Next Decade and Beyond." In June 2010, the SWOT mission was selected as one of two accelerated Tier 2 missions for a potential launch in 2013-2016. The mission has two main scientific objectives in oceanography and hydrology. The main oceanographic objective is to characterize mesoscale and submesoscale circulation at spatial resolution of 10 km and larger in order to aid in the understanding of heat and carbon exchange between the ocean and atmosphere [1]. This scale is necessary since these phenomena occur at scales smaller than 100 km. Current measurements are at resolutions of 300 km. The primary hydrological objectives involve a survey of the storage capacity of all terrestrial water bodies such as lakes, reservoirs, and wetlands which have areas greater than 250 m² and rivers with widths of at least 100 m. Estimates of changes in river discharge on time scales as short as sub-monthly will also be of interest. This knowledge will not only be essential for the future resource allocation of fresh water but will also enable better flood predictions.

The SWOT mission will use a Ka-band Radar Interferometer (KaRIN) to perform the ocean altimetry measurements [2]. Two Ka-band SAR antennas will be placed 10 m apart with a

bandwidth of 200 MHz. An orbit of 970 km will result in a swath width of 120 km with spatial resolutions less than 100 m. The sea surface height (SSH) precision needs to be at least 1 cm for a 1 km spatial resolution. SWOT will also have an orbit with a 22 day repeat cycle and a 78 degree inclination. This inclination includes important polar ocean areas but still allows for a revisit time of once every 11 days in lower latitudes, providing sufficient temporal coverage to meet the key oceanographic and hydrological objectives.

1.2 Sea Surface Altimetry

The specific oceanographic and hydrological objectives discussed in Section 1.1 can be achieved through surface altimetry. Specifically, surface altimetry determines sea surface heights and terrestrial surface water heights using space-borne radar systems. A pictorial description of altimetry is illustrated in Figure 1.1. Initially, the radar transmits a pulse and receives its echo from the surface at a later time; this propagation time is then used to calculate the distance between the precisely known satellite orbit and the surface. Current and previous altimeter missions have used Ku-band radar from 12-18 GHz. The SWOT mission radar will be a satellite altimeter which uses Ka-band radar from 27-40 GHz. Using a radar at Ka-band rather than Ku-band results in less delay due to the ionosphere, eliminating the need for a dual-frequency altimeter [3]. The higher frequency also provides better spatial resolution to determine sea surface roughness. Ka-band radar does not penetrate snow and ice as deeply as Ku-band radar, thus improving height measurements in those regions. Radar in the Ka-band, however, has greater attenuation due to water and water vapor in the troposphere than Ku-band radar, which renders it unusable about 10% [4].

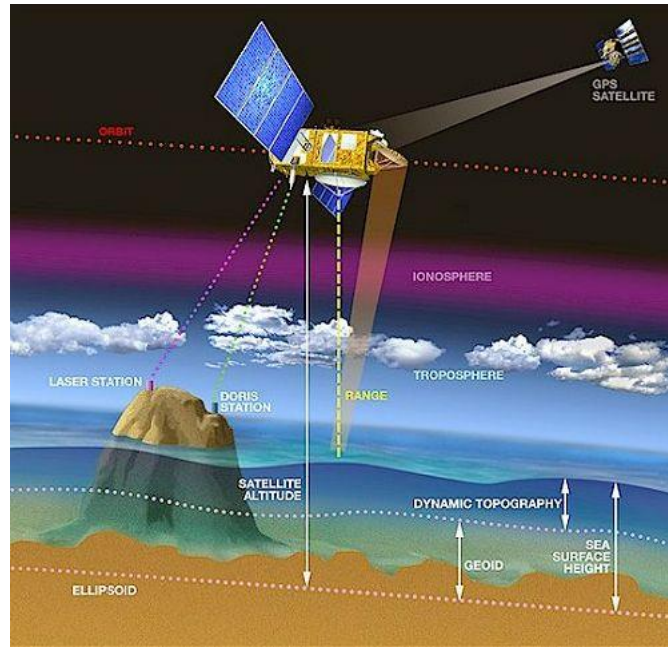


Figure 1.1: Principles of altimetry. [3]

Water vapor content can have a significant effect on the accuracy of the SSH measurement. The speed of light changes when it passes through a medium other than a vacuum due to changes in the index of refraction. The index of refraction in the troposphere is highly dependent upon the temperature and humidity of the air [5]. Temperature variations are easier to measure and model than humidity variations, which can vary from 10^{-2} g/m^3 in cold and dry climates to 30 g/m^3 in hot and humid climates around the Earth [6]. Wet-tropospheric path delay is an increase in propagation time due to a change in the index of refraction from water vapor along its path. Measurement of the wet-tropospheric path delay is necessary to correct altimeter measurements.

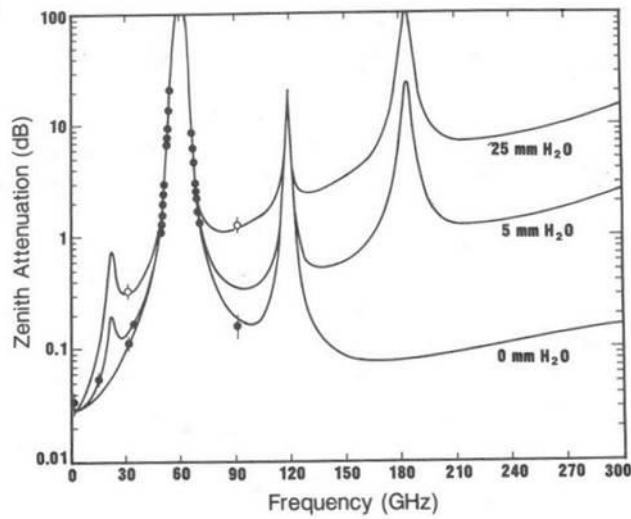


Figure 1.2: Atmospheric attenuation as a function of frequency [7].

Microwave radiometers provide a method to measure the total precipitable water (TPW) in the atmosphere to determine the wet-tropospheric path delay viewed by the radar altimeter. Traditionally, microwave radiometers at 18-37 GHz have been included as part of surface altimetry satellite missions to determine the wet tropospheric path delay over the ocean. One frequency of the 18-37 GHz radiometers, 23.8 GHz, measures the weak water vapor absorption line at 22.235 GHz to retrieve the TPW. The other two channels typically measured by radiometers on surface altimetry missions are window channels at 18.7 and 34.0 GHz. Window channels are frequencies far from absorption lines of atmospheric gases and at which the atmosphere has high transmittance as shown in Figure 1.2.

One limitation of wet-tropospheric path delay correction using 18-37 GHz microwave radiometers is their large instantaneous fields of view at these frequencies. It has recently been considered to add high-frequency millimeter-wave radiometers to improve the spatial resolution of wet path delay measurements near the coasts. These high-frequency radiometers will have

smaller surface footprints in proportion to their wavelengths. The brightness temperature of land is highly variable and more difficult to predict than that of the ocean. Therefore, if the radiometer field of view includes a significant amount of land, the retrieved wet path delay will have relatively large errors.

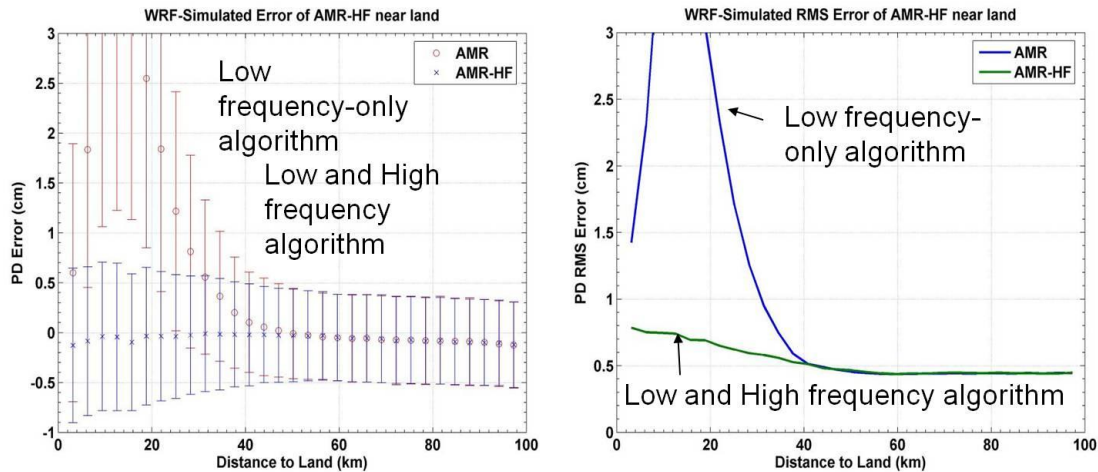


Figure 1.3: Wet path delay error using a high resolution WRF model for both low frequency (18-37 GHz) and high-frequency (90-170 GHz) radiometer channels [8]

A SWOT mission concept study was performed to determine the potential benefit of adding millimeter-wave window channels at 92, 130, and 166 GHz to improve the estimates of wet-tropospheric path delay in coastal areas. Inclusion of these millimeter-wave frequencies with the lower-frequency microwave radiometers on the SWOT mission is under consideration. Figure 1.3 shows that, using only the lower microwave frequencies of 18-37 GHz, the path delay error increases well above the 1 cm SWOT mission requirement within approximately 40 km from land. Adding the millimeter-wave frequencies from 90-170 GHz decreases the retrieved path delay error to less than 1 cm until a few kilometers from land. Therefore, the addition of higher frequency radiometers is expected to improve the accuracy of sea surface height measurements near land.

1.3 Microwave Radiometer Fundamentals

1.3.1 Principles

Microwave radiometers are well-characterized, sensitive receivers that measure thermal electromagnetic radiation. In atmospheric remote sensing, these receivers measure natural radiation from the Earth's surface and the atmosphere. Atmospheric gases radiate electromagnetic energy that varies with frequency, with increased absorption at characteristic frequencies known as absorption lines. In general, this electromagnetic radiation of molecules behaves according to Planck's blackbody radiation law. A blackbody is defined as a material that is a perfect absorber and a perfect emitter of electromagnetic radiation, when it reaches thermal equilibrium. This means that all radiation incident on the material is both absorbed and emitted. Planck's blackbody radiation law is [6]

$$B_f = \frac{2hf^3}{c^2} \left(\frac{1}{e^{hf/kT_{ph}} - 1} \right) \quad (1.1)$$

where B_f is the blackbody spectral brightness ($\text{W} \cdot \text{m}^{-2} \cdot \text{sr}^{-1} \cdot \text{Hz}^{-1}$), h is Planck's constant at 6.63×10^{-34} J·s, f is frequency (Hz), k is Boltzmann's constant at 1.38×10^{-23} J/K, T_{ph} is the physical temperature (K), and c is the speed of light at 3×10^8 m/s. At millimeter-wave frequencies and below, $hf/kT_{ph} \ll 1$, Planck's blackbody radiation law (1.1) is approximated as Rayleigh-Jeans law using Taylor polynomial expansion and approximation as

$$B_f = \frac{2f^2 k T_{ph}}{c^2} \quad (1.2)$$

The radiation intensity received by an antenna can be characterized by (1.3) where A_e is the effective area of the antenna (m^2), f is the receiver's center frequency (Hz), F is the normalized antenna pattern ($\text{W} \cdot \text{sr}^{-1}$), $d\Omega$ is the solid angle of the antenna pattern, θ is the azimuth angle, and φ is the zenith angle.

$$P = \frac{1}{2} A_e \int_f^{f+\Delta f} \iint_0^{4\pi} B_f(\theta, \varphi) F(\theta, \varphi) d\Omega df \quad (1.3)$$

If the antenna is placed in a blackbody chamber and B_f is constant over Δf if $\Delta f \ll f^2$, (1.2) can be inserted into (1.3) to yield (1.4) where P_{bb} (W) is the power received by the antenna from a blackbody.

$$P_{bb} = kT\Delta f \frac{A_e}{\lambda^2} \iint_0^{4\pi} F(\theta, \varphi) d\Omega \quad (1.4)$$

$$\frac{\lambda^2}{A_e} = \iint_0^{4\pi} F(\theta, \varphi) d\Omega \quad (1.5)$$

Using the relationship in (1.5), (1.4) simplifies to (1.6). This result is fundamental to microwave radiometry and provides a linear relationship between power and physical temperature.

$$P_{bb} = kT_{ph}B \quad (1.6)$$

The brightness temperature T_B can be related to the physical temperature T_{ph} of a blackbody, as in (1.7), using a grey body's emissivity e where $0 \leq e \leq 1$. The emissivity of a blackbody is equal to one, is zero for a perfect reflector and is always less than one for grey bodies.

$$T_B = eT_{ph} \quad (1.7)$$

Now that the principles of microwave radiometry have been explained, different radiometer receiver architectures can be considered, which measure brightness temperatures in terms of power.

1.3.2 Comparison of Direct Detection and Superheterodyne Architectures

Direct detection and superheterodyne receiver architectures were considered for the millimeter-wave radiometer designs. The direct detection architecture was selected for the

design of the radiometers at 92, 130, and 166 GHz. The direct detection architecture, as shown in Figure 1.4, is a homodyne architecture in which the detector operates at the RF frequency.

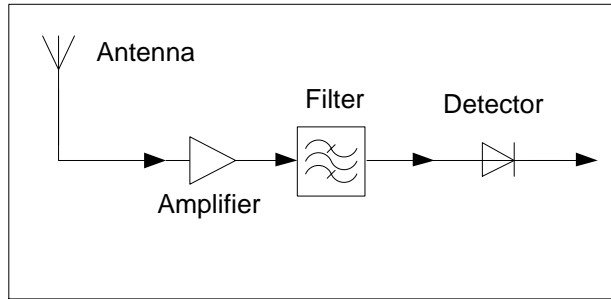


Figure 1.4: Direct Detection Architecture

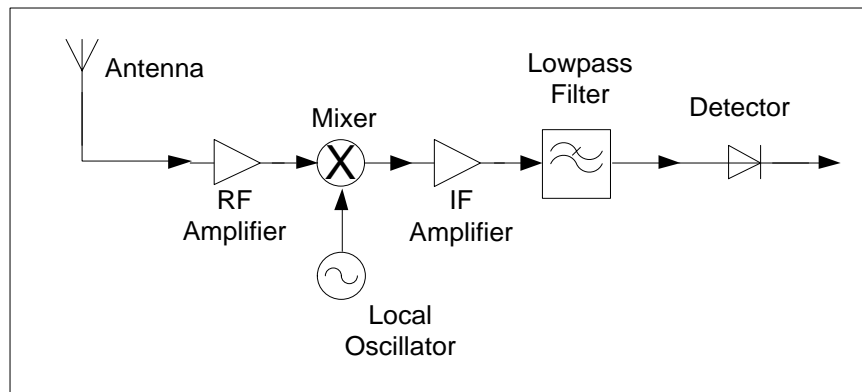


Figure 1.5: Superheterodyne Architecture

The superheterodyne architecture, as shown in Figure 1.5, downconverts the RF to an intermediate frequency (IF) that is easier to work with because it is typically a lower frequency. The receiver accomplishes this by mixing a typically lower frequency from the local oscillator (LO) with the RF. This produces two IF frequencies, $f_{RF} - f_{LO}$ and $f_{RF} + f_{LO}$, with $f_{RF} + f_{LO}$ removed by lowpass filtering so the lower IF becomes the detected frequency. This lower frequency has several distinct advantages over the original higher radio frequency. Active components such as low noise amplifiers (LNAs) and detectors are more readily available and affordable in monolithic microwave integrated circuits (MMICs) at these frequencies. Passive components, such as the filter, can be designed with higher Q and fewer electromagnetic

coupling issues. The addition of a mixer and an LO increases the power, size, and complexity of a receiver in addition to adding loss to the receiver. In addition to the mixer, an LO is needed that is stable over temperature and not prone to drift over time. Some of these stability concerns can be mitigated through thermal control and phase locked-loop techniques, but these increase the power budget and receiver complexity [9]. These parameters are important in receiver design, especially for satellite systems, and should be minimized as much as possible.

The direct detection receiver architecture does not require a mixer or LO and associated circuitry. This reduces the mass, volume, power consumption, and complexity of the receiver. Finding low noise amplifiers at RF frequencies with sufficiently high gain and low noise figure as well as designing filters with a sufficiently high Q are challenges associated with implementing the direct detection architecture at millimeter-wave frequencies. Recent advances in MMIC technology have made viable the implementation of the direct detection architecture at frequencies up to 183 GHz for satellite radiometers.

1.3.3 Comparison of Total Power and Dicke Radiometers

Both total power and Dicke radiometer configurations can be implemented in either direct detection or superheterodyne receiver architecture. Total power radiometers using direct detection receiver architecture are the simplest without a mixer and ideally have the lowest receiver noise temperature as shown in Figure 1.6. Radiometers are characterized not only by their noise temperature but also by their radiometric resolution ($NE\Delta T$). Radiometric resolution is defined as the minimum change in scene brightness temperature that results in a detectable change at the radiometer output [10]. The radiometric resolution of a radiometer is adversely

impacted by the receiver noise temperature and gain variations. Gain variations affect total power radiometers, affect unbalanced Dicke radiometers to a lesser extent, and affect balanced Dicke radiometers not at all.

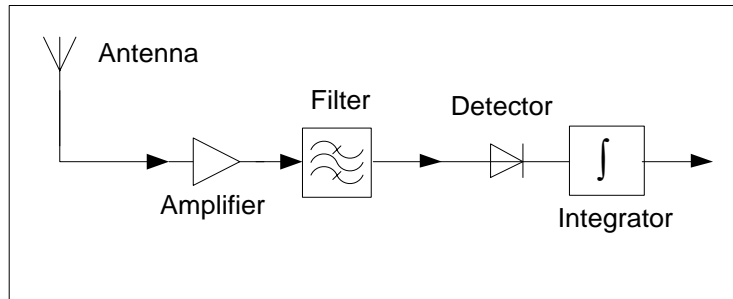


Figure 1.6: Total Power Radiometer Diagram

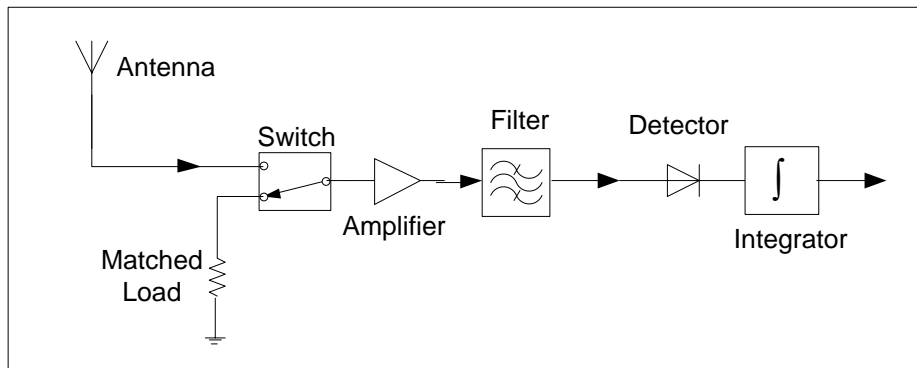


Figure 1.7: Dicke Radiometer Diagram

A Dicke radiometer as shown in Figure 1.7 measures the noise equivalent temperature of a matched load and subtracts it from the antenna temperature through switching. This reduces the effects of gain variations in the radiometer. The rate of switching is chosen to be sufficiently fast so that the gain of the system can be considered constant over one period. In this case a period is the total time spent viewing the scene through the antenna and the matched load, half a period for each. The matched load measurement is then subtracted from the scene measurement either using a difference amplifier or in post processing. This switching and resulting subtraction

enables a significant improvement in the radiometric resolution of the radiometer by reducing the effect of gain variations.

The $NE\Delta T$ for total power radiometers is given in (1.8) and for Dicke radiometers is given in (1.9) and (1.10) [6],

$$NE\Delta T = (T'_A + T'_{REC}) \left[\frac{1}{B\tau} + \left(\frac{\Delta G_s}{G_s} \right)^2 \right]^{1/2} \quad (1.8)$$

$$NE\Delta T = \left[\frac{2(T'_A + T'_{REC})^2 + 2(T_{REF} + T'_{REC})^2}{B\tau} + \left(\frac{\Delta G_s}{G_s} \right)^2 (T'_A - T_{REF})^2 \right]^{1/2} \quad (1.9)$$

$$NE\Delta T = \frac{2(T'_A + T'_{REC})}{\sqrt{B\tau}} \quad (1.10)$$

where T'_A (K) is the antenna temperature, T'_{REC} (K) is the receiver temperature, T_{REF} (K) is the physical temperature of the matched load, and $NE\Delta T$ (K) is the radiometric resolution. While increasing the bandwidth B (Hz) and integration time τ (s) will improve the radiometric resolution of a system, the bandwidth is typically fixed and integration time can be limited by factors such as temporal and spatial resolution. Due to these restrictions, reducing gain variations and the receiver noise temperature are the main approaches to improve the $NE\Delta T$ of the radiometer. The role these terms play in the $NE\Delta T$ of a total power radiometer is shown in (1.8). In contrast, the effect of gain variations in unbalanced Dicke radiometers is reduced by a factor of $T'_A - T_{REF}$, as shown in (1.9). The closer T'_A and T_{REF} are, the more the $NE\Delta T$ is reduced. T_{REF} (K) is the equivalent temperature viewing the matched load, normally the same as T_{ph} (K), the physical temperature of the system. In the case of a balanced Dicke radiometer

(1.10), the gain fluctuations have no effect because T'_A equals T_{REF} . This type of system is difficult to implement in practice due to the natural variability of measured brightness temperatures. A balanced Dicke radiometer has a radiometric resolution twice that of an ideal total power radiometer with zero $\Delta G/G$, assuming the same T'_A , T_{REC} , B , and τ . A reduction in $NE\Delta T$ improves radiometer precision, while radiometer calibration with known sources improves radiometer accuracy.

1.3.4 Comparison of External and Internal Calibration

Calibration determines a linear relationship between the measured radiometer output voltage and a known brightness temperature viewed by the antenna. This relationship is obtained using references of a known brightness temperature, which can be external or internal to the radiometer. Measurement of two references provides a relationship to convert radiometer output voltages to their corresponding brightness temperatures. One method of external calibration is to view two microwave absorbers with known physical temperatures to find

$$V_{out} = aT_A + b \quad (1.11)$$

where V_{out} (V) is the radiometer output measured by the analog-to-digital converter (ADC), a (V/K) is the slope of the line, T_A (K) is the antenna temperature of the scene viewed by the radiometer, and b (V) is the intercept of the line.

$$a = \frac{V_1 - V_2}{T_1 - T_2} \quad (1.12)$$

$$b = V_1 - aT_1 \quad (1.13)$$

V_1 and V_2 with corresponding T_1 and T_2 assume a linear system response and are referred to as calibration points, i.e. the two points used to find the equation of the calibration line. The most common method of performing an external calibration on a remote sensing satellite involves

viewing the cosmic background radiation and a microwave absorber, i.e. T_1 and T_2 , during a portion of the satellite's scanning cycle. Another external calibration method involves moving two known temperatures of microwave absorber in front of the antenna to provide two calibration points. For example, two known temperatures can be obtained by maintaining one microwave absorber at a constant ambient temperature and heating another, i.e. T_1 and T_2 . This method increases the mass, volume, power consumption and complexity, which is undesirable on a satellite system.

As described in Section 1.2, satellite altimetry missions include a nadir viewing radiometer for wet-tropospheric path delay correction without moving parts. Consequently, external calibration is not viable, so internal calibration needs to be utilized instead. The two brightness temperatures for internal calibration are typically obtained through a noise diode and a matched load i.e. T_1 and T_2 . Once T_1 and T_2 are known for the noise diode and matched load, (1.11)-(1.13) are used to determine the calibration line. The noise diode is often coupled into the radiometer and the matched load switched, both prior to the first LNA. The noise diode could be switched in as well, but this adds complexity and may increase the insertion loss before the first LNA, which is undesirable. The accuracy of an internal calibration is limited by the thermal stability of the matched load and the stability of the power output of the noise diode which can become an issue over the lifetime of the noise diode [11]. In addition to whether or not they have moving parts, another difference between external and internal calibrations is whether the complete radiometer is characterized in the calibration. The matched load calibration point in internal calibration does not include the effects of the radiometer before the switch, such as the antenna and coupler. The noise diode calibration point does not include the effects of the

antenna on the radiometer nor does it include effects of different insertion losses between when the switch connects the antenna to the receiver and when it connects the matched load to the receiver. Not including these effects introduces uncertainty. However, internal calibration yields lower mass, volume, power consumption and complexity in a nadir viewing radiometer compared to external calibration.

1.4 Technology Objectives for Millimeter-wave Radiometer Development

The research performed for this thesis was based on a NASA Advanced Component Technology (ACT) program. The four main objectives are to develop a tri-frequency feed horn, switches, noise sources, and demonstration radiometers at center frequencies of 92, 130, and 166 GHz.

1.4.1 Tri-Frequency Feed Horn

A tri-frequency feed horn, Figure 1.8, was designed to create a single antenna focus at the center frequencies of 92, 130, and 166 GHz. Only one feed horn is then necessary to maintain co-located instantaneous fields of view for all three center frequencies at nadir. Using one feed horn for three radiometer frequencies will reduce the mass and volume of the radiometer and simplify the focal plane design.

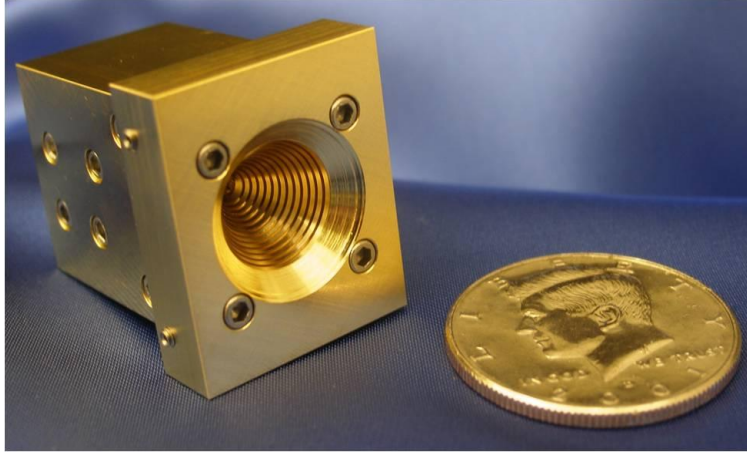


Figure 1.8: Assembled tri-frequency feed horn for the SWOT ACT [8].

The tri-frequency feed horn was designed and tested at the Jet Propulsion Laboratory (JPL). It is a corrugated feed horn with WR-10, WR-08, and WR-05 outputs for the 92, 130, and 166 GHz center frequencies, respectively, and bandwidths of at least 10 GHz with 15 dB return loss or greater.

1.4.2 PIN-Diode Switches at 92, 130, 166 GHz

Low-loss MMIC PIN-diode switches are necessary to produce a Dicke radiometer or a radiometer with internal calibration. The switches at 92, 130, and 166 GHz were designed by JPL and fabricated using Northrup Grumman's MMIC 75 μm InP process. This InP process was selected for the lowest insertion loss and fastest switching time at these frequencies. The switch design objectives were an insertion loss less than 2 dB, a return loss greater than 15 dB, and isolation greater than 20 dB. Low loss is necessary because the switch precedes the low-noise amplifier, so it increases the overall receiver noise temperature [12], as

$$T_{cas} = T_{e1} + \frac{T_{e2}}{G_1} + \frac{T_{e3}}{G_1 G_2} + \dots \quad (1.14)$$

where

$$T_e = (F - 1)T_o \quad (1.15)$$

and T_o is 290 K.

A high input return loss minimizes standing waves at the switch ports, improving system stability. A good match at the switch ports yield the same resistance presented at the input to the first LNA, regardless of whether the LNA's input is connected to the antenna or to the matched load. This in turn results in a consistent RF gain and noise figure, leading to a more stable radiometer. Switch isolation refers to how much signal from one input leaks into the output when the switch is connected to the other input. Sufficient isolation is important when viewing the matched load for internal calibration because it determines the amount of power from the antenna that leaks into the receiver.

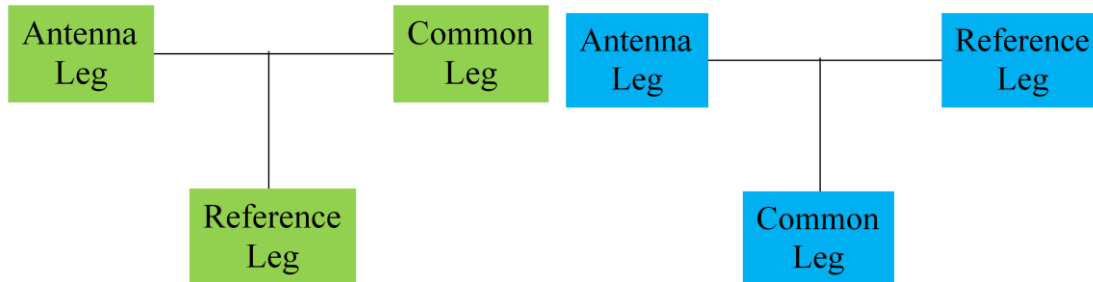


Figure 1.9: Diagram of switch topologies with asymmetric (*left*) and symmetric (*right*).

Several designs were fabricated at each frequency to determine which would result in the switch with best overall performance. Two different layout topologies were implemented, asymmetric and symmetric, as shown in Figure 1.9. Asymmetric designs have the common leg in line with the antenna leg, which allows for a more compact design of the multi-chip module (MCM) housing. Symmetric designs are more traditional and have the common leg positioned orthogonal to the antenna leg. Some switch versions contained an internally matched load

implemented as a radial stub in microstrip, which further simplifies the MCM design by eliminating the need for a separate matched load.

1.4.3 Noise Sources at 92, 130, and 166 GHz

The noise source is an active device used for calibration purposes. In this project, a noise source consists of an avalanche noise diode in waveguide packaging. The noise source uses a waveguide-to-microstrip transition to couple out the noise diode power. This output power can be represented as an equivalent temperature, which is either switched or coupled into the radiometer as one of the two internal calibration points. This output power is typically represented in terms of excess noise ratio (ENR) [12] as

$$ENR = 10 \log_{10} \left[\left(\frac{T_g - T_o}{T_o} \right) \right] \quad (1.16)$$

where T_g (K) is the temperature generated by the noise source. ENR is defined as the added noise power or noise temperature of a component compared to an equivalent resistor at a physical temperature of T_o , 290 K. This added temperature is often referred to as the temperature deflection or difference from 290 K. If the physical temperature of the receiver is not equal to T_o , a correction term of $\left(\frac{T_{ph} - T_o}{T_o} \right)$ needs to be added, as shown in (1.17) [13]. For example, if T_g equals 700 K, a 1.5 dB ENR results from (1.16), while using the correction term in (1.17) with T_{ph} equal to 300 K instead of 290 K results in a 1.61 dB ENR. This change is only 0.11 dB in this case and has a minor effect.

$$ENR = 10 \log_{10} \left[\left(\frac{T_g - T_o}{T_o} \right) + \left(\frac{T_{ph} - T_o}{T_o} \right) \right] \quad (1.17)$$

The design goal for this project was for the noise source to have a 10 dB ENR, which yields a noise temperature deflection of 290 K after a 10 dB coupler. This noise deflection of 290 K corresponds to a total noise temperature of 580 K.

1.4.4 MMIC-Based Radiometers at 92, 130, and 166 GHz

The component technology developments of a tri-frequency feed horn as well as the high frequency switches and noise sources were integrated into demonstration radiometers with center frequencies of 92, 130, and 166 GHz. A system block diagram of these three radiometers is shown in Figure 1.10. These radiometers use waveguide components to connect the tri-frequency feed horn to the multi-chip module, which houses the MMIC components. The data from the detector is recorded by a data acquisition system that includes biasing and thermal control.

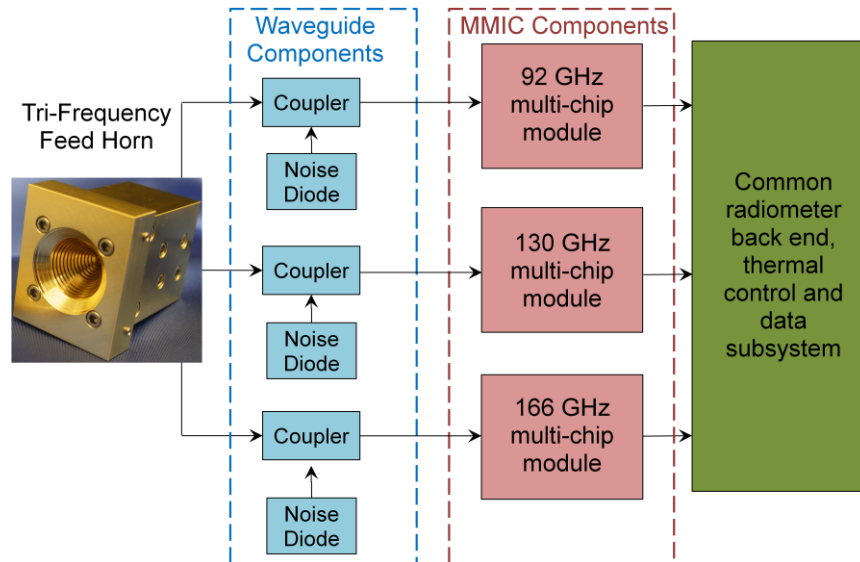


Figure 1.10: Block diagram of the tri-frequency radiometer with 92, 130, and 166 GHz center frequencies.

Chapter 2

92 GHz Radiometer Design and Test

2.1 Block Diagram

The purpose of this research project was to demonstrate component and subsystem technologies to enable millimeter-wave radiometers with internal calibration. The lowest frequency of the three radiometers is centered at 92 GHz. It uses direct detection architecture with internal calibration and can be operated as either a total power or Dicke radiometer. A block diagram of this configuration is shown in

Figure 2.1. The measured antenna signal is coupled with the power from the noise diode through a waveguide based directional coupler before entering the multi-chip module (MCM). The signal is then converted to microstrip and passes through a Dicke switch, RF gain, and filtering before reaching the power detector.

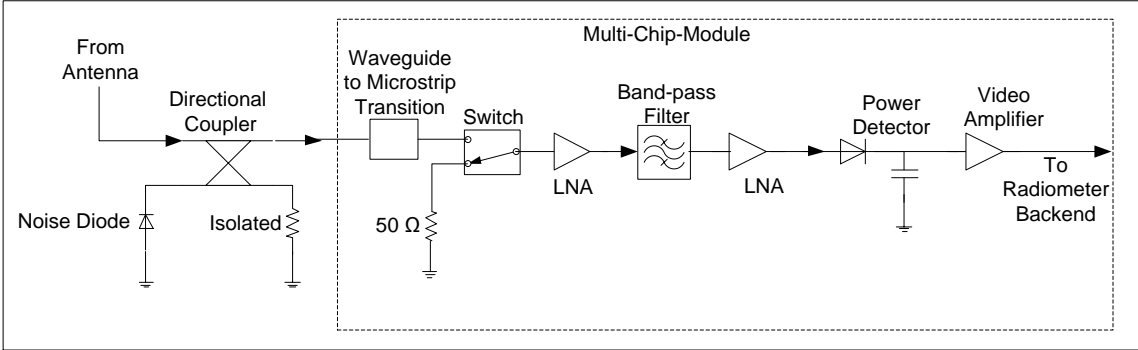


Figure 2.1: Block diagram of a direct detection Dicke radiometer with internal calibration.

The passive microstrip-based components, i.e. waveguide-to-microstrip transition, bandpass filter, and matched load, were all designed as part of this thesis. The switch, LNA, and

power detector used in the 92 GHz demonstration radiometer are all commercially-available MMIC components.

2.2 Predicted Noise Temperature and Radiometric Resolution

Once the radiometer topology has been selected, the important radiometer performance metric of receiver noise temperature can be calculated as discussed in Section 1.3. Initially, the system noise temperature is predicted based upon theoretical component values using the cascaded noise temperature equation (1.14). Since the bandwidth and integration time are often determined by constraints imposed by the mission, the receiver noise temperature is the factor determining a radiometer’s $NE\Delta T$ that is mostly controlled by the radiometer design, as discussed in Section 1.3.3. The 92 GHz radiometer can also be used in either a Dicke or a total power configuration with internal calibration.

Table 2.1: Noise analysis for the 92 GHz radiometer using theoretical component values.

Component	Vendor	Part Number	Gain (dB)	Noise Figure (dB)	Cumulative Noise Temperature (K)
Directional Coupler	Dorado	DCG-10-10E	-0.5	0.5	35
Isolator	Raditek	RADI-75-110-WR10	-0.5	0.5	75
Waveguide-to-Microstrip Transition	MSL	-	-0.25	0.25	97
Switch	M/A-Com	MA4GC6773	-1.2	1.2	220
LNA	HRL Labs	LN5-100	29.0	3.0	727
BPF	MSL	-	-1.5	1.5	727

Receiver Gain (dB)	25.1
Receiver Noise Factor	3.5
Receiver Noise Figure (dB)	5.5
Receiver Noise Temperature (K)	727

The noise analysis of the 92 GHz radiometer shown in Table 2.1 is based upon theoretical and vendor-measured gain and noise figure values. The ideal directional coupler insertion loss is calculated using

$$L_{2,1} = -10 \log_{10} \left[1 - \frac{P_3}{P_1} \right] \quad (2.1)$$

where P_3 and P_1 are ports of the directional coupler. A waveguide isolator was included in the original 92 GHz radiometer design but was determined to be unnecessary in the final implementation. The insertion losses of the waveguide-to-microstrip and bandpass filter are based upon simulation values. The switch insertion loss is based upon the M/A-COM datasheet value at 77 GHz, the highest frequency specified by the manufacturer. The LNA from HRL Laboratories has a specified gain of 29 dB and noise figure of 3 dB. The noise analysis for the 92 GHz radiometer based upon theoretical component values results in a receiver noise temperature of 727 K.

With a 5 GHz design bandwidth, the radiometric resolution as a function of integration time is shown in Figure 2.2. This analysis uses the system noise temperature as a sum of the calculated receiver noise temperature and an antenna temperature of 100 K. The total power radiometric resolution was calculated using (1.8) with gain variations ($\Delta G/G$) of 1.6×10^{-4} . As shown in Section 2.7.5.1, this $\Delta G/G$ value was calculated from (1.8) using the measured receiver noise temperature and minimum Allan deviation. The Dicke radiometric resolution was calculated using (1.9) and a T_{REF} of 301 K, the temperature of the matched load. Both curves are shown in Figure 2.2, and are better than the measured $NE\Delta T$ for the on-orbit Microwave Humidity Sounder (MHS) and Advanced Microwave Sounding Unit (AMSU) at 89 GHz, neither of which have internal calibration.

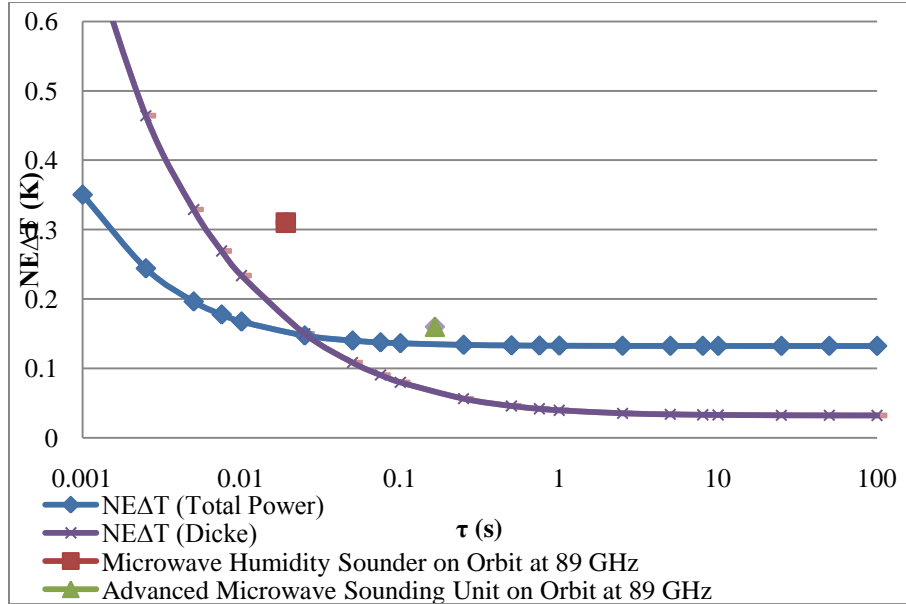


Figure 2.2: Radiometric resolution for the 92 GHz radiometer using theoretical component values with 727 K noise temperature and 5 GHz bandwidth.

A more realistic receiver noise temperature is calculated using measured component values, as listed in Table 2.2. The directional coupler and waveguide through line insertion losses were measured using an Agilent E8364B network analyzer with 75-110 GHz WR-10 waveguide extenders, as described in Section 2.4.1. The waveguide-to-microstrip insertion loss is based upon an HFSS simulation adjusted for a more realistic value [14]. The bandpass filter insertion loss is determined from the HFSS simulation in the cavity, as described in Section 2.6.3.2. The LNA gain and noise figure are specified by HRL. The switch and attenuator insertion losses are measured and include additional losses due to the testing setup, as discussed in Sections 2.4.2 and 2.6.4.2, respectively. Consequently, the measured receiver noise temperature is expected to be less than that in Table 2.2.

Table 2.2: Noise analysis for the 92 GHz radiometer using measured component values.

Component	Vendor	Part Number	Gain (dB)	Noise Figure (dB)	Cumulative Noise Temperature (K)
Directional Coupler	ELVA	DC-10	-0.75	0.75	55
Waveguide Through Line	Custom Microwave Inc.	ST10R-3.0	-0.20	0.20	71
Waveguide-to-Microstrip transition	MSL	-	-0.50	0.50	115
Switch	M/A-Com	MA4GC6773	-3.55	3.55	627
LNA	HRL Labs	LN5-100	29.00	3.00	1540
BPF	MSL	-	-1.56	1.56	1540
Attenuator	MSL	-	-2.75	2.75	1542
LNA	HRL Labs	LN5-100	29.00	3.00	1545
Attenuator	MSL	-	-2.75	2.75	1545

Receiver System Gain (dB)	45.9
Receiver Noise Factor	6.3
Receiver Noise Figure (dB)	8.0
Receiver Noise Temperature (K)	1545

The cumulative noise temperature of 1545 K is approximately double the original theoretical estimate of 727 K. The largest contributor to the increased noise temperature is the greater than expected loss of the M/A-Com switch. While this includes some loss due to the ground-signal-ground (GSG) connections on the CPW to microstrip transitions used in testing, it is still considerably more insertion loss than originally expected. The receiver noise temperature could be reduced considerably if the PIN diode switch designed by JPL was used, since it was measured to have 1.9 dB of insertion loss [15]. The availability and exact dimensions of the JPL PIN-diode switch precluded its use in the RF trench of this MCM. The rationale for the addition of a second LNA and two attenuators not included in the original design will be discussed in Section 2.3.

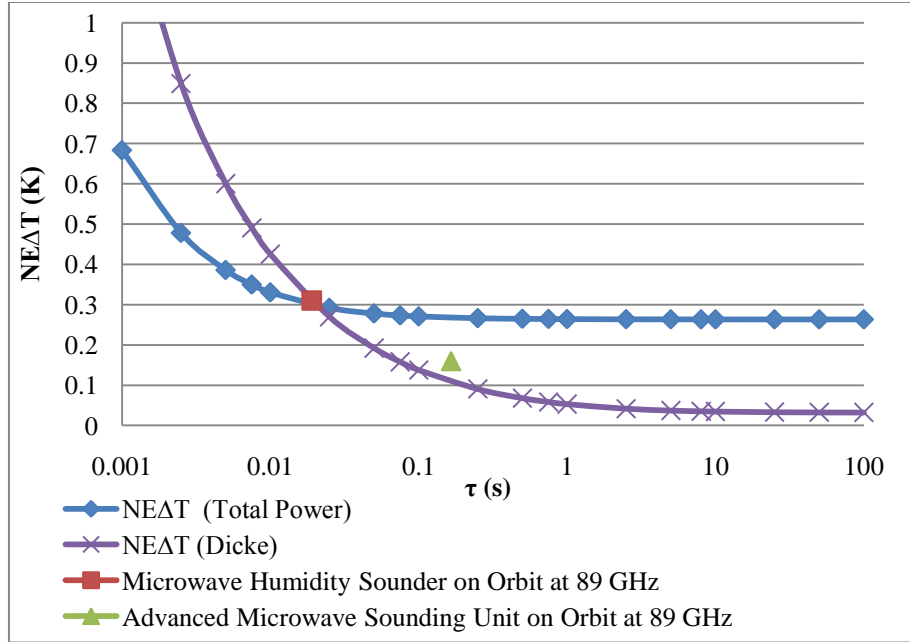


Figure 2.3: Radiometric resolution for the 92 GHz radiometer using measured component values with 1545 K noise temperature and 6.8 GHz bandwidth.

The radiometric resolution results are shown in Figure 2.3 with a T_A of 100 K, T_{REC} of 1545 K, T_{REF} of 301 K, $\Delta G/G$ of 1.6×10^{-4} , and measured B of 6.8 GHz, discussed in Section 2.6.3.2. The radiometric resolution of the 92 GHz radiometer in total power mode using measured component values has a minimum slightly greater than 0.25 K at long integration times. The $NE\Delta T$ in Dicke mode reduces even further to 0.033 K for long integration times.

2.3 Gain Requirements

The amount of pre-detection gain in the 92 GHz radiometer is determined mainly by the gain of the LNAs and how much attenuation is added to the receiver. The first consideration involves minimizing the cumulative noise temperature through adding RF gain as early as feasible in the radiometer, which also improves the $NE\Delta T$ of the radiometer. The amount of attenuation added was determined by the need to use the linear portion of the square law region of the power detector as

$$V = K(\sqrt{P})^\alpha \quad (2.2)$$

where at low input power levels, $\alpha = 2$. This means that the output voltage of the detector is proportional to its input power. K in (2.2) is the sensitivity of the detector, also sometimes represented as β . The HRL 92 GHz zero bias power detector has good linearity up to an input power of -30 dBm. While the minimum detectable power is not specified, -50 dBm was determined to be detectable [16].

Table 2.3: Calculated power at the input of the power detector of the 92 GHz radiometer for the original design.

System Gain (dB)	T_{sys} (K)	T_a (K)	Bandwidth (GHz)	Power (dBm)
25.1	727	600	5.0	-45.3
25.1	727	297	5.0	-46.5
25.1	727	77	5.0	-47.5

Using the receiver gain and system noise temperature calculated from the radiometer configuration in Table 2.1, the input power to the power detector can be calculated using (1.6) with the RF gain included. To ensure all input power to the detector is both detectable and in its square law region, the lowest and highest T_a values will be used to determine the upper and lower bounds. These T_a values correspond to the equivalent noise temperatures of liquid nitrogen and the noise diode, approximately 77 K and 600 K, respectively. Both input power levels to the detector fall within the linear portion of the square-law region of the detector as listed in Table 2.3.

Table 2.4: Calculated power at the input of the power detector of the 92 GHz radiometer for the final design.

System Gain (dB)	T_{sys} (K)	T_a (K)	Bandwidth (GHz)	Power (dBm)
45.9	1545	600	6.8	-21.0
45.9	1545	297	6.8	-21.7
45.9	1545	77	6.8	-22.2

Utilizing the two-LNA configuration from Table 2.2, the largest input power to the detector is -21.0 dBm, as listed in Table 2.4. This is greater than the -30 dBm maximum input for the linear portion of the square-law region. This non-linearity could potentially introduce error in brightness temperature measurements through calibration errors. Fortunately, it is likely that unaccounted for losses due to wire bonds and cavity non-idealities exist in the RF chain. These losses will reduce the receiver gain below the value used in Table 2.4 and consequently decrease the input power at the detector.

This less than expected pre-detection gain of the 92 GHz radiometer was observed during testing. The measurement of the power detector output voltage was used to calculate the input power at the detector using (2.2) and the detector's sensitivity supplied by the manufacturer. The measured output voltage of the detector after a video gain of 101, while looking at the matched load at 301 K, is 264.4 mV.¹ Using an average power sensitivity of 13,500 V/W for the 92 GHz HRL detector, the input power at the detector input is -37.1 dBm. This is considerably less than the calculated value shown in Table 2.4 and is within the square-law region of the detector.

¹ Data acquired on September 14, 2011.

2.4 Commercially-Available Components

2.4.1 ELVA Coupler

The directional coupler couples a portion of the noise diode power to the brightness temperature of the scene viewed by the antenna. The coupler enables a simple and low insertion loss method for adding an internal calibration point to the radiometer. As previously mentioned, increased losses before the first RF gain stage adversely affect the overall receiver noise temperature and radiometric resolution.



Figure 2.4: W-band ELVA 10 dB directional coupler.

The amount of loss in an ideal coupler is directly related to the coupling factor. The higher the coupling factor, the lower the theoretical insertion loss of the coupler. The achievable noise diode power limits how large the coupling factor can be. As discussed in Section 1.4.3, a noise diode with 10 dB ENR corresponds to 0 dB ENR at the output of a 10 dB coupler. A 0 dB ENR is 290 K of deflection or a calibration point of 580 K for the radiometer.

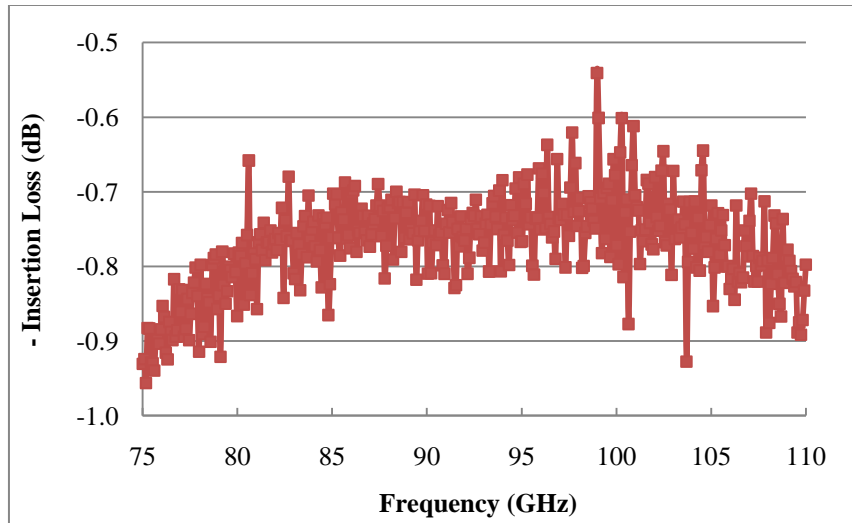


Figure 2.5: Insertion loss of the W-band ELVA coupler.

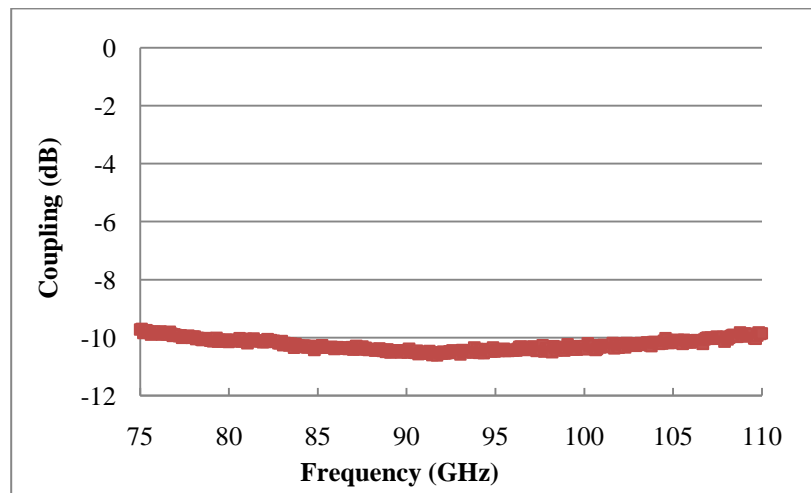


Figure 2.6: Coupling of the W-band ELVA coupler.

The requirements of low insertion loss and necessary coupling are met using the waveguide based WR-10 ELVA directional coupler. It has 10.5 dB of coupling, as shown in Figure 2.6, and low insertion loss of 0.75 dB, as shown in Figure 2.5.

2.4.2 M/A-Com PIN-diode Switch

The switch used in the 92 GHz radiometer to change between the scene viewed by the antenna and the matched load is a 77 GHz single-pole double throw (SPDT) PIN-diode switch

by M/A-Com. It is manufactured on a GaAs substrate and has 1.2 dB of insertion loss at 77 GHz, according to the manufacturer. The 92 GHz radiometer's software is configured for Dicke switching every 500 ms.



Figure 2.7: Measurement test configuration for M/A-COM PIN-diode switch.

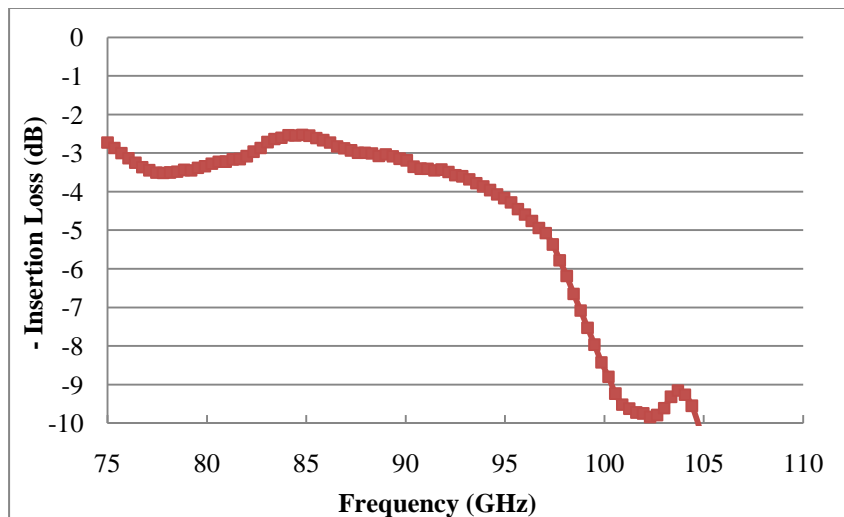


Figure 2.8: Measured insertion loss of the 77 GHz M/A-COM PIN-diode switch for W-band.

Since the switch was designed for operation at 77 GHz, testing across W-band (75-110 GHz) was performed to determine its response at 92 GHz. As shown in Figure 2.8, the insertion loss at 77 GHz is much greater than the specified loss of 1.2 dB. This increased insertion loss is partially due to the test measurement setup shown in Figure 2.7. The losses included in the switch measurement but not due to the switch are a GSG, transmission line, and right angle

microstrip bend. These additional components were necessary due to the switch's symmetric design and the inability of the RF probe station to measure at right angles. Ideally, the asymmetric SPDT switch designed and optimized by JPL for operation at 92 GHz would have been utilized, but it was not available at the time of fabrication of the 92 GHz radiometer.

2.4.3 HRL LNA

Reducing the loss in the radiometer before the first gain stage is important to minimize the receiver noise temperature. After the first gain stage, each subsequent noise factor is reduced by the previous gain as indicated in the cascaded noise factor equation [12]

$$F_{cas} = F_1 + \frac{F_2 - 1}{G_1} + \frac{F_3 - 1}{G_1 G_2} + \dots \quad (2.3)$$

where F_n is the noise factor and G_n is the gain of each component.

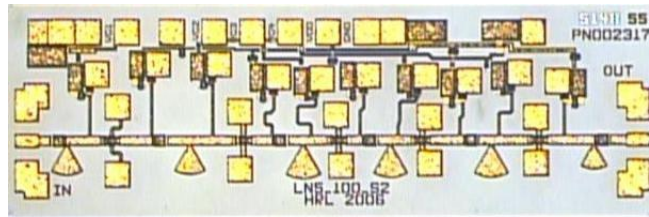


Figure 2.9: 92 GHz MMIC LNA from HRL [17].

The LNA chosen for the 92 GHz radiometer is a five stage InP MMIC LNA by HRL, LN5-100. It has an average gain of 29 dB and noise figure of 3 dB with a drain current of 40 mA. Two LNAs are used in series to deliver a sufficient amount of power to the detector. A gate bias of 0 V and drain bias of 1.14 V to both LNAs is applied resulting in 85.4 mA of drain current. The drain bias is controlled through software and applied after the gate bias so the transistors of the LNA are not damaged through the application of too much current and the LNAs do not start self-oscillating [18].

2.4.4 HRL Detector

The power sensed by the radiometer is converted to an output voltage by an HRL W-band MMIC power detector, V1A, using a tunnel diode.

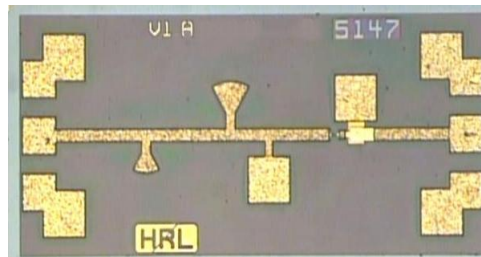


Figure 2.10: 92 GHz MMIC zero bias power detector from HRL [19].

The linearity of the square-law region of the detector begins to degrade above -30 dBm. As discussed in Section 2.3, the RF gain was selected so that the largest input signal to the radiometer results in no more than -30 dBm of input power at the detector. The power detector is also fabricated using an InAs/GaAlSb process and is a zero bias detector. This means that no bias voltage needs to be applied for its operation. The bandpass filter limits the power to the input of the detector to bandwidth of interest centered at 92 GHz. The sensitivity β (V/W) of the power detector varies with frequency over the bandwidth of the 92 GHz radiometer, but this frequency dependence is assumed to be stable and thus does not affect the operation of the radiometer. While the uncertainty of the exact detector sensitivity does not affect the functionality of the radiometer, it does affect the video gain after the power detector. A conservative approach to adding video gain was taken to avoid exceeding the maximum input voltage of the analog-to-digital converter. More details of implementation of this power detector are provided in Section 2.7.2.

2.5 Components Designed at JPL

2.5.1 Tri-Frequency Feed Horn

A tri-frequency feed horn was designed, fabricated, and tested by JPL for operation at center frequencies of 92, 130 and 166 GHz. The design requirements for the horn include 10 GHz bandwidth with better than 15 dB of input return loss.

2.5.2 Noise Source

The noise diode chosen for the noise source is a beam-lead diode designed by M-Pulse Inc. and manufactured for NASA's Goddard Space Flight Center. An excess-noise ratio (ENR) of 13 dB was measured at 92 GHz [20]. When implemented with a 10 dB coupler, this translates to a temperature of 869 K. Not only is this high of a calibration temperature unnecessary, but due to a slightly greater coupling factor, the actual calibration temperature will be less than the theoretical 869 K.

2.5.3 PIN-Diode Switch

JPL developed a MMIC SPDT PIN-diode switch at 92 GHz using the InP PIN-diode fabrication process from Northrop Grumman. Several variations of the PIN-diode switch were manufactured to determine which one had the best performance. These variations were produced mainly due to the uncertainty associated with the diode models at these millimeter-wave frequencies.

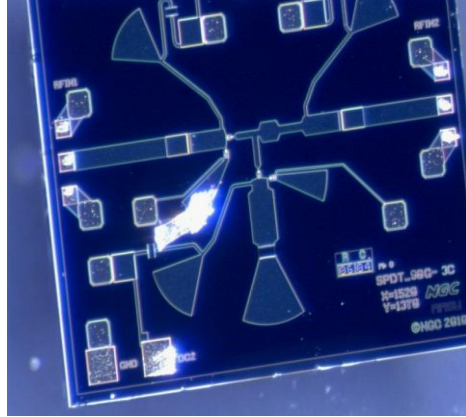


Figure 2.11: 92 GHz asymmetric SPDT pin diode switch with integrated matched load and radial stub tuning to improve isolation. [15]

These variations included asymmetric and symmetric designs with some designs including integrated matched loads. Testing of these switches indicated that they met the insertion loss and input return loss requirements of less than 2 dB and greater than 15 dB, respectively, but did not meet the goal of isolation exceeding 20 dB. Consequently, a radial stub on the switch was tuned to decrease the frequency of maximum isolation in order to meet this requirement. This switch was not used in the 92 GHz radiometer due to availability and timing considerations.

2.6 Components Designed at CSU MSL

2.6.1 Waveguide-to-Microstrip Transition Design

The coupling of electromagnetic energy from waveguide to microstrip is performed through a waveguide-to-microstrip probe. Two probe transition types are broadside and longitudinal. A longitudinal or E-plane probe transition was selected for the 92 GHz waveguide-to-microstrip transition. This type was selected over the broadside configuration to simplify the MCM housing design. The probe was simulated using HFSS and manufactured on 5 mil thick polished alumina substrate with a dielectric constant of 9.9. The microstrip traces were

manufactured in 0.125 mil thick gold. The design was largely based upon the waveguide-to-microstrip probe transition designed by Leong and Weinreb [21]. They designed and produced a W-band probe on 5 mil thick alumina, which is similar to the final design used in this thesis.

2.6.1.1 Design

The design of the waveguide-to-microstrip transition is a four-step process. First, the opening of the waveguide broadwall is chosen to ensure a sufficient waveguide cutoff frequency of 197 GHz [12] using

$$f_{c10} = \frac{1}{2a\sqrt{\mu\epsilon}} \quad (2.4)$$

where a is 30 mils and $1/\sqrt{\mu\epsilon}$ is the speed of light in vacuum. This waveguide cutoff frequency was selected to be at least twice the operating frequency to ensure that lower level harmonics do not provide feedback. Next, the paddle, shown to the right in Figure 2.12, is optimized for nearly constant impedance as a function of frequency. There is no backside metallization below the paddle so that electromagnetic coupling can occur from the waveguide onto the microstrip. A high impedance inductive line tunes out the capacitance series reactance. The final step involves the use of a quarter-wave impedance transformer to convert the paddle resistance to 50Ω with a 50Ω transmission line at the end for wire bonding.



Figure 2.12: 92 GHz waveguide-to-microstrip transition.

The HFSS simulated input return loss shown in Figure 2.13 illustrates a good match for the waveguide-to-microstrip probe transition of better than 20 dB. Figure 2.14 shows the simulated insertion loss, which is flat across W-band.

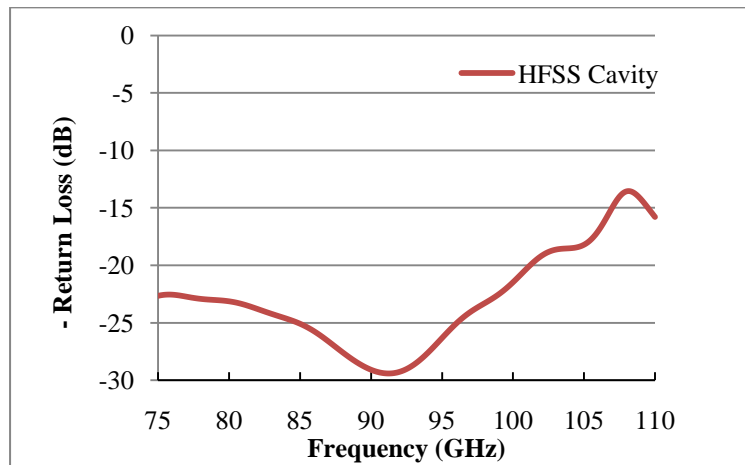


Figure 2.13: Input return loss of 92 GHz waveguide-to-microstrip transition.

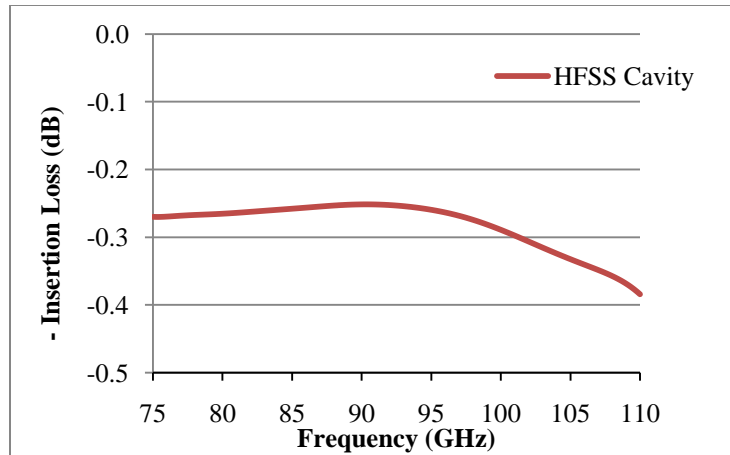


Figure 2.14: 92 GHz waveguide-to-microstrip transition insertion loss.

The input return loss and insertion loss are not compared to measured results because it required a special test fixture consisting of waveguide inputs and outputs to allow for back-to-back waveguide-to-microstrip transitions.

2.6.2 Matched Load

The internal matched load is used for internal calibration and can be used in a Dicke radiometer to minimize gain variations and thus improve radiometric resolution. Two matched loads were designed in HFSS on 5 mil thick polished alumina substrate with 0.125 mil thick gold for microstrip. The two matched load designs are virtual ground and ground via matched load, as described in the following subsections.

2.6.2.1 Virtual Ground Design

The virtual ground matched load design uses a quarter-wave transmission line to translate an open to a ground. This design is illustrated in the 3D HFSS model of the matched load shown in Figure 2.15. From left to right in Figure 2.15, a length of transmission line is followed by a 50 Ω thin film resistor (shown in red) and then a quarter-wave transmission line to translate the

open to a ground. This transformation can be intuitively illustrated on a Smith chart and is referred to as a virtual ground.

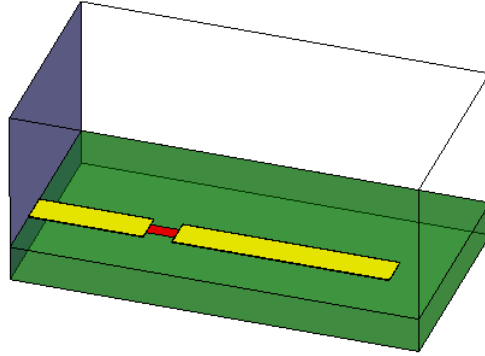


Figure 2.15: HFSS 3D Model of 92GHz 50 Ω matched load with virtual ground.

The thin film resistor is made of TaN, and its size is calculated using

$$R = \frac{L}{W}sq \quad (2.5)$$

where R (Ω) is the total resistance, L is the length, W is the width, and sq (Ω/sq) is the resistance per square unit. Applied Thin Film (ATP), Inc. fabricated the matched loads using their design guidelines [22]. Thin film resistors are also used in the design of attenuators discussed in Section 2.6.4, so the same sq of 25 Ω/sq was utilized to reduce the number of masks and cost of fabrication.

2.6.2.2 Virtual Ground Measurement

The testing of the 50 Ω load with virtual ground was performed using a Summit 9000 RF probe station with 150 μm GSG probe pitch from Cascade Microtech, Inc. in conjunction with an Agilent E8364B network analyzer with W-band waveguide frequency extenders from OML, Inc. A J microTechnology, Inc. ProbePoint 0503 coplanar waveguide (CPW) to microstrip adapter substrate was used to enable testing and is fabricated on 5 mil thick alumina with 150 μm pitch

for the GSG. Its microstrip transmission lines are designed for optimal operation up to 50 GHz. Wire bonds were then added to connect the ProbePoint 0503 to the matched load. The 50 GHz limit and additional impedance due to wire bonds will result in some non-idealities, such as increased loss, when testing at W-band.

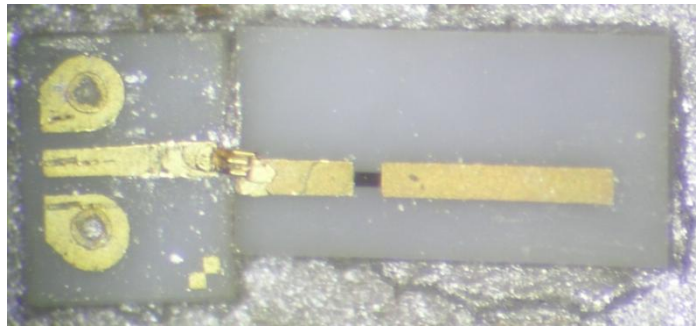


Figure 2.16: 50 Ω load with virtual ground measurement configuration.

The HFSS simulation results of the matched load in a cavity are shown in Figure 2.17 with a good input return loss across the bandwidth. A further HFSS simulation was performed with the matched load in open air since that is how it was tested with the probe station. The open air simulation was enabled by making the ceiling of the cavity a perfectly matched layer (PML). In HFSS a PML fully absorbs electromagnetic fields, preventing reflections as if the simulation was conducted without boundaries, i.e. in open air.

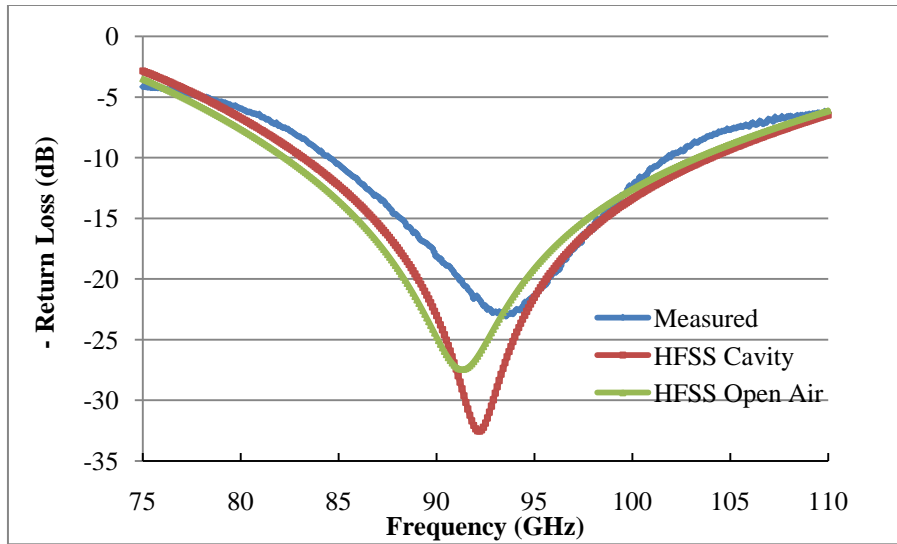


Figure 2.17: Comparison among HFSS cavity simulation, HFSS open air simulation, and measured result for the 50 Ω load with virtual ground.

Figure 2.17 illustrates the good agreement between the simulation and measured results of the matched load. The slight frequency shift between the two results could be caused by several factors. The waveguide port used for the simulation had the same dimensions of the cross-section of the cavity when ideally it should have smaller dimensions for the most accurate results [23]. Also, a dielectric constant of 9.9 was used, while a dielectric constant of 9.7 should be used at frequencies of 10 GHz or higher for alumina. While the wave port sizing guidelines and decreased dielectric value at higher frequencies were not utilized for the 92 GHz design, they were implemented in the 130 GHz passive component designs described in Section 3.6. The wire bond impedance or an error in the test setup calibration could also have resulted in the frequency shift, but the overall frequency shift is too small to have an effect on performance. The measured input return loss is still sufficient for use in the 92 GHz radiometer and is in good agreement with the simulated results.

2.6.2.3 Ground Via Matched Load Design

Plated vias provide a ground for the second matched load design. The vias are holes going all the way through the 5 mil thick alumina substrate and are plated in gold and are shown as grey circles on the right of Figure 2.18.

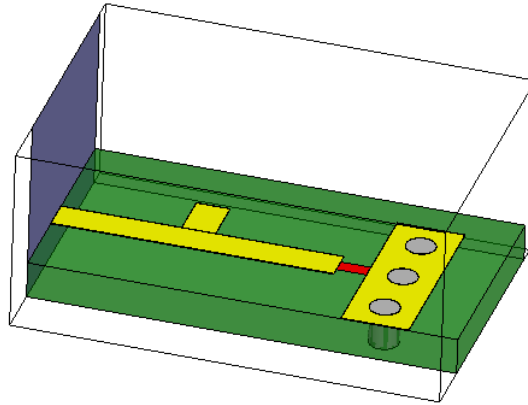


Figure 2.18: HFSS 3D Model of 92 GHz 50 Ω matched load with ground vias.

The vias enable an electrical connection between the top metallization and ground. The vias unfortunately do not form a lossless connection to ground but add some inductance to the circuit. Consequently, a matching stub needs to be added to the left of the TaN thin film resistor to tune the matched load to exactly 50 Ω with zero reactance. The resistance is calculated using (2.5) with an sq of 25 Ω /sq.

2.6.2.4 Ground Via Matched Load Measurement

The 50 Ω matched load with ground vias used for testing is shown in Figure 2.19, similar to the test setup described in Section 2.6.2.1.

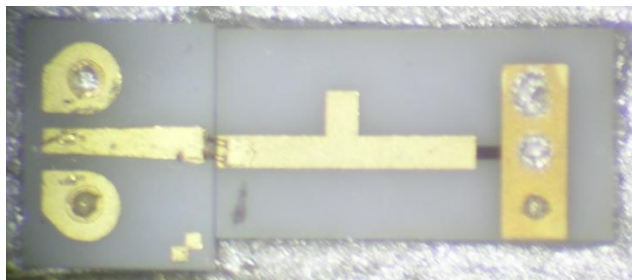


Figure 2.19: 50 Ω load with ground vias measurement configuration.

The HFSS cavity and HFSS open air simulation results are shown in Figure 2.20. Almost no frequency shift occurred between the cavity and open air simulation, in contrast to the matched load with a virtual ground. The ground in this case is not as sensitive to cavity dimensions since it is directly connected to ground and does not use microstrip.

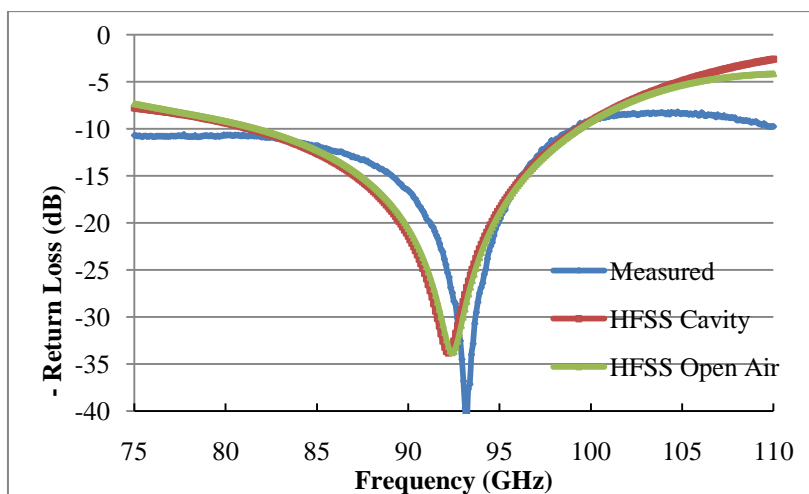


Figure 2.20: Comparison among HFSS cavity simulation, HFSS open air simulation, and measured result for the 50 Ω load with virtual ground.

The input return loss of both HFSS simulations meets requirements, and the measured response shows strong agreement with the simulations. Comparing Figure 2.17 with Figure 2.20, the matched load with virtual ground provides a match that is broader in frequency than the matched load with ground vias. Consequently, the matched load with virtual ground was used for the internal matched load in the radiometer.

2.6.3 Edge-Coupled Bandpass Filter

2.6.3.1 Design

Butterworth and Chebyshev are two types of coupled line microstrip bandpass filters. Butterworth filters are maximally flat, meaning that they have the flattest passband insertion loss response of all filter choices of a particular order and complexity. Chebyshev filters have an equal ripple passband response as well as having a sharper roll off or attenuation outside of the passband than a Butterworth filter of the same order. Plots of attenuation versus normalized frequency for maximally flat and equal ripple filters were used to decide what order of a filter meets specifications. While higher order filters have sharper roll off outside of the passband, the complexity and fabrication costs of the filter increase significantly. Standard low pass filter coefficient tables are used to calculate the characteristic impedance of each set of coupled lines of the filter. This is performed using a simple frequency substitution the bandpass response to the normalized low pass form.

A 5th order Chebyshev coupled line microstrip bandpass filter with 5 GHz bandwidth centered at 92 GHz was selected for the bandpass filter design. A Chebyshev filter was chosen because of its superior out of band attenuation. Since the power measured by the radiometer is across a relatively large bandwidth, the ripple only effects the measurement if it varies with temperature. This should not be an issue since the MCM will be actively temperature controlled. The initial design was performed in Ansoft Designer based upon the ideal Chebyshev coefficient values. The passband response was adjusted to the desired bandwidth and the filter was rotated by approximately 45 degrees with a bend at both ports to decrease the overall filter width, while

increasing its length. Then this design was simulated in HFSS on 5 mil thick alumina substrate with 0.125 mil thick gold and a dielectric constant of 9.9 with a loss tangent of 0.0001.

While manually optimizing the filter by adjusting the coupled line widths, lengths, and spacings, the lid height of the cavity, as modeled in Figure 2.21, was determined to have a major effect on the match of the filter.

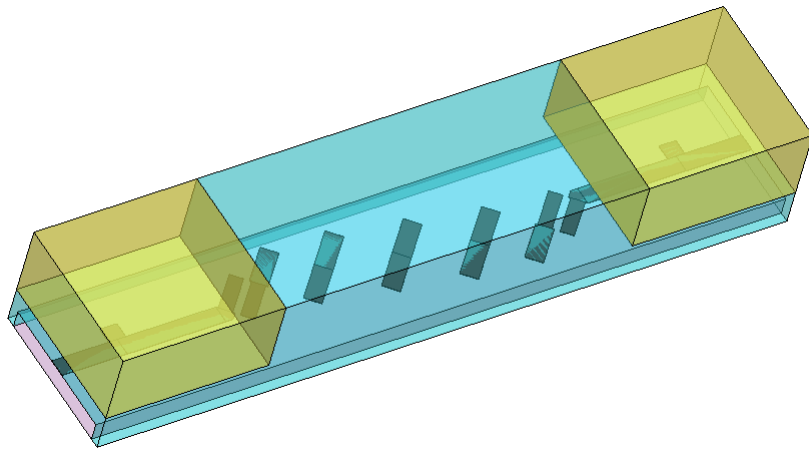


Figure 2.21: HFSS 3D Model of 92GHz BPF

Difficulties related to manually tuning the bandpass filter resulted in the need for matching stubs with lower lid height to obtain a sufficient match over the bandwidth of interest. A more efficient way of optimizing the filter, discussed in Section 3.6.4.1, uses HFSS's optimization feature to eliminate the difficulties in manufacturing and assembly of the matching stubs with lower lid height. This method will be used for the 130 GHz bandpass filter design in Section 3.6.4.

2.6.3.2 Measurement

The measurement setup is the same as that described in Section 2.6.2.2. A 92 GHz bandpass filter with GSGs for testing is shown in Figure 2.22.

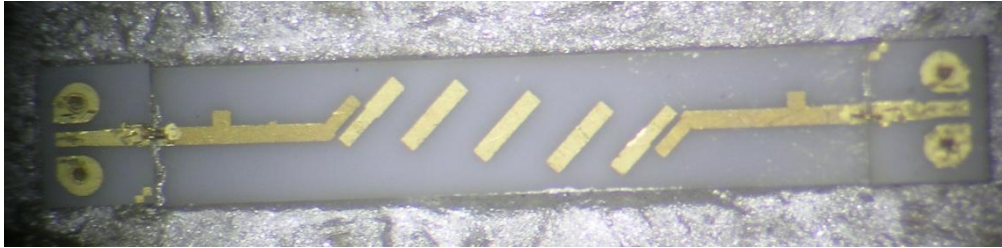


Figure 2.22: 92 GHz bandpass filter measurement configuration.

The input return loss shown in Figure 2.23 exhibits good agreement between the HFSS open air simulation and the open air measurement. The HFSS cavity simulation has a better input return loss, indicating that the cavity has an important effect on the matching of the filter.

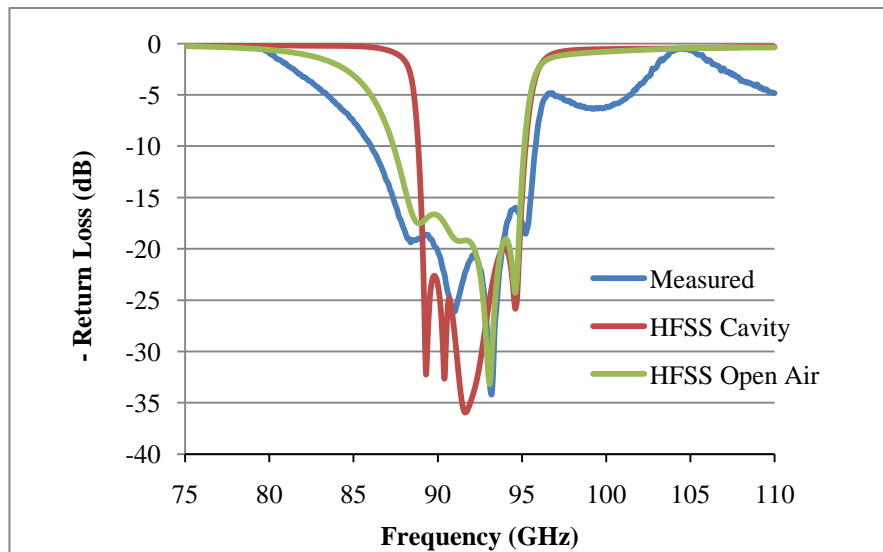


Figure 2.23: Comparison of the input return loss among HFSS open air simulation, HFSS cavity simulation, and open air measurement.

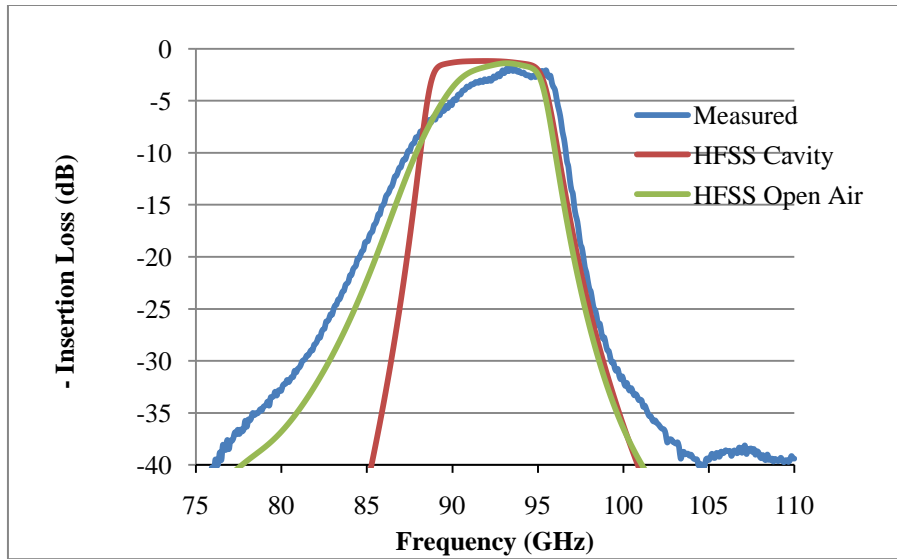


Figure 2.24: Comparison of the insertion loss among HFSS open air simulation, HFSS cavity simulation, and open air measurement.

In Figure 2.24, a comparison among the insertion loss responses of the HFSS open air simulation, HFSS cavity simulation, and open air measurement is shown for the 92 GHz bandpass filter. The HFSS cavity response has a much sharper low frequency roll-off than the open air case. While the 92 GHz radiometer has a bandwidth requirement of 5 GHz, this bandpass filter was designed with a 6.6 GHz bandwidth due to the previously mentioned difficulties associated with optimizing the filter response. The open air measured bandwidth is in close agreement with the expected at 6.8 GHz. This wider bandwidth is acceptable for use in the 92 GHz radiometer and could easily be redesigned for a 5 GHz bandwidth using the optimization techniques described in Section. Since the cavity plays such a pivotal role in the filter response, a test fixture with the same cavity as that in the simulations was manufactured to test the bandpass filter.

2.6.3.3 Test Fixture

Knowing the bandwidth of the radiometer is essential since the power measured is a function of bandwidth, as shown in Section 1.3.1. The test fixture shown in Figure 2.25 is a gold plated brass clamshell design. From left to right it contains a waveguide-to-microstrip transition at the input waveguide, two transmission lines, the bandpass filter, two more transmission lines, and another waveguide-to-microstrip transition at the output waveguide in a 5 mil deep trench.

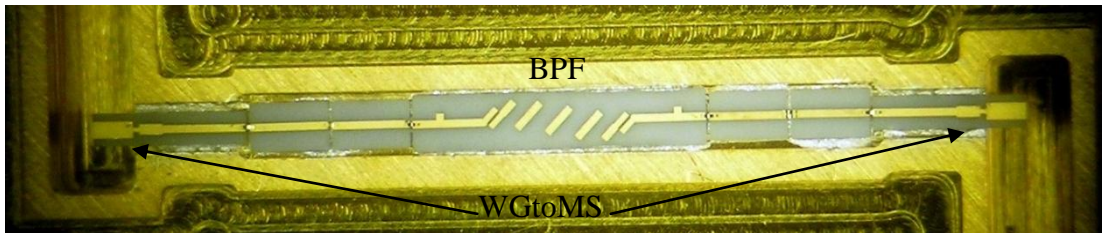


Figure 2.25: A close-up view of the bottom half of the BPF test fixture.

The testing was performed using the Agilent E8364B network analyzer with W-band WR-10 waveguide extenders. The input return loss measurement for the waveguide test fixture containing the bandpass filter is shown in Figure 2.26.

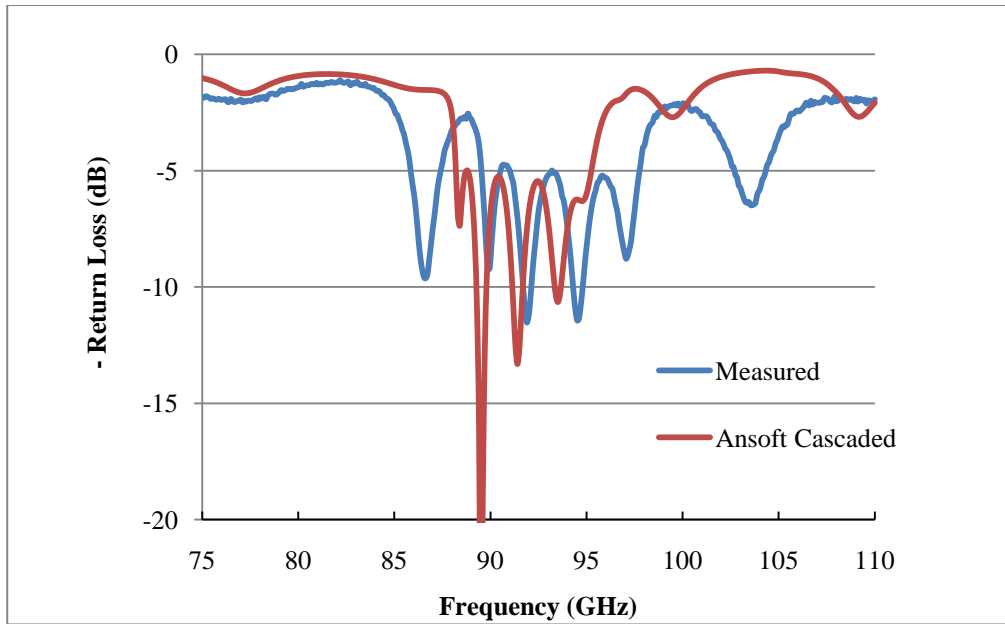


Figure 2.26: Waveguide bandpass filter input return loss measurement compared to Ansoft Designer cascaded components simulation.

This response is worse than the HFSS simulations and open air measurement of a BPF alone by approximately 10 dB or more and has significant ripples in the passband. The ripples are most likely due to the poor match between cascaded components. . When simulated in HFSS, each component model may not quite match the fabricated product, as shown in passive component comparisons between simulations and measurements in the previous subsections. This difference between the model and real component especially holds true for wire bonds. The length, height, angle, and wire bond type, i.e. flat ribbon or 1 mil diameter, are difficult to match consistently in assembly. The wire bond model is the largest source of error in the Ansoft cascaded components simulation. The insertion loss comparison between the cascaded simulation and measurement is shown in Figure 2.27. Good agreement exists between the two with a similar passband ripple and insertion loss.

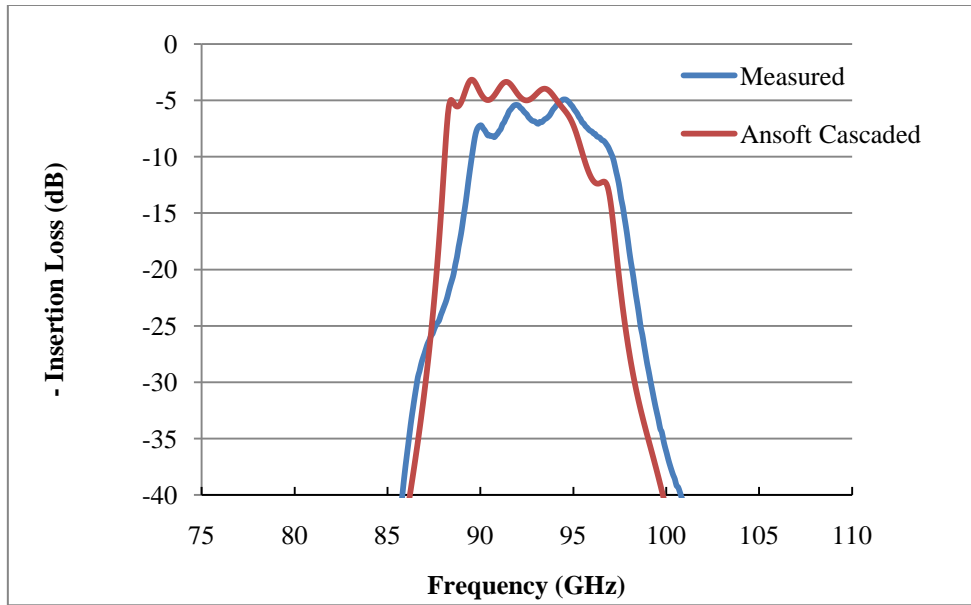


Figure 2.27: Waveguide bandpass filter insertion loss measurement compared to Ansoft Designer cascaded components simulation.

The easiest way to improve the bandpass filter cavity measurement is to reduce the number of components in the test setup. The RF chain ideally should only contain a waveguide-to-microstrip transition, bandpass filter, and another waveguide-to-microstrip transition. This will eliminate the uncertainty associated with four transmission lines and four wire bonds that the current test setup uses. A simpler solution than manufacturing a separate test fixture is to design the filter in a cavity and then compare the open air simulation to the open air measurement. If the open air comparison is favorable, one expects that the cavity frequency response will be similar to the simulated cavity response.

2.6.4 Attenuator

In a microwave receiver, an attenuator is added to reduce the signal power if too much gain exists in the RF chain. Too much gain can saturate some of the LNAs. Too high of input power at the power detector will push its operation out of the square-law region, as discussed in

Section 2.3. An attenuator can improve the matching between components such as the LNAs or bandpass filters. This causes any reflected signal due to a poor match to undergo attenuation before reaching the next component.

2.6.4.1 Design

Several values of attenuation were designed in HFSS on 5 mil thick polished alumina substrate. Resistors are shown in red in Figure 2.28 and use TaN thin film technology with an sq of 25 Ω/sq . The transmission lines are 0.125 mil thick gold plating. Several attenuator topologies exist, such as the pi, tee, bridged-tee, and distributed. Ultimately the distributed topology was chosen for its simplicity of implementation and fabrication. The other topologies have several drawbacks. Resistors cease to behave as lumped elements when they become longer than a quarter-wavelength of the operating frequency. One alternative would be to use a larger sq , but this increases the fabrication cost by requiring multiple resistor masks. These topologies also require mitered microstrip bends and vias which are difficult to simulate and fabricate accurately. On the other hand, the main limitation of the distributed attenuator configuration is its narrow bandwidth. Fortunately, the operational bandwidth at 92 GHz is only 5% and is easily obtainable with a distributed attenuator.

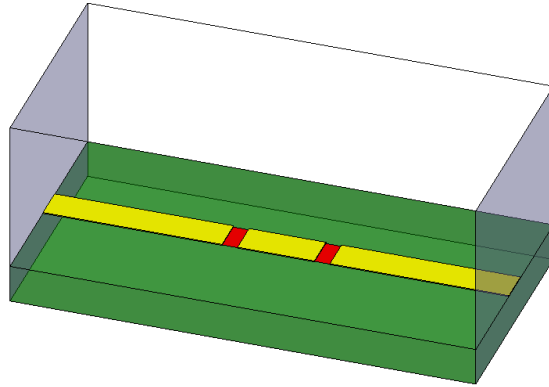


Figure 2.28: HFSS 3D model of 2 dB distributed attenuator.

The design methodology behind the distributed attenuator is simple. The first step is to select the resistance necessary for the desired attenuation level. This can be performed using a simple voltage divider with 29.2Ω for 2 dB of attenuation. A 50Ω transmission line is used at the beginning for wire bonding. Then half of this resistance is simulated, which moves the normalized resistance to 1.3 on the real impedance axis of the Smith chart. A quarter-wave transmission line rotates halfway around the Smith chart to 0.7. The subsequent addition of the other half of the resistance moves the match to 50Ω . A 50Ω transmission line on the end allows for wire bonding. This method results in the expected level of attenuation and a reciprocal 50Ω match at either port.

2.6.4.2 Measurement

The 2 dB attenuator shown in Figure 2.29 uses the same testing setup as that described in Section 2.6.2.2. The input return loss is shown in Figure 2.30, comparing the HFSS cavity and open air simulations to the measured result. This measured match is worse than simulated due to the CPW microstrip GSG transition and wire bonds.

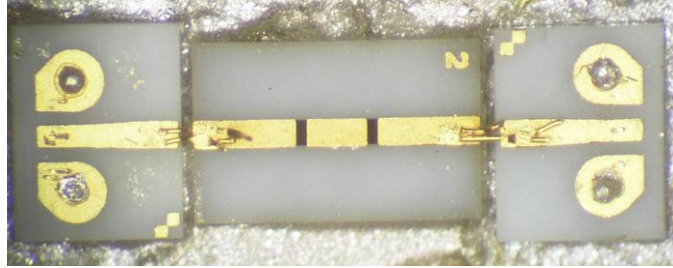


Figure 2.29: 92GHz 2 dB attenuator used for measurements.

The insertion loss of the 2 dB attenuator measured in open air is greater and contains more ripple than expected. The average insertion loss for the bandwidth of interest is 2.75 dB. The ripple possibly results from poor matching with the GSGs and wire bonds. The use of the GSGs also increases the insertion loss measured.

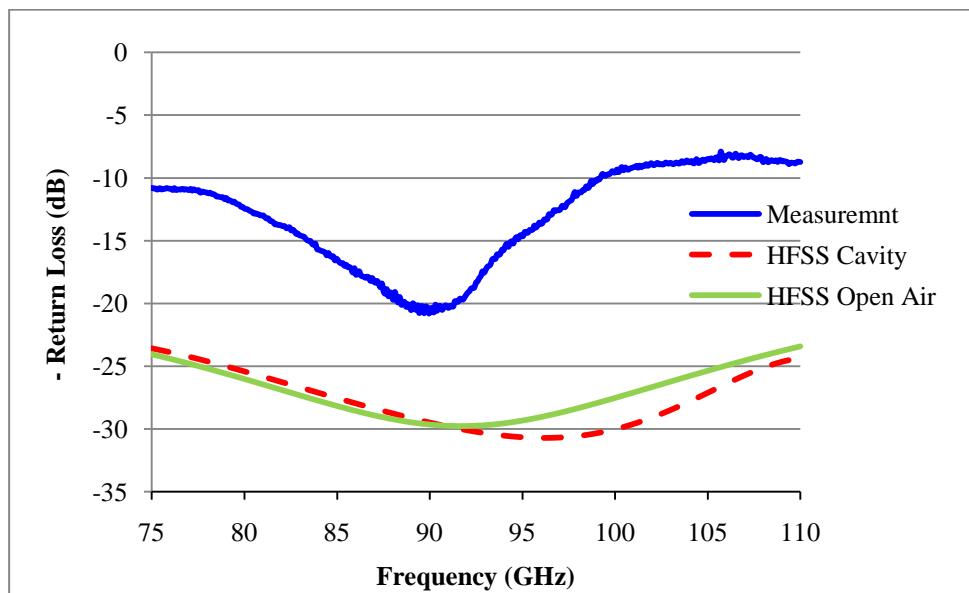


Figure 2.30: Comparison of input return loss for 2 dB attenuator for HFSS cavity, HFSS open air, and open air measurements.

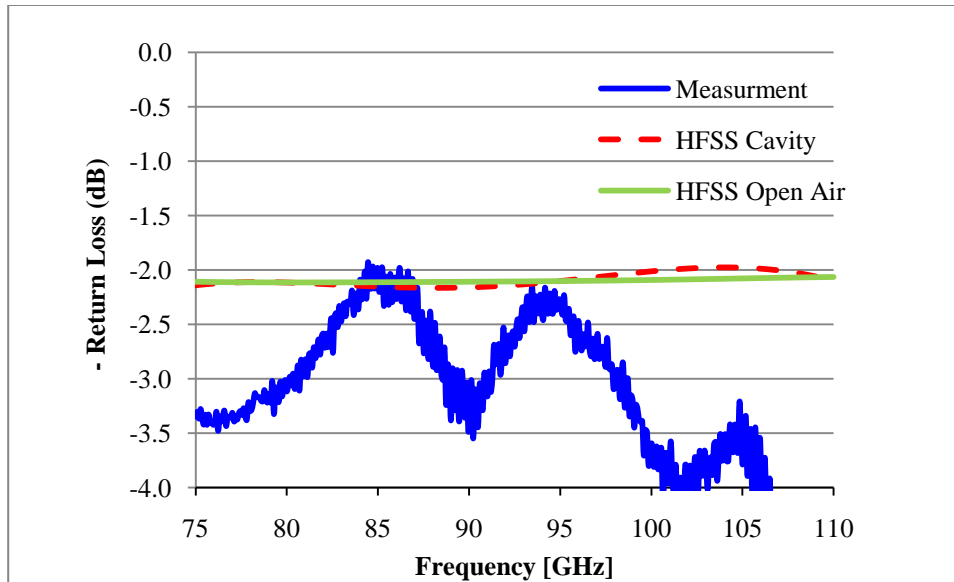


Figure 2.31: HFSS cavity and HFSS open air simulations compared with open air measurements for the insertion loss of the 2 dB attenuator.

2.6.5 Multi-Chip Module Design and Assembly

The multi-chip module for the 92 GHz radiometer serves both electrical and mechanical purposes. Electrically, it allows for the coupling of waveguide electromagnetic energy to microstrip. In addition, the waveguides implement high pass filters to prevent positive feedback at 92 GHz.

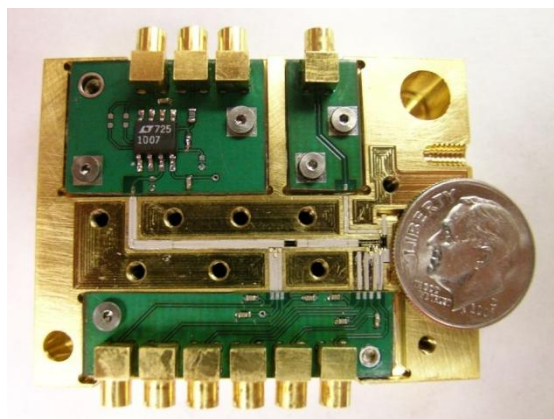


Figure 2.32: Bottom half of the 92 GHz MCM clamshell with one LNA and MMCX connectors.

Mechanically, the housing provides protection for the passive and MMIC components in a trench as part of the gold-plated brass split block, i.e. clamshell, design. It also allows the circuits to create the bias voltages to be as close as physically possible to the switch and LNAs, thus reducing electromagnetic interference. The other mechanical benefit of the brass housing is that it helps to maintain thermal equilibrium, which helps to reduce gain fluctuations of the LNAs and provides an easily measured matched load temperature.

The clamshell design of the 92 GHz MCM was designed in AutoCAD, a 3D mechanical drawing and modeling program. The MCM contains the RF trench in which all of the passive and MMIC components reside. Specifics of the MMIC assembly procedure can be found in Appendix A.

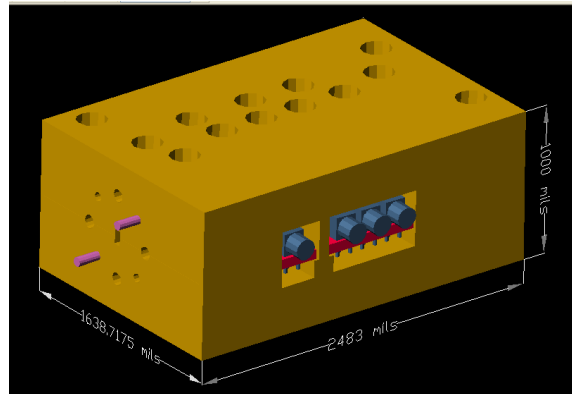


Figure 2.33: 92 GHz MCM model.

The waveguide input and RF trench have the finest detail in the MCM and therefore the tightest tolerances. For example, the backshort distance of the waveguide-to-microstrip transition and the lid height above the bandpass filter are critical to the frequency responses of those components. The RF trench is divided in two parts, with the bottom section being 5 mils deep, the thickness of most of the passive and MMIC components, and the top portion is 20 mils deep, except for the section above the bandpass filter. The unloaded waveguide cutoff frequency for

the waveguide-to-microstrip probe transition is 197 GHz and 148 GHz for the rest of the RF trench, which does not include the switch. An unloaded waveguide does not take into account the effect that components with different dielectric constants have on the cutoff frequency, but instead uses the dielectric constant of air. This cutoff frequency is sufficiently above the radiometer operating frequency of 92 GHz to eliminate the risk of positive feedback to the LNAs. The RF trench was also designed so that one or two LNAs could be used, depending on the final gain needs of the radiometer. The other trenches in the MCM are the biasing trenches which provide DC bias voltages to the switch and LNAs.

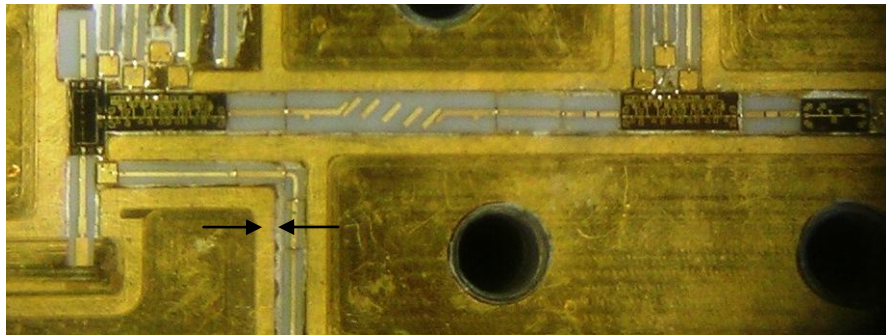


Figure 2.34: 92 GHz radiometer, loaded RF trench with 2 LNAs and arrows pointing to a pressure ridge.

Another important aspect of the MCM design is the inclusion of pressure ridges, as indicated in Figure 2.34. These are walls along the RF and biasing trenches which ensure good contact by directing more pressure between the bottom and top clamshells around these critical areas. It is important that the cavity of the RF trench does not provide a path for electromagnetic energy to cause positive feedback in the system. Numerous bolts are also installed along the pressure ridges of the RF trench to ensure a seamless fit between the top and bottom halves of the MCM.

Several lessons were learned from the design, manufacturing, and assembly of the MCM. For instance, keeping the radii of the corners of the MCM as large as possible is essential to making the MCM cost effective to manufacture. A rule of thumb provided by the machinist who manufactured the MCM clamshell is that the radii should be no smaller than one-third of the depth of the cutout. This is not always possible, especially in the RF trench, but these instances should be limited. Separate trenches for the bias lines with higher waveguide cutoff frequencies rather than one wide waveguide trench should be used to prevent positive feedback at 92 GHz. Another consideration is not to design the lid height too low between the bias board and the bias transmission lines because the wire bonds may short to the top clamshell i.e. ground. Consequently, non-conductive kapton tape was added to prevent shorting the bias voltage wire bonds to ground. Locator pins in the clamshell ensure that it fits together properly without any of the parts or wire bonds being damaged when the two halves are put together.

2.7 Testing

After finishing individual component testing, the passive and active components were integrated to produce the 92 GHz radiometer. Analysis of the radiometer involved determining its mass, volume, and power consumption. The receiver's noise temperature, $NE\Delta T$, and thermal stability were also tested. In addition to the RF section, the radiometer includes a data acquisition and control board to record the radiometer's output voltage as well as control hardware and software. In addition, precise thermal control is essential to minimize gain variations and provide stable radiometer performance.

2.7.1 Mass, Volume and Power Consumption

The mass, volume, and power consumption of the 92 GHz radiometer were characterized to provide realistic baselines for the design of MMIC-based millimeter-wave direct detection radiometers with internal calibration for airborne and space-borne use. The dimensions of the 92 GHz radiometer are shown in Figure 2.35. The radiometer dimensions are 9.91" L x 1.55" W x 5.12" H, and it has a volume of 78.9 in³. The length and height could each be reduced by 2" by substituting 1" waveguide through lines for the current 3" through lines. The MCM itself has dimensions of 2.48" L x 1.64" W x 1.00" H.

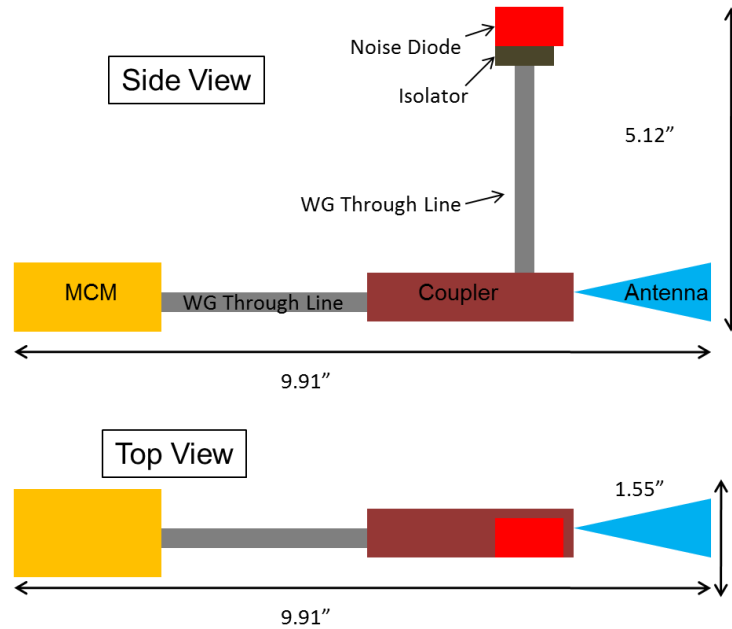


Figure 2.35: Dimensions of the 92 GHz radiometer.

The data acquisition and control board of the 92 GHz radiometer consumes 3.22 W, while the MCM consumes just 0.204 W, as listed in Table 2.5. The total power consumed would be considerably higher if the power to the microcontroller board and thermal control were included. The mass of the MCM and its waveguide components is just under 700 g and could be reduced further by redesigning the MCM and using 1" waveguide through lines.

Table 2.5: Power and mass of the 92 GHz radiometer.

	Power (W)	Mass (g)
MCM	0.204	329.3
Waveguide components with a WR-10 standard gain horn antenna		346.0
Peltier unit, heat sink, and fan (no TCM)		463.0
Data acquisition and control board	3.22	136.6
Microcontroller board		196.9
Total	3.424	1471.8

2.7.2 Multi-Chip Module Bias Boards

In order to bias the LNAs and switch as well as provide a path for the power detector output voltage, three bias boards were designed for the 92 GHz MCM using OrCAD schematic and PCB editors. Isolation between the two MCM bias boards above the RF components in Figure 2.32 was increased by adding a brass wall to separate them.

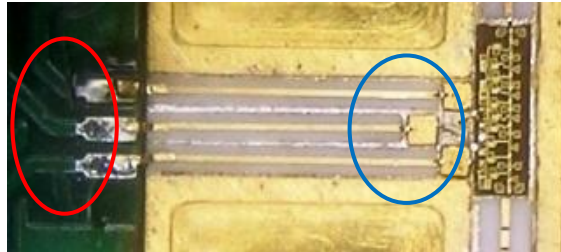


Figure 2.36: 92 GHz LNA biasing trench with PCB bond pads (red) and capacitors (blue).

Low pass filtering for the LNA gate and drain biases were included on all of the MCM bias boards to eliminate high frequency noise above 160 kHz. Capacitors were placed as close as possible to the bond pads which were in turn connected to the bias transmission lines. The bias transmission lines are microstrip lines fabricated on an alumina substrate, which connect the bias from the MCM bias board pads to the MMIC components in the RF trench. In the biasing

trenches capacitors with wire bond inductance provide noise. Each of these capacitors has a value of 120 pF and dimensions of 10x10x5mils. They are available from American Technical Ceramics, 111SK121M100TT.

Several lessons were learned during the design, assembly, and testing of the bias boards in the MCM. The cutout depth for these boards needs to take into account the thickness of the silver epoxy used to affix the boards to the bottom half of the MCM clamshell in addition to the PCB thickness. If this is not done, wire bonding from the PCB pads to the bias transmission lines is difficult due to the height difference between the two. The bond pads on the PCB were covered in solder paste, which is difficult to wire bond to and can damage the wire bonder tip. An alternative is to gold plate the bond pads, which is expensive, or connect them by welding. However, the two most important lessons learned from the 92 GHz MCM bias boards involved ground loops and power detector protection. Initially, individual Tyco MMCX coaxial connectors were used to make each connection from the data acquisition and control board to the MCM. These connectors proved problematic due to the small wire gauge necessary for the coaxial cables. It was difficult to ensure that the outer cable sheath made contact with the connector ground. Secondly, each of the individual ground paths provided the opportunity for ground loops and a low impedance path for noise to couple onto. Initial testing of the 92 GHz radiometer revealed these issues through noisy and inconsistent measurements partially due to these grounding issues. Redesigning the data acquisition and control PCB along with adding a single point of ground and non-coaxial connectors eliminated these issues. A ground offset still exists between the PCB and MCM, but it is constant and measurements are easily corrected. The new connectors used in the final design were PicoBlade and PicoClasp connectors by Molex.

They were chosen due to their small form factor, but they are not robust to repeated insertion. Using pre-crimped wires for stable connections helps to mitigate this issue. A better, albeit more expensive, option is to use the nano-style connectors from Omnetics Connector Corporation. These connectors have a slightly larger form factor preventing their use in the specific design of this 92 GHz MCM, but they provide more robust connections and come populated with pre-crimped wires.

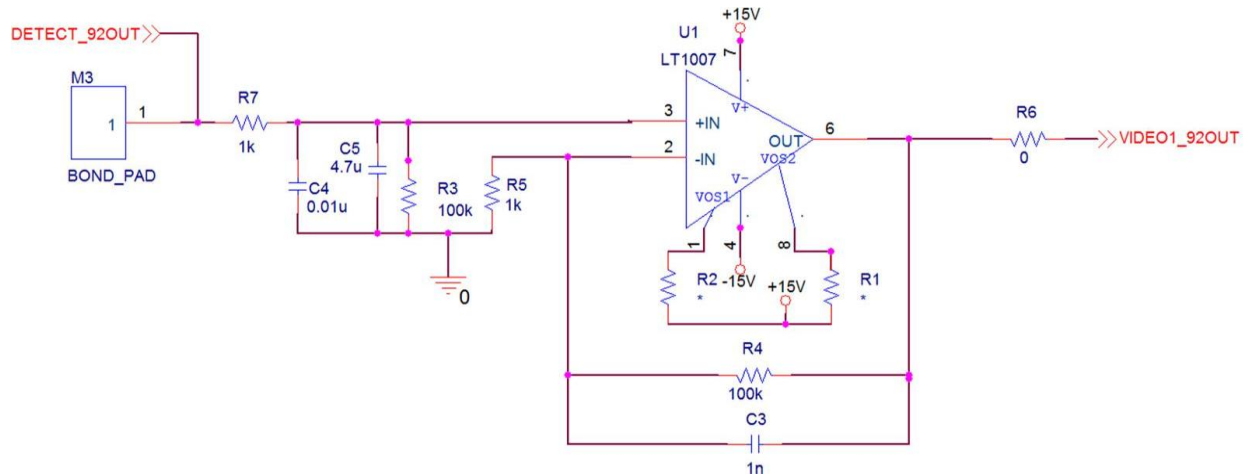


Figure 2.37: Video Board schematic for PCB in the 92 GHz MCM

Since a MMIC zero bias power detector was used in the 92 GHz radiometer, video amplification was applied directly at its output in the MCM to ensure better noise immunity. During initial testing, the HRL power detector was damaged several times and had to be replaced. Initially, the damage to the detector was attributed to electrostatic discharge (ESD). As precautions against ESD were taken and failures continued to occur, other causes were investigated. Ultimately, it was determined that voltage transients of several hundred millivolts were detected at the input of the video amplifier when power was applied. These voltage transients were damaging the power detector and not ESD as previously suspected. As shown in Figure 2.37, filtering was added to the non-inverting video amplifier terminal as well as resistance to ensure the same input offset current at both terminals. The 1 k Ω resistor (R3) and

the 0.01 μF (C4) and 4.7 μF (C5) capacitors were added to form RC filters at the non-inverting terminal. The low pass filter corner frequencies are 16 kHz and 34 Hz, respectively. When the radiometer is off, the output of the detector is essentially ground so the non-inverting terminal sees 1 k Ω in parallel with 100 k Ω , while the inverting terminal sees the same due to the low impedance output of the amplifier. Choosing the same resistance values ensures the same offset at the input terminals of the video amplifier. The implementation of these changes sufficiently protected the power detector from damage due to the video amplifier.

2.7.3 Data Acquisition and Control System

The data acquisition and control system consists of the SAM3U-EK microcontroller development board as well as the data acquisition and control board, as shown in Figure 2.38. This system is controlled through a user interface described in Appendix C.

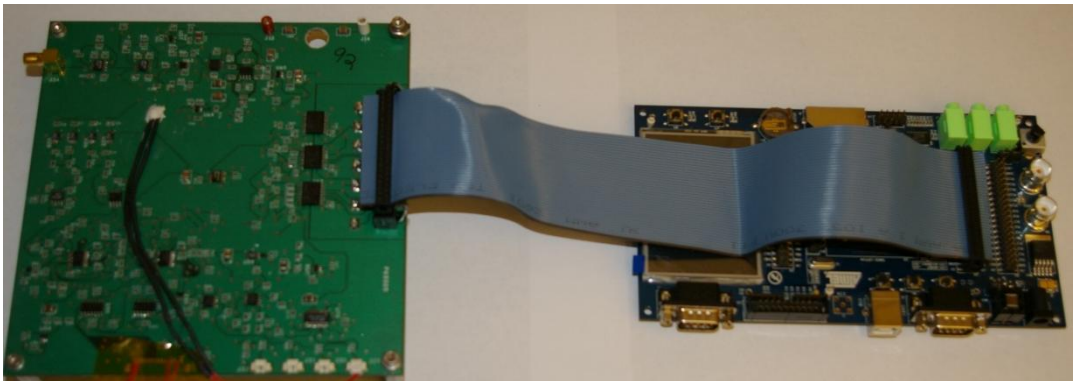


Figure 2.38: Data acquisition and controller board (*left*) and SAM3U-EK (*right*).

The data acquisition and control board includes video amplification and detection for the MCM power detector output voltage, LNA gate and Dicke switch driver control, temperature and LNA drain current monitoring, and voltage regulators for the all sub-systems of the radiometer. A more detailed breakdown of the data acquisition and control system is shown in

Figure 2.39. Differences between the final data acquisition and control board are detailed in Appendix B.

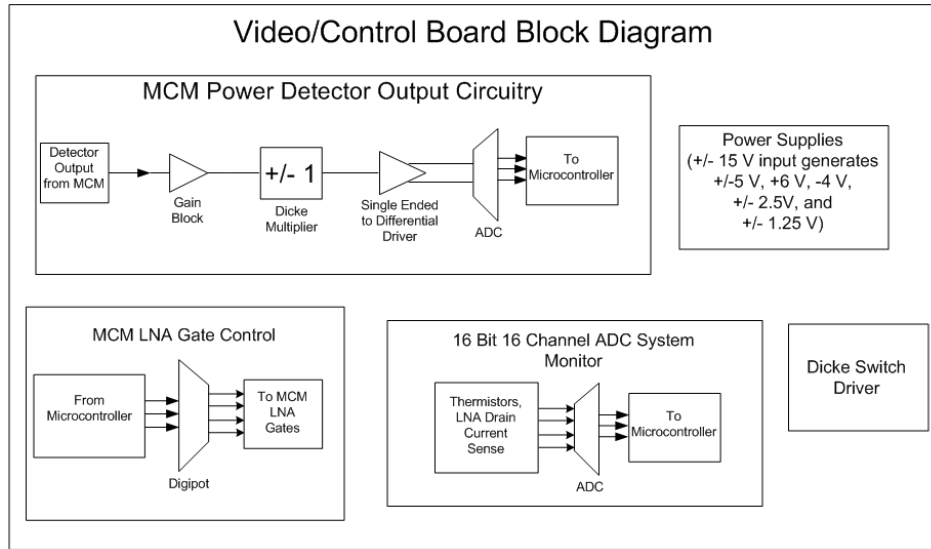


Figure 2.39: Block Diagram of the data acquisition and control system for the 92 GHz radiometer.

2.7.3.1 Video Gain and Detection

One of the major sub-systems of the data acquisition and control board is the video gain and detection circuitry, as described in Appendix G. Video gain is applied to the output voltage from the HRL power detector in several stages to provide a total linear gain of 1495 in the 92 GHz radiometer. This ensures the linearity of the signal and is less than the maximum input voltage of the analog-to-digital converter (ADC). The gain is provided using a LT1007 low noise operational amplifier recommended by HRL in conjunction with their 92 GHz power detector. It has a specified noise level of $4.5 \text{ nV}/\sqrt{\text{Hz}}$ at 10 Hz and $3.8 \text{ nV}/\sqrt{\text{Hz}}$ at 1 kHz, which is important since the voltage output of the detector is on the order of several millivolts before any video gain. One of these gain stages was implemented in the MCM to ensure a larger and more stable output voltage that is more immune to noise. After the video gain, a low loss single-pole/double-throw (SPDT) switch, along with the INA 129 differential amplifier,

performs the Dicke switching subtraction, as described in Section 1.3.3. Since the SPDT switching signal is controlled in software, the radiometer can be operated in total power or Dicke mode. The Dicke switching was performed at a 2 Hz rate with a 5.3 Hz low pass filter at the differential amplifier for averaging. If averaging is performed only in post processing, the video gain hardware can be simplified by eliminating the SPDT, low pass filter, and difference amplifier. The last stage in the video amplification and detection before the ADC is AD8132 single ended to differential driver. This driver is necessary to use the ± 2.5 V input range of the ADC. The LT2452 is a 16-bit delta-sigma ADC with a single differential input. It transmits the data to the microcontroller through a serial peripheral interface (SPI) with up to 60 conversions a second. A sampling rate of 56 Hz was utilized, and data was written to a secure digital (SD) card in blocks of 10 samples each. This video amplification and detection configuration is low noise, fast, and simple to implement as well as operate.

2.7.3.2 Drain and Gate Biasing

All power supplies for the LNA drain and gate bias as well as other support circuitry were chosen to be as low noise as possible, with details provided in Appendix G. The 1.25 V drain voltage is supplied by four low noise voltage references in parallel for reduced noise as

$$e'_n = \frac{e_n}{\sqrt{N}} \quad (2.6)$$

where e_n corresponds to $35 \text{ nV}/\sqrt{\text{Hz}}$ at 5 Hz and $N = 4$ is the number of voltage references in parallel. This resulting drain voltage is used as a reference for a low noise high current buffer amplifier. The LNA gate bias can be set values between 0 and -1.25 V by using an inverting operational amplifier with the 1.25 V reference. Both the drain and gate biasing can be applied in two ways. One way uses the ISL22444 256-tap digital potentiometer to change the gate

biasing between -1.25 and 0 V with a software command. While this implementation allows the gate voltage to be easily varied to obtain the recommended drain current of 40 mA with a 1.25 V drain bias, excess noise can be introduced from the digital potentiometer to the LNAs resulting in a larger receiver noise temperature as well as issues with ground offsets. The second method uses voltage dividers to obtain the appropriate drain and gate biasing. Ideally, these voltage dividers would be placed inside the MCM as close as possible to the LNAs to prevent noise from coupling onto a smaller bias voltage. The voltage dividers were not implemented on the 92 GHz MCM bias boards, but the gates were grounded in the final implementation, eliminating this need. The MAX4626 switch was utilized to control when the drain bias was applied so that the LNAs were not damaged. The LNA biasing involved grounding the gates and applying a 1.14 V drain bias, which drew a drain current of 85.4 mA. This is slightly higher than the 40 mA per LNA that the datasheet associates with 29 dB of gain. Consequently, the LNA gain is probably slightly higher than the nominal 29 dB. The LNA drain current is monitored by the LT2439 16-bit 8 channel ADC through a 1 Ω current sense resistor used in conjunction with an INA129 operational amplifier.

2.7.4 Thermal Control

Thermal control and monitoring are used to improve the stability of the radiometer. The MCM is temperature controlled using a proportional, integral, and differential (PID) controller, specifically TC-36-25 RS232 from TE Technologies, Inc. This temperature control module (TCM) is used with a Peltier unit, heat sink, and fan to both heat and cool the MCM to a specific temperature. Although the temperature controller with a MP-2996 supplied thermistor is

specified to be able to stabilize the temperature within ± 0.01 K, actual physical temperature control stability when applied to the MCM was ± 0.1 K.

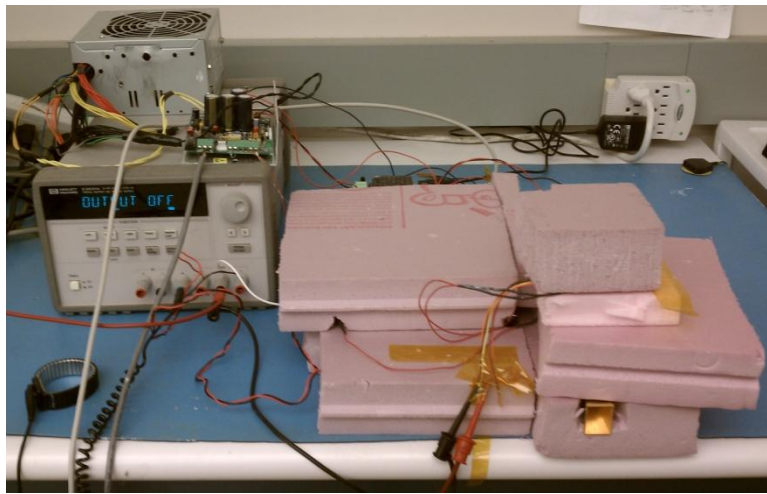


Figure 2.40: 92 GHz radiometer test setup with thermal control.

The vendor supplied temperature control UI with RS232 serial port communication was used with the settings listed in Appendix E.3 [24]. In addition to this active temperature control, solid extruded polystyrene foam insulation encased the radiometer and PCB. Separate temperature monitoring was performed using the precision 44032 thermistors by Omega, which have an accuracy of 0.1 K. They were used in combination with voltage dividers and the LT2439 ADC to record the temperatures of the MCM, PCB, and noise source.

Temperature control has a significant effect on stability of the radiometer. Although a combination of active and passive thermal control was used, a significant system warm-up time is necessary to achieve thermal equilibrium.

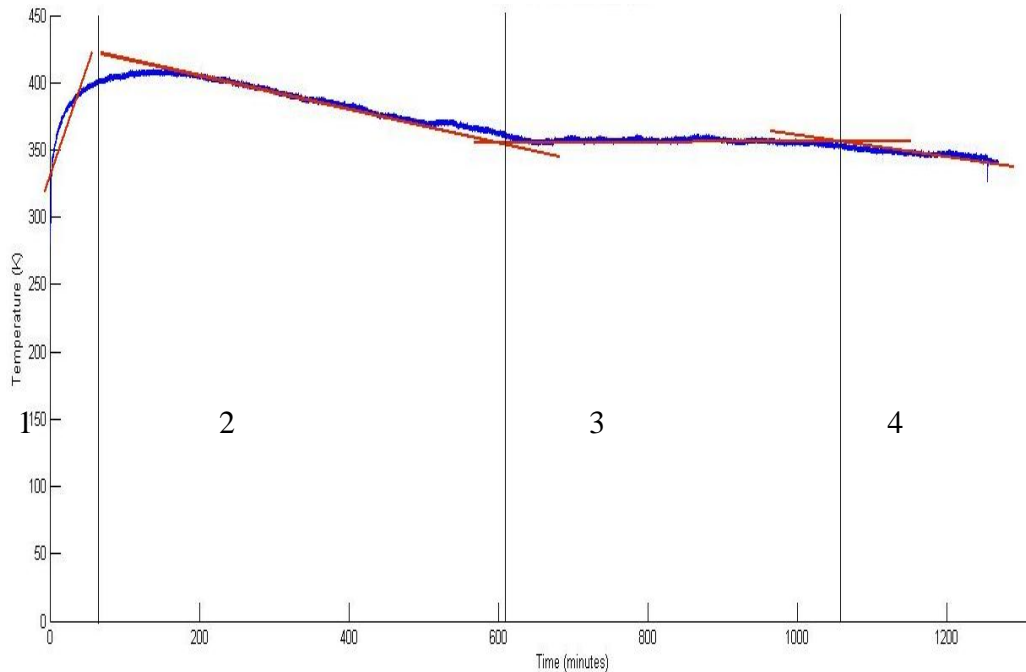


Figure 2.41: Long term 92 GHz matched load equivalent noise temperatures using previous calibration coefficients.²

Long term testing of the 92 GHz radiometer using active and passive thermal control was conducted to determine the thermal stability of the radiometer. Figure 2.41 shows matched load equivalent noise temperatures using previous calibration coefficients. Testing began with the system off at room temperature, i.e. no warm-up of the system before recording data. Over 20 hours of data were recorded with the radiometer in total power mode looking at the internal matched load. As shown in Figure 2.41, four distinct regions of equilibrium were measured during this time. The PCB and MCM exhibit thermal stability of 0.1 K after 60 minutes, as shown in Figure 2.42. Even the noise diode, which was not under active thermal control, had physical temperature variations of less than 1.0 K over this time period. These variations do not affect the matched load measurements because the switch has an isolation of 38.5 dB. Over the

² September 18 and 19, 2011 long term data with $m = 2.236 \text{ mV/K}$ and $b = 3.0028$.

20 hours of continuous data, the drain current, as shown in Figure 2.42, exhibits minor variations, which are uncorrelated with the power detector output voltage.

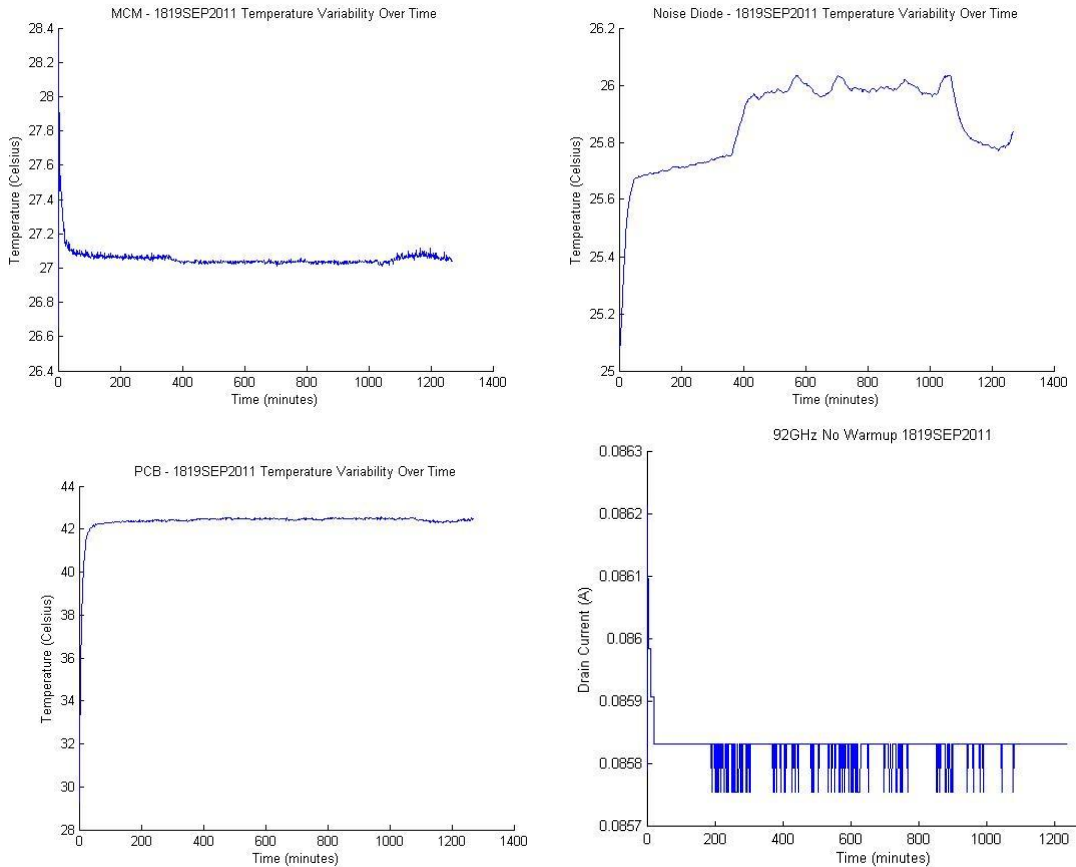


Figure 2.42: Long term 92 GHz MCM, PCB, and noise diode temperature data as well as drain current measurements.³

Therefore, the four regions of equilibrium in Figure 2.41 result from different thermal behaviors that can be measured at the data acquisition and control board and on the surface of the MCM housing. There are several potential causes for the different regions of equilibrium. First, thermal gradients in the MCM could change the matched load power or the amount of switch insertion loss or isolation, which is unlikely due to the tens of Kelvin increase over eight hours in Region 2. The LNAs are the most likely cause for this drift. The LNAs are active devices and dissipate power in the form of heat. While this heat dissipation due to the LNAs is not measured

on the outside surface of the MCM, it could result in a significant change in gain which affects the measured matched load output voltage. These changes in output voltage occur at such a slow rate that performing calibrations every few minutes will reduce the error to acceptable levels. Region 3 is easily identifiable as the region with the most stable response with a slope two orders of magnitude less than the other three regions. As a result, Region 3 data will be analyzed in terms of Allan deviation in Section 2.7.6.

2.7.5 Results

While the testing of individual components verified their performance, the 92 GHz radiometer was tested using three criteria. These were measuring the receiver noise temperature, determining the accuracy of its internal calibration, and analyzing long term system stability through Allan deviation calculations [25].

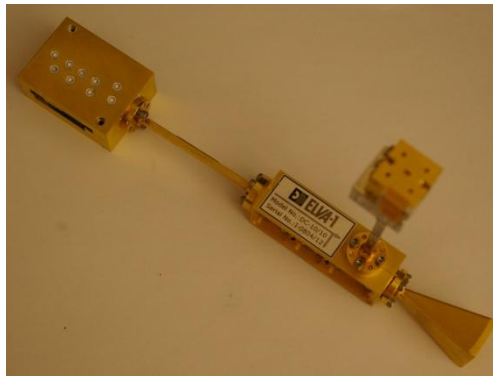


Figure 2.43: 92 GHz radiometer configuration used for testing, without thermal control.

The 92 GHz system test setup involves a standard WR-10 horn antenna followed by an ELVA 10 dB coupler, 3" waveguide through line, and MCM with the noise source connected to the coupler through an isolator, as shown in Figure 2.43. Thermal insulation was used around all components, and active thermal control using a Peltier mounted on the MCM. Thermal equilibrium was assured by letting the system warm up overnight for 14 hours.

2.7.5.1 Measured Receiver Noise Temperature

The receiver noise temperature was determined using the Y-factor method, which is accomplished by measuring the power or brightness temperature of two loads at two different temperatures and calculating the noise temperature [12] as

$$Y = \frac{N_1}{N_2} = \frac{V_1}{V_2} > 1 \quad (2.7)$$

$$T_e = \frac{T_1 - YT_2}{Y - 1} \quad (2.8)$$

where V_1 and V_2 are the power detector output voltages corresponding to microwave absorber physical temperatures of T_1 and T_2 . Y is the ratio of these output voltages, and the receiver noise temperature is T_e (K). The microwave absorber used for testing, as shown in Figure 2.44, was the IS-005A from TDK RF Solutions, Inc. with a minimum of 50 dB of absorption across the W-band. Microwave absorbers were at temperatures of 297.4 K and 77.6 K during testing. When performing Y-factor measurements, it is essential to take into account the offset voltage. The offset voltage is the measured output voltage of the power detector when the LNAs are off. This offset is constant during a single test and is a result of a potential difference between the MCM ground and the data acquisition PCB ground at the ADC.



Figure 2.44: 92 GHz testing without thermal control [26].

The experimental data for the Y-factor measurements are listed in Table 2.6. The cold load data were truncated to 560 samples due to condensation on the microwave absorber. For the test at $t = 300$ minutes, the warm load data were truncated to 730 samples due to excess noise.

Table 2.6: Y-factor measurements for the 92 GHz radiometer.³

Time (min)	Warm (V)	std (V)	W Offset (V)	Cold 560 (V)	std (V)	C 560 Offset (V)	Y	Noise Temperature (K)
0	3.6467	0.00140	3.70790	3.129	0.001	3.1902	1.1623	1277
0	3.6467	0.00110	3.70790	3.1256	0.00087	3.1868	1.1635	1266
0.5	3.6482	0.00100	3.70940	3.1272	0.00094	3.1884	1.1634	1267
10	3.6471	0.00120	3.70830	3.1251	0.00072	3.1863	1.1638	1264
20	3.6482	0.00160	3.70940	3.1291	0.00859	3.1903	1.1627	1273
30	3.6515	0.00110	3.71270	3.1313	0.00094	3.1925	1.1629	1271
45	3.6481	0.00110	3.70930	3.1302	0.00081	3.1914	1.1623	1277
60	3.6461	0.00096	3.70730	3.1291	0.0014	3.1903	1.1621	1278
90	3.6451	0.00140	3.70630	3.1278	0.001	3.1890	1.1622	1277
120	3.6396	0.00130	3.70080	3.1239	0.00088	3.1851	1.1619	1280
180	3.6421	0.00110	3.70330	3.1231	0.00098	3.1843	1.1630	1271
240	3.6446	0.00083	3.70580	3.1241	0.0012	3.1853	1.1634	1267
300	3.6393	0.001	3.7005	3.1214	0.001	3.1826	1.1627	1273
360	3.6262	0.00130	3.68740	3.1055	0.0026	3.1667	1.1644	1259

The average measured receiver noise temperature is 1271 K with a 6 K standard deviation, for the data listed in Table 2.6. This is lower than the calculated noise temperature of 1545 K as shown in Table 2.2. The drain current for this test was 85.8 mA, more than the 40 mA per LNA specified by the manufacturer to yield a 3.0 dB noise figure. Since the noise figure for this LNA is only specified at 40 mA of drain current, the higher current of 42.9 mA could result in a higher than expected gain and lower than expected noise figure. Both the waveguide-to-microstrip transition and PIN-diode switch, which come before the first LNA, have some uncertainty associated with their insertion loss measurements, so their actual insertion loss may

³ 92 GHz Y-factor testing on September 15, 2011. The radiometer configuration consisted of a noise diode with isolator, and a standard WR-10 horn antenna, as well as active and passive thermal control.

be less than measured. All of these considerations contribute to the lower than expected receiver noise temperature.

The radiometric resolution ($NE\Delta T$) of the 92 GHz radiometer is shown in Figure 2.45 as a function of integration time. It is better than both the MHS and AMSU sounders at 89 GHz, which do not have internal calibration. The radiometric resolution calculations assume a $\Delta G/G$ of 1.6×10^{-4} . This variation was determined using (1.8) with the measured receiver noise temperature of 1271 K and the measured Allan deviation of 0.22 K at 8 s, as discussed in Section 2.7.6.1, along with a T_A of 100 K and B of 6.8 GHz. The Dicke radiometric resolution used the same parameters as well as a T_{REF} of 301 K.

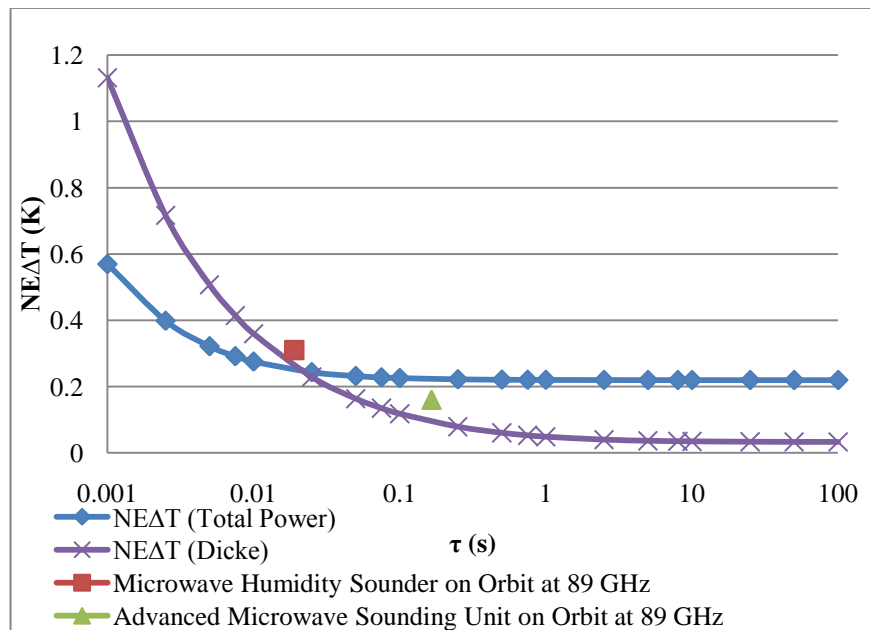


Figure 2.45: $NE\Delta T$ for the 92 GHz radiometer based upon measured receiver noise temperature.

2.7.5.2 Internal Calibration

An experiment was conducted using the 92 GHz radiometer to analyze the stability of internal calibrations over time with the microwave absorber at 77.6 K as a reference.

Table 2.7: Internal calibration for the 92 GHz radiometer.³

Description	Time (min)	m	b	ND Temp (K)	M Temp (K)
External/Internal	0	0.002356	3.0074	640.3	346.6
External/Internal	0	0.002371	3.0028	638.0	345.3
				W Temp (K)	C Temp (K)
Internal/Test	0.5	0.002377	3.0027	297.3	78.1
Internal/Test	10	0.002382	3.0010	296.9	77.8
Internal/Test	20	0.002375	3.0022	297.8	79.2
Internal/Test	30	0.002373	3.0071	297.4	78.1
Internal/Test	45	0.002381	3.0007	297.6	80.1
Internal/Test	60	0.002374	3.0015	297.3	79.5
Internal/Test	90	0.002383	2.9969	297.6	80.6
Internal/Test	120	0.002375	2.9964	296.6	79.5
Internal/Test	180	0.002370	2.9965	298.3	79.3
Internal/Test	240	0.002373	2.9995	297.6	78.3
Internal/Test	300	0.002369	2.9945	298.1	79.4
Internal/Test	360	0.002365	2.9830	297.9	77.7

Initially, two external calibrations were performed to determine the antenna referred noise diode and matched load brightness temperatures, 639.2 K and 346.0 K, respectively. These values are averages and were assumed to be constant during the subsequent internal calibrations. The noise source was biased with 11.4 V and 15.2 mA but was only turned on 10 s prior to each internal calibration to reduce the drift between calibrations from the noise diode warming up. The noise source did not have a good input match, so a waveguide isolator was used between the noise diode and directional coupler during testing. The isolator ensured that no reflections occurred between the noise diode and the directional coupler. While the noise source matching was not optimized as part of this project, this would eliminate the need for an isolator in the final radiometer. The four measurements performed in the same order for each test were as follows: the noise source on with the room temperature microwave absorber, internal matched load, room temperature absorber with the noise source off, and microwave absorber in LN₂. All measurements were taken for approximately 20 s, and the results are shown in Table 2.7. The

noise diode has a consistent temperature, as shown in Figure 2.46, so using the average from both external calibrations at $t = 0$ is reasonable. This measurement could be more stable by testing in Dicke mode as discussed in Section 4.4.

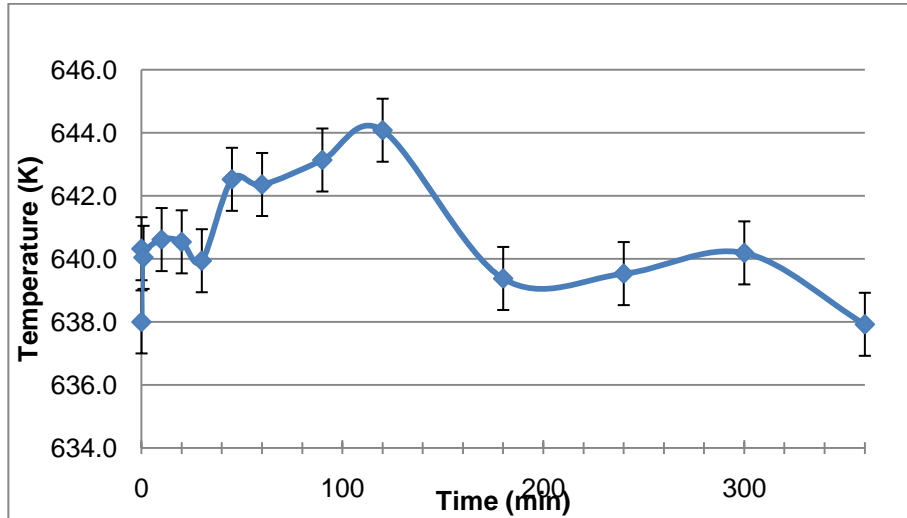


Figure 2.46: 92 GHz noise diode temperature with error bars. 3

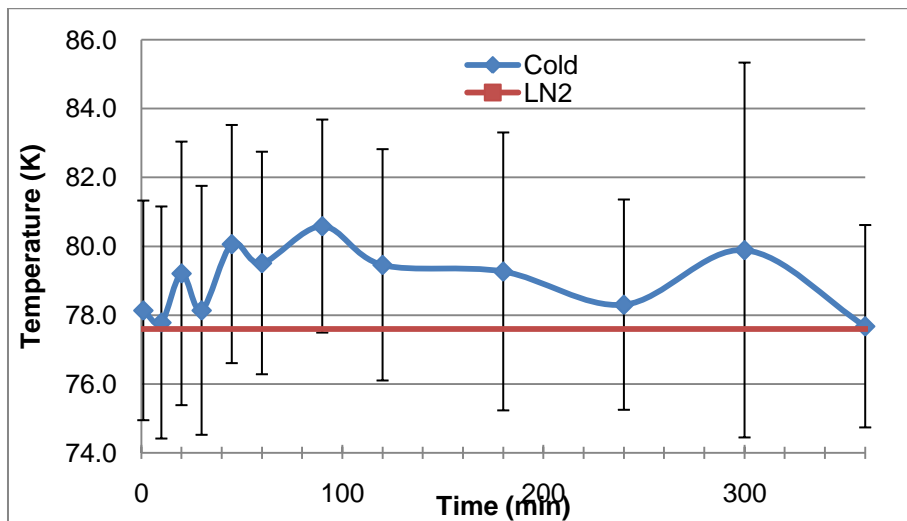


Figure 2.47: LN₂ temperature based upon internal calibration with error bars. 3

The results of the calculated LN₂ temperature in Figure 2.47 show good agreement with the expected 77.6 K value. While all the results are greater than 77.6 K, this is expected because the cold microwave absorber is removed from the LN₂ and manually placed in front of the

antenna for measurement. The error associated with these results is approximately ± 3.6 K.

Subsequent analysis will attempt to determine the most significant factors contributing to this error.

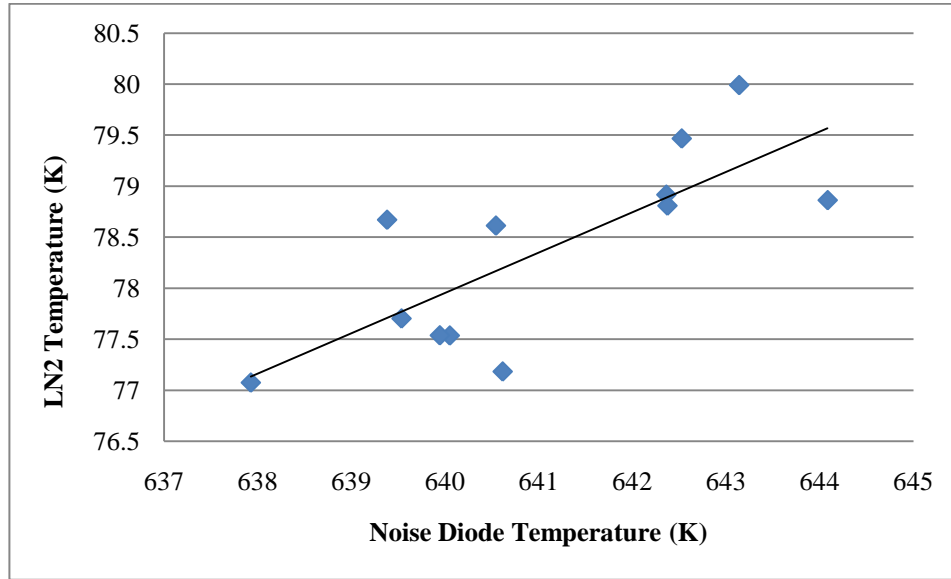


Figure 2.48: Comparison between the measured equivalent noise temperature of the noise diode and that of the LN₂ absorber.

The equivalent noise temperature of the noise diode and that of the cold absorber have a strong correlation of 0.771, as shown in Figure 2.48. The measured variability in noise source power is not unexpected since the noise diode is an active component. Other factors, which may contribute to the error in the cold absorber temperature, are subsequently considered.

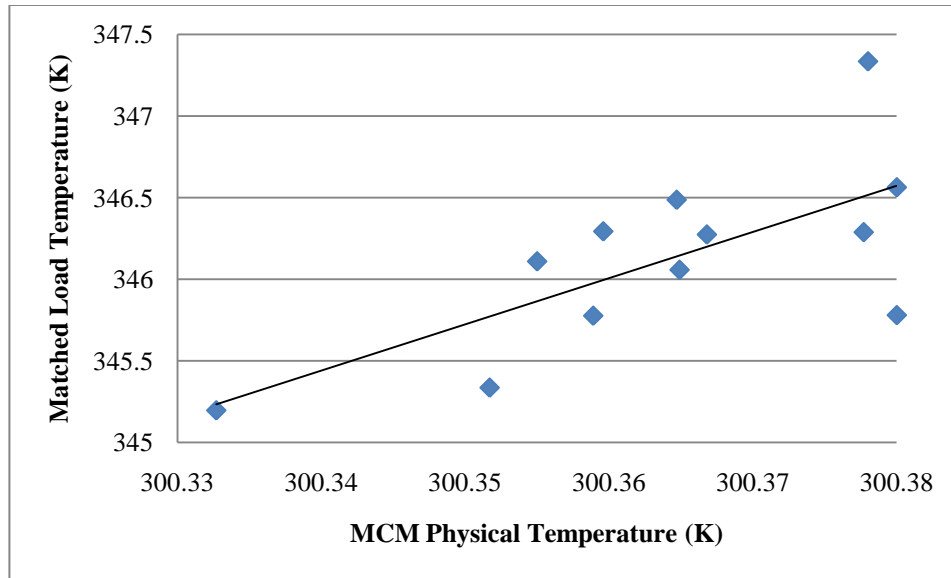


Figure 2.49: Comparison between the physical temperature of the MCM and the matched load brightness temperature.

The matched load temperature and the physical temperature of the MCM have a strong correlation of 0.695, as shown in Figure 2.49. This is expected since the noise power output of the matched load is a direct result of thermal noise. Although this variability in the matched load temperature will affect the accuracy of the internal calibration, the variability in the MCM physical temperature is 0.01 K and unlikely to be the major contributor. The reasonable correlation of 0.574 between the noise diode temperature and the MCM physical temperature helps to corroborate this conclusion, as shown in Figure 2.50.

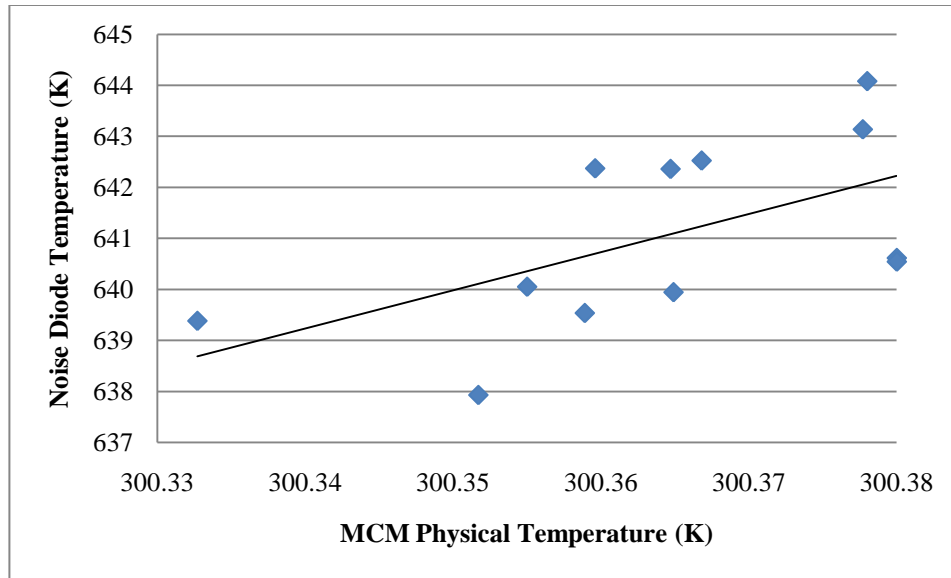


Figure 2.50: Comparison between the physical temperature of the MCM and the noise diode temperature.

The comparison in Figure 2.51 demonstrates a poor correlation of -0.297 between the physical temperature of the noise diode and the equivalent noise temperature of the cold absorber. Based upon this analysis, the largest contributor of error to the cold absorber temperature determination is the output power variability of the noise diode.

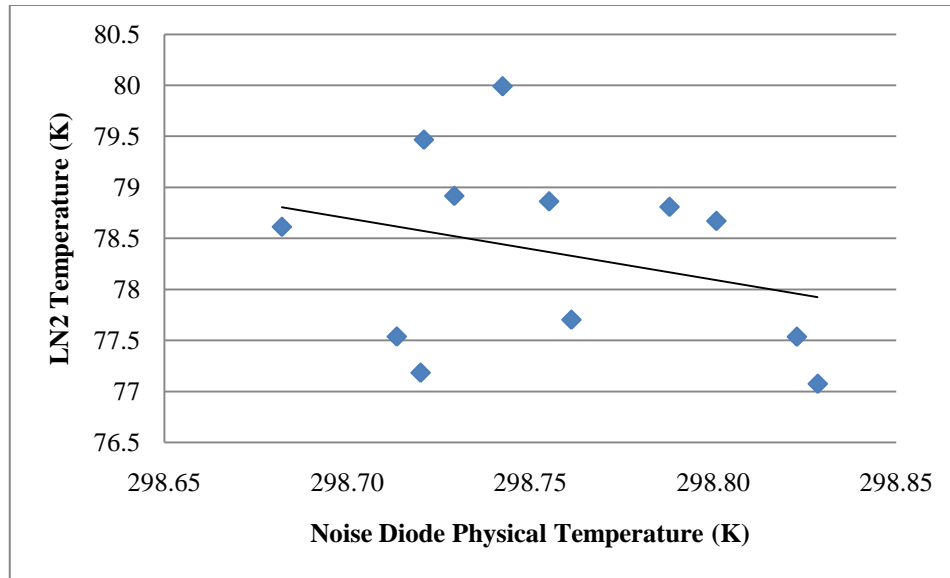


Figure 2.51: Comparison between the noise diode physical temperature and the cold absorber temperature.

2.7.6 Long Term Radiometer Stability

Long term data was taken with the 92 GHz radiometer looking at the internal matched load with active thermal control. This long term stability analysis does not focus on the temperature stability, which was covered in Section 2.7.4, but instead will address the effect of noise through an Allan deviation calculation. Region 3 of the overnight data shown in Figure 2.41 is used for this analysis since it is the most thermally stable. The temperature data for this region is shown for the MCM in Figure 2.52 and the noise diode and PCB in Figure 2.53. These reaffirm the high degree of temperature stability for this region, as mentioned in Section 2.7.4.

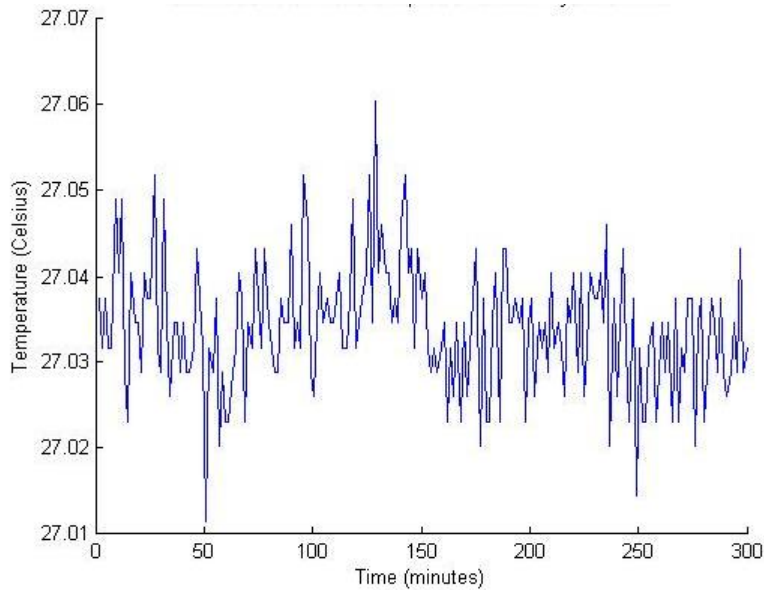


Figure 2.52: MCM physical temperature data for Region 3 matched load data.⁴

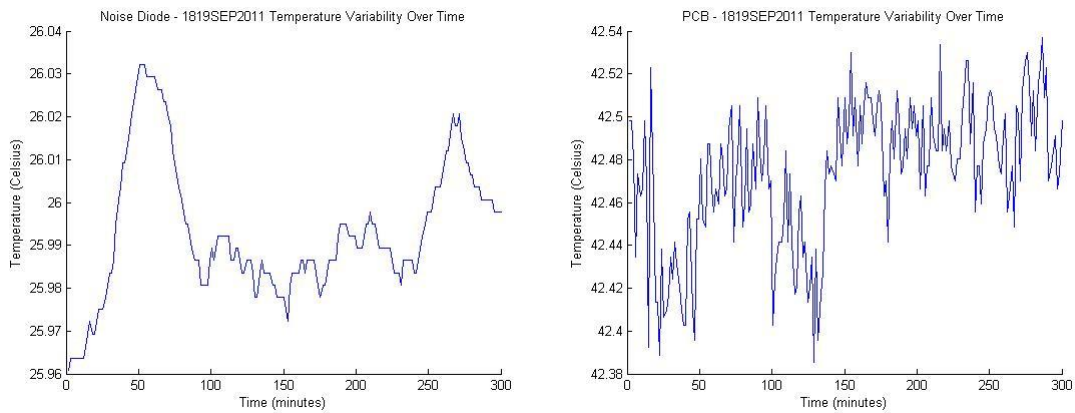


Figure 2.53: Noise diode and PCB temperature data for Region 3 matched load data.⁴

2.7.6.1 Allan Deviation

An Allan deviation calculation was performed for the five-hour time series of matched load equivalent noise temperature shown in Figure 2.54. It has a mean value of 357.4 K with a 1.0 K standard deviation. The calibration coefficients used to determine this temperature result from external calibrations done several days prior and so the voltage to temperature conversion is

⁴ 92 GHz radiometer matched load temperature data from September 18 and 19, 2011 of Region 3 (samples 2.2×10^6 to 3.2×10^6 data and 436 to 635 temperature).

not exact. Besides the data to be analyzed, the sampling frequency of 56 Hz and a series of τ divisible by the sampling frequency are used as inputs.

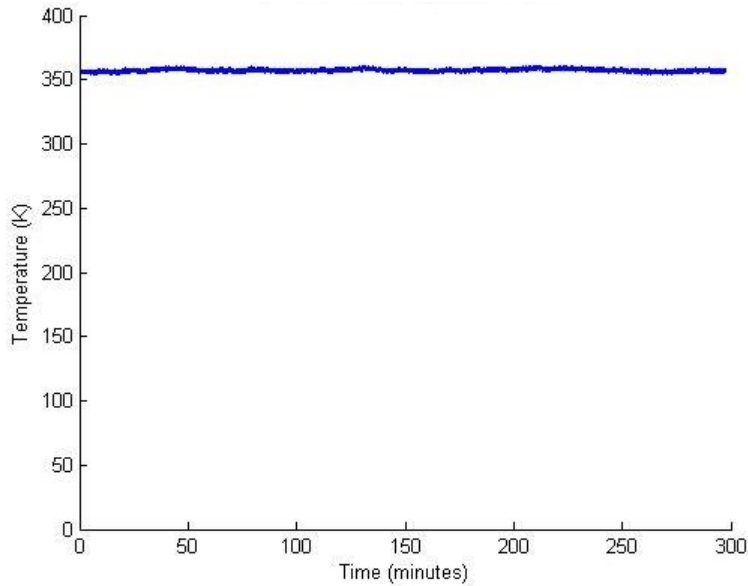


Figure 2.54: Matched load equivalent noise temperature using previous calibration coefficients for Allan deviation analysis.⁵

The τ values used were 0.125, 0.25, 0.5, 1, 2, 4, 8, 16, 32, 64, 128, 256, 512, and 1024 s.

As shown in Figure 2.55, the Allan deviation calculation shows a minimum at 8 s with a value of 0.22 K. This corresponds to the *NEAT* at long integration times.

⁵ September 18 & 19 overnight matched load data, samples 2.2×10^6 to 3.2×10^6 with $m = 2.236$ mV/K and $b = 3.0028$.

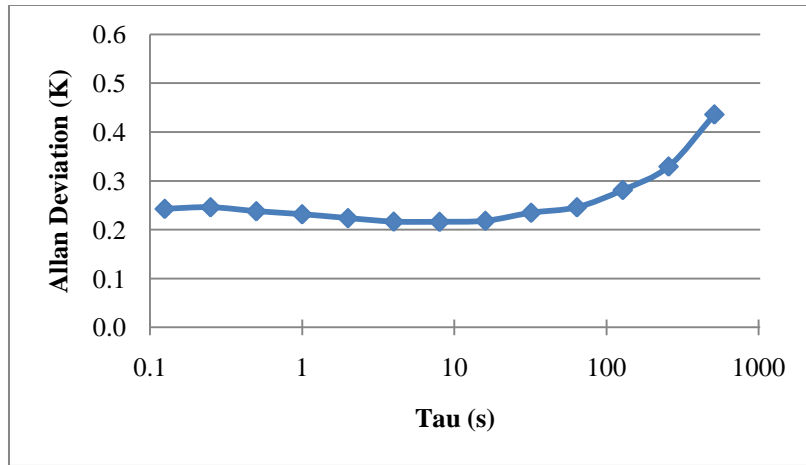


Figure 2.55: Allan deviation of matched load equivalent noise temperatures in Figure 2.54.5

Chapter 3

130 GHz Radiometer Design and Test

3.1 Block Diagram

The receiver architecture for the 130 GHz radiometer is direct detection and enables a lower receiver noise temperature than a superheterodyne architecture, as discussed in Section 1.3.2. A switch was used to enable internal calibration and operation as a Dicke radiometer.

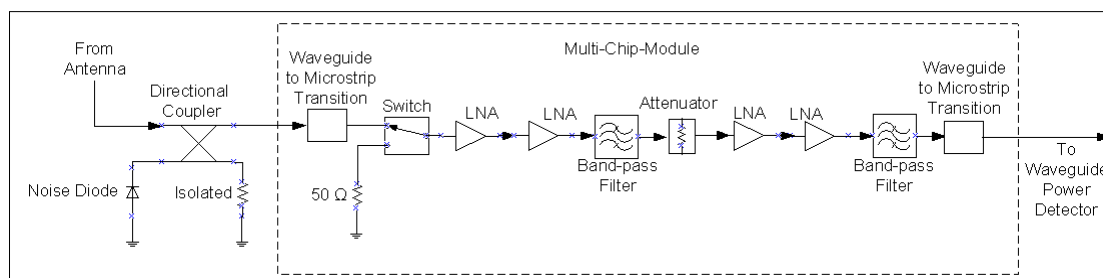


Figure 3.1: Block diagram of the 130 GHz radiometer.

There are several minor differences between the 130 GHz radiometer architecture and that of the 92 GHz radiometer. Four MMIC LNAs are used instead of two to obtain sufficient receiver gain and two bandpass filters instead of one, a wide filter followed by a narrow one. The other major difference not shown in Figure 3.1 is the need for impedance matching circuits to account for the wire bond inductance. The directional coupler, noise diode, and power detector are all waveguide components. All of the components inside of the multi-chip-module are MMIC components. The active components, such as the switch and LNAs, were developed by JPL, while the passive components, waveguide-to-microstrip transition, matched load, bandpass filters, attenuators, and interconnects were designed as part of this thesis.

3.2 Predicted Noise Temperature and Radiometric Resolution

A noise temperature analysis was performed to characterize the 130 GHz radiometer and determine its radiometric resolution. The components for the direct detection architecture with Dicke switching, along with their gain or loss and noise figure, are listed in Table 3.1. The loss of the directional coupler, interconnect attenuators, bandpass filters, and attenuator were measured at JPL using the Agilent 8510C network analyzer with a 90-140 GHz (F-band) RF probe station. The losses of the switch as well as the gain and noise figure of the LNAs were provided from previous individual component measurements at JPL. The loss of the 1-inch waveguide through line from QuinStar Inc. was not directly measured but inferred from a 3-inch WR-08 through line measurement. The waveguide-to-microstrip transition loss is an adjusted simulation value, just as was used for the 92 GHz version. The calculated cumulative receiver noise temperature of this radiometer configuration is 1328 K.

Table 3.1: Final 130 GHz radiometer theoretical noise analysis based upon measured component values.

Component	Vendor	Gain (dB)	Noise Figure (dB)	Cumulative Noise Temperature (K)
Directional Coupler	ELVA	-1.3	1.3	101
Waveguide Through Line	QuinStar	-0.3	0.3	129
Waveguide-to-Microstrip transition	MSL	-0.5	0.5	180
Switch	JPL	-1.9	1.9	438
LNA	JPL	18	3.3	1267
Interconnect Attenuator	MSL	-2.8	2.8	1282
LNA	JPL	18	3.3	1282
Interconnect Attenuator	MSL	-2.8	2.8	1312
Wide BPF	MSL	-1.25	1.25	1313
Attenuator	MSL	-4.15	4.15	1315
Interconnect Attenuator	MSL	-2.8	2.8	1319
LNA	JPL	18	3.3	1327
Interconnect Attenuator	MSL	-2.8	2.8	1349
LNA	JPL	18	3.3	1349
Interconnect Attenuator	MSL	-2.8	2.8	1328
Narrow BPF	MSL	-3.25	3.25	1328
Waveguide-to-Microstrip transition	MSL	-0.5	0.5	1328
Receiver Gain (dB)	41.6			
Receiver Noise Factor	5.6			
Receiver Noise Figure (dB)	7.5			
Receiver Noise Temperature (K)	1328			

The total power radiometric resolution is shown in Figure 3.2 as a function of integration time with a 1328 K noise temperature, 5.25 GHz bandwidth, antenna temperature of 100 K, and gain variations of 1.34×10^{-3} . The $\Delta G/G$ was determined from (1.8) using the measured receiver noise temperature in Section 3.7.4.1 and the measured Allan deviation in total power mode in Section 3.7.5.1. The Dicke $NE\Delta T$ shown in Figure 3.2 uses a T_{REF} of 301 K. The Dicke radiometric resolution is comparable with that of the Microwave Humidity Sounder and the

Advanced Microwave Sounding Unit at 157 GHz and 89 GHz respectively. These radiometers on orbit do not have internal calibration.

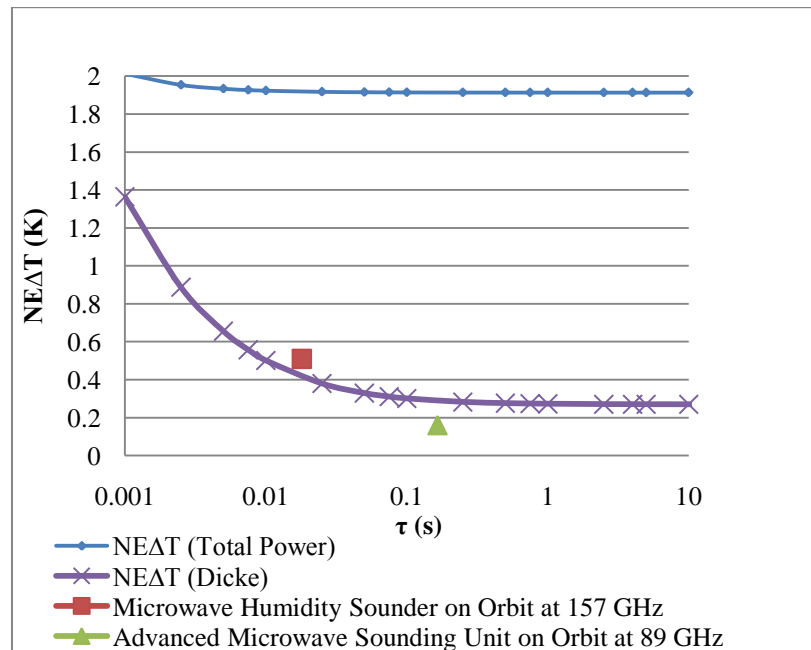


Figure 3.2: Realistic radiometric resolution plot for the 130 GHz radiometer using 1328 K and a 5.25 GHz bandwidth.

3.3 Gain Requirements

The approach for calculating the RF system gain requirements was discussed in Section 2.3, so a detailed discussion will not be presented here. To summarize, the RF gain, receiver noise temperature, minimum and maximum measured scene temperatures, and the radiometer bandwidth will be used in conjunction with (1.6) to calculate the expected minimum and maximum values of input power to the 130 GHz power detector.

The expected maximum input power to the detector is -27.0 dBm, as listed in Table 3.2. This power level falls within the square-law region for these zero-bias detectors with a maximum input power of -20 dBm. For comparison, when measuring the voltage output of the detector when looking at the matched load at a thermal equilibrium of 301 K, the input power to the

detector is calculated to be -39.9 dBm, using the detector's sensitivity of 1423 V/W. This power is 12.1 dB, or a factor of 16.3, less than expected from Table 3.2.

Table 3.2: Input power calculation to the power detector of the 130 GHz radiometer based upon implemented and measured radiometer component configuration and values.

System Gain (dB)	T_{sys} (K)	T_a (K)	Bandwidth (GHz)	Beta (V/W)	Power (dBm)
41.6	1328	600	5.25	1423	-27.0
41.6	1328	297	5.25	1423	-27.7
41.6	1328	77	5.25	1423	-28.4

3.4 Commercially Available Components

3.4.1 ELVA Coupler

As discussed in Section 1.3.4, the directional coupler enables the addition of a hot calibration load with minimal loss and no moving parts. The directional coupler is a waveguide device in the 130 GHz radiometer. Its insertion loss was measured using JPL's F-band RF probe station setup to be -1.3 dB, as shown in Figure 3.4. This loss is less than that of an active MMIC switch.



Figure 3.3: 130 GHz 10-dB waveguide directional coupler from ELVA.

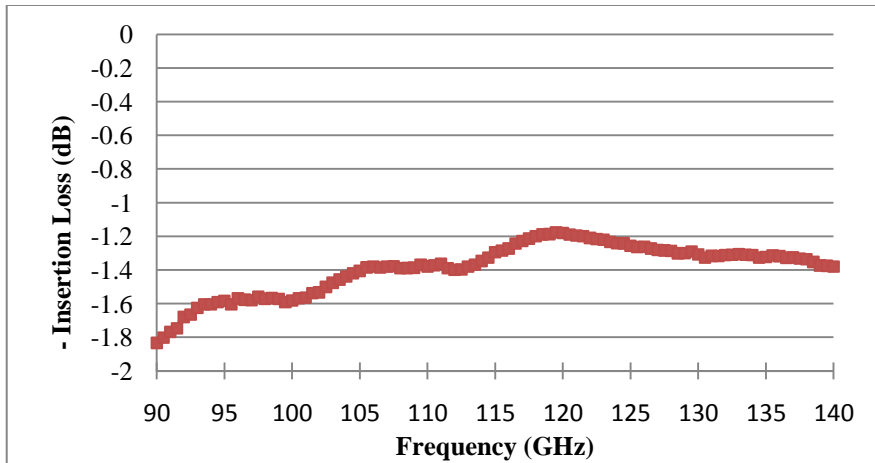


Figure 3.4: Insertion loss of the 130 GHz ELVA 10 dB coupler.

The coupling of the ELVA directional coupler was measured to be 9.2 dB in Figure 3.5, slightly less than the expected 10 dB. This measurement was conducted with a matched load at the input port of the coupler.

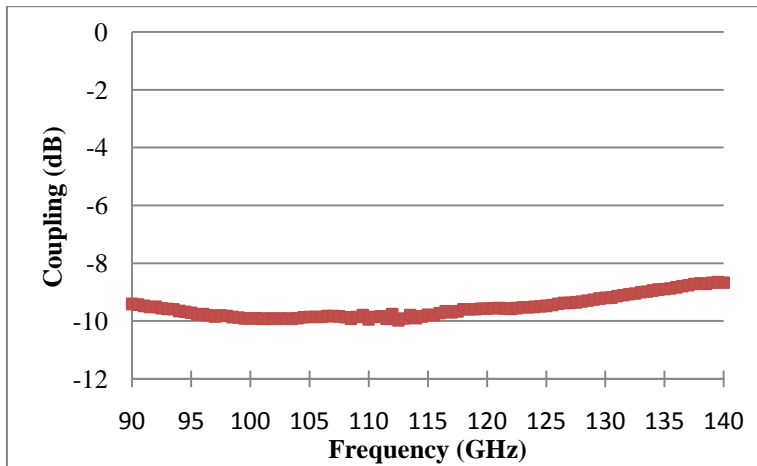


Figure 3.5: Coupling factor in dB of 130 GHz ELVA 10 dB coupler

3.4.2 Pacific Millimeter Products Detector

While the power detector used at 130 GHz is a zero bias detector, the same as used in the 92 GHz radiometer, several differences other than their frequency of operation exist between the two. This detector has a sensitivity of 1423 V/W at 130 GHz, is packaged in a WR-08 waveguide housing with an SMA output, and has a negative voltage output.



Figure 3.6: 130 GHz zero bias waveguide detector with negative voltage output.

This power detector operates in the square-law region up to a maximum power of -20 dBm. This is 10 dB higher than the 92 GHz power detector described in Section 2.4.4. The waveguide packaging allows for the possibility of additional testing by adding a down converting mixer to the radiometer output so that the radiometer can be more precisely characterized over frequency. The SMA output provides a robust connection to the SMA input of the data acquisition PCB. This waveguide detector has a greater susceptibility to noise than a MMIC detector because gain cannot be added inside the MCM but instead must be added on the data acquisition and control board. Additionally, if the detector becomes damaged, the whole detector assembly must be replaced, but conclusions drawn from testing the 92 GHz radiometer will help prevent damage.

3.5 Components Designed at JPL

3.5.1 Tri-Frequency Feed Horn

The tri-frequency feed horn was designed, fabricated, and characterized by JPL operates at 92, 130, and 166 GHz. It was designed to achieve a 10 GHz bandwidth corresponding to an input return loss requirement of 15 dB.

3.5.2 Noise Source

The 130 GHz noise source is a beam-lead diode from M-Pulse Inc. that was manufactured for NASA's Goddard Space Flight Center as part of a Small Business Innovation Research program [20] [8]. It is the same beam-lead diode used for the 92 GHz noise source with different packaging and biasing. Although the WR-08 housing for the beam-lead diode was not optimized, an 8 dB and 4 dB ENR was measured for two versions. This corresponds to brightness temperatures of 510 K and 377 K, respectively, after the measured 9.2 dB coupling of the 130 GHz ELVA coupler. The 4 dB ENR noise source was used in the 130 GHz internal calibration.

3.5.3 PIN-Diode Switch

An SPDT PIN-diode switch was designed by JPL and produced using Northrup Grumman's 75 μm thick InP wafer process technology to operate between 90 and 135 GHz. This encompasses the bandwidth of the 130 GHz radiometer. This MMIC switch development was necessary because no commercially available MMIC SPDT switches are known to be available at these frequencies.

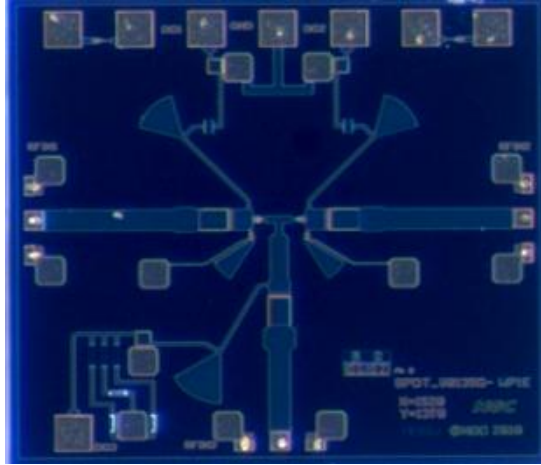


Figure 3.7: 90-135 GHz symmetric MMIC PIN-diode switch design [15].

Without a switch at 130 GHz, neither internal calibration nor Dicke switching would be possible. Not only does the switch have a small form factor of 1.37 by 1.52 mm, but it has a low insertion loss of 1.9 dB. The input return loss is better than 15 dB, meeting the design goals, but the isolation is only 8 dB instead of the desired 20 dB. While the isolation did not meet the target, it can be tuned in the same manner as discussed in Section 2.5.3. This lack of isolation could affect the precision of the internal calibration.

3.5.4 LNA

The LNAs used in the 130 GHz radiometer were designed by JPL and produced using the 35 nm InP HEMT (high electron mobility transistor) process from Northrup Grumman. Measurements by JPL are shown in Figure 3.8[22]. This LNA has an average gain of 18 dB with a 3.3 dB noise figure at 130 GHz.

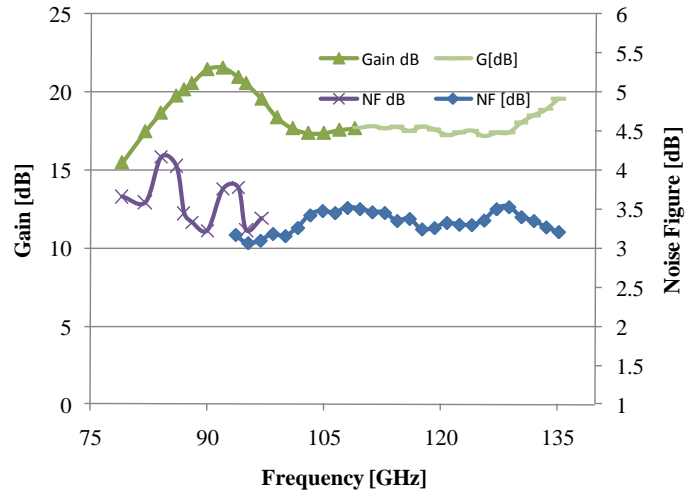


Figure 3.8: Gain and noise figure measurements for 140LNA [27].

As discussed in previous sections, minimizing the loss before the first gain stage is essential to minimizing the cumulative receiver noise temperature, as shown by (1.14). The biasing for these LNAs is 0-0.2 V for its gates and 0.75-1.0 V for its drain with 15-20 mA of current. The gate biasing of these LNAs was implemented using voltage dividers inside of the MCM and their biases were highly variable at 0.05 to 0.21 V with a drain bias of 0.7 V.

3.6 Components Designed at CSU MSL

3.6.1 Waveguide-to-Microstrip Transition Design

A waveguide-to-microstrip probe transition enables the coupling of electromagnetic energy from the waveguide to microstrip. Several modifications were made to the 92 GHz design discussed in Section 2.6.1. The transition was designed and fabricated on 3 mil thick polished alumina substrate with 0.1 mil thick gold microstrip lines. A dielectric constant of 9.7 and loss tangent of 0.0002 were used in the Djordjevic-Sarkar model for the alumina substrate in the Ansoft HFSS simulation.

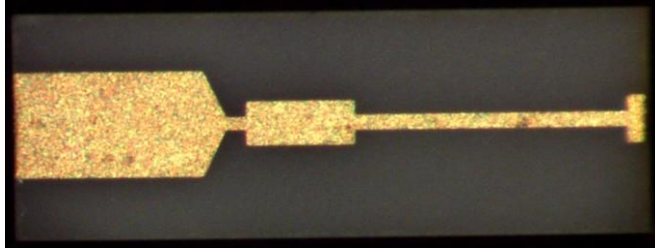


Figure 3.9: 130 GHz waveguide-to-microstrip probe transition

The layout of the 130 GHz waveguide-to-microstrip transition probe follows the same design principles as the 92 GHz version. The opening in the waveguide for the probe has a cutoff frequency of 236 GHz. The paddle on the left in Figure 3.9 does not have backside metallization underneath it and is optimized so that the frequency response of the probe has the smallest impedance change over the 130 GHz radiometer's frequency range. On the right side of the paddle is an angular transition into the high impedance transmission line. This angular transition reduces the effect of an inexact placement i.e. if part of the paddle is not in the waveguide or vice versa. A vertical line in gold could have been added to indicate proper placement but would need to be included in the simulation to ensure no adverse effects on the frequency response. To the right of the high impedance line is a wider segment that is a quarter-wave impedance transformer to 50Ω . To its right is another high impedance line to tune out the wire bond inductance at these frequencies. The inductance of the wire bonds has a significant effect on the matching of the component at frequencies above 100 GHz. Individual interconnects will be used to tune out the wire bond inductance for components elsewhere in the RF trench but can be incorporated into the design of the waveguide-to-microstrip transition. Two major difficulties arise in adding a high impedance line to tune out the wire bond inductance. One source of error is accurately modeling the wire bond because creating the exact wire bond used in the simulation in the assembly process is difficult and affects the tuning. The other issue is that the wire bond electrically connects an alumina substrate to one made of InP at

the input and to one of alumina at the output, which makes it difficult to optimize the match in only one component. The probe ends on the far right with a short $50\ \Omega$ transmission line for wire bonding purposes.

The probe transition was designed on an alumina substrate with a wire bond that is 6 mils long and 1 mil high using 0.7 mil diameter bond wire. Its simulated input return loss and insertion loss are shown in Figure 3.10 and Figure 3.11, respectively. The input return loss is better than 20 dB, and the insertion loss is approximately 0.25 dB. As mention in Section 2.6.1, the simulated HFSS results are not compared with measured results because fabricating a special test fixture for this purpose would be required.

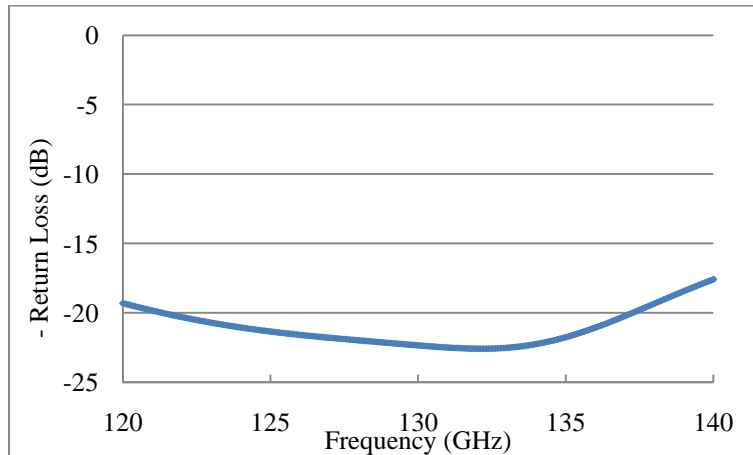


Figure 3.10: HFSS simulation of input return loss of the 130 GHz waveguide-to-microstrip probe transition with wire bond to alumina substrate.

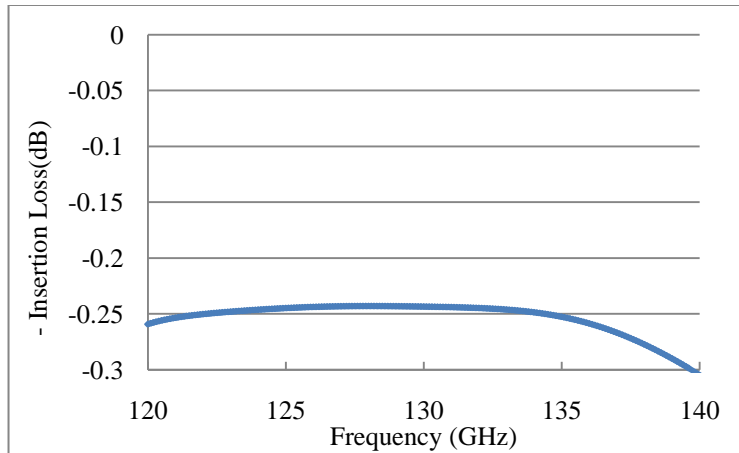


Figure 3.11: HFSS simulation of insertion loss of the 130 GHz waveguide-to-microstrip probe transition with wire bond to alumina substrate.

3.6.2 Matched Load with Virtual Ground – Design and Measurement

The design of the matched load at 130 GHz used the virtual ground topology instead of the ground via version. The virtual ground matched load had a broader frequency response at 92 GHz. The design methodology is the same as the one for the 92 GHz version discussed in Section 2.6.2.1. The only variation is the addition of the high impedance microstrip section to tune out the wire bond inductance.

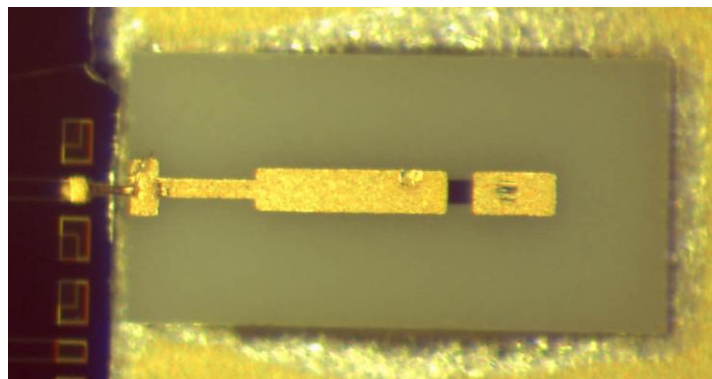


Figure 3.12: 130 GHz matched load with virtual ground measurement configuration.

The same HFSS simulation configuration as the one discussed in Section 3.6.1 was used for the 3 mil thick alumina substrate and 0.1 mil thick gold microstrip. An sq value of $50 \Omega/sq$ was used for the TaN thin film resistor.

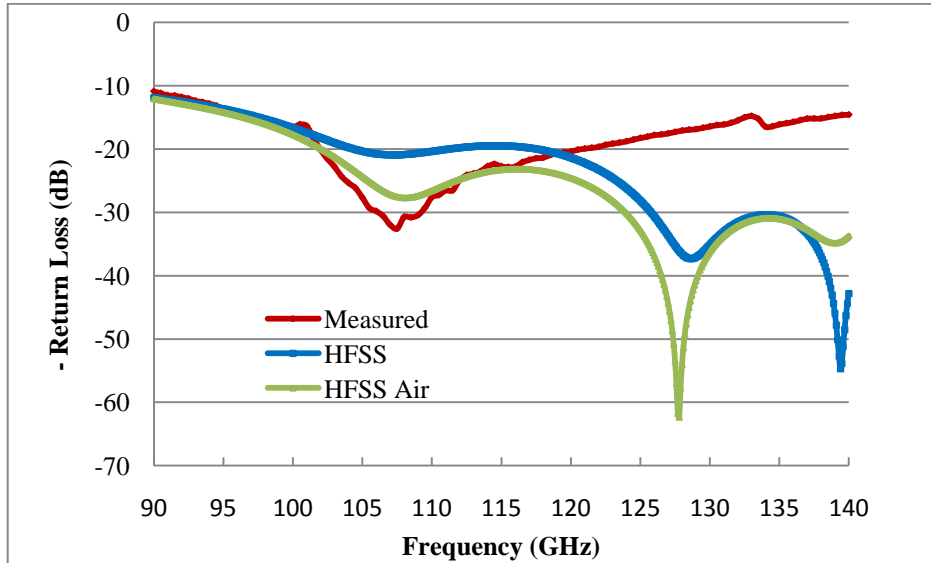


Figure 3.13: 130 GHz matched load comparison of the input return loss between open air measured, HFSS open air simulation, and HFSS cavity results.

The measurements were performed using JPL's WR-08 RF probe station with a coplanar waveguide (CPW) to microstrip transition designed for operation above 100 GHz. The input return loss comparison shown in Figure 3.13 indicates excellent agreement between the measured and simulated results up to 115 GHz. The range of operation of the 130 GHz radiometer is centered at 130 GHz with a 5.25 GHz bandwidth. The matched load has a reduced but sufficient match over that frequency range. The disparity between the simulation and measured results could have several causes. One factor could be that the wire bond which was modeled in HFSS may not correspond exactly to the one used in the matched load testing. Also, the CPW to microstrip transition used to enable probing might have adversely affected the match, although measurements of other components show good agreement.

3.6.3 Interconnects and Interconnect Attenuators

Wire bond inductance has a substantial effect on the matching between components at frequencies above 100 GHz. Passive components referred to as interconnects were designed, fabricated, and tested to tune out this inductance at 130 GHz. These passive components also have smaller dimensions than other RF components in the trench such as the LNAs and bandpass filters, which results in a higher waveguide cutoff frequency. One version of the interconnects was designed to have attenuation as well as the ability to tune out wire bond inductance. This significantly increases the versatility of the design by allowing for attenuation to be added if too much RF gain exists in the system and improve the match between components at the same time. The interconnects are designed and manufactured on a 3 mil thick polished alumina substrate with 0.1 mil thick gold transmission lines, and the attenuator version uses TaN thin film resistors with an sq of 100 Ω/sq .

3.6.3.1 Interconnect Design and Measurement

Since the interconnects are designed to tune out the wire bond inductance, the wire bond model used in HFSS is important for their design. The bond wires are 5 mils long and 1 mil high with a 0.7 mil diameter. As mentioned previously, it is difficult to exactly model the wire bonds which are used in the assembly of the 130 GHz radiometer components, but the model used is reasonable.

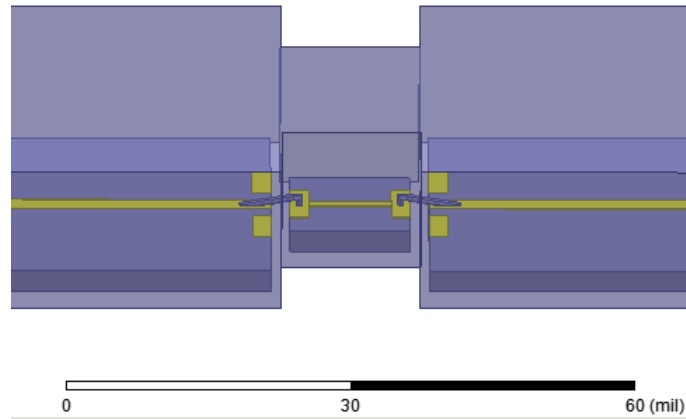


Figure 3.14: HFSS model of 130 GHz interconnect with wire bonds for simulation purposes.

The design process for the interconnects involves adding a short $50\ \Omega$ transmission line at the ends for wire bonding and approximately a quarter-wave high impedance line in between to tune out the wire bond inductance.

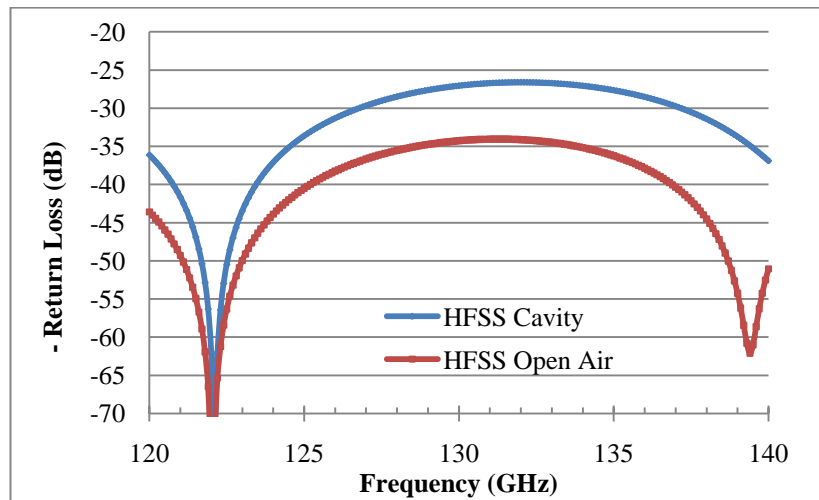


Figure 3.15: Input return loss comparison between the cavity and open air HFSS simulations of the 130 GHz interconnects.

The simulations involve wire bonds to alumina substrates with $50\ \Omega$ gold transmission lines (de-embedded) to accurately reflect testing conditions. The input return loss is better than 25 dB for both the cavity and open air simulations, as shown in Figure 3.15. This level of matching is sufficient for use in the 130 GHz radiometer. The insertion loss is approximately

0.1 dB for both cases at, as shown in Figure 3.16. Due to limitations in CPW to microstrip transitions, the interconnects were not directly tested. Since comparisons between other component HFSS simulations and measurements show good agreement, the frequency responses of the interconnects should be similar to their simulated responses.

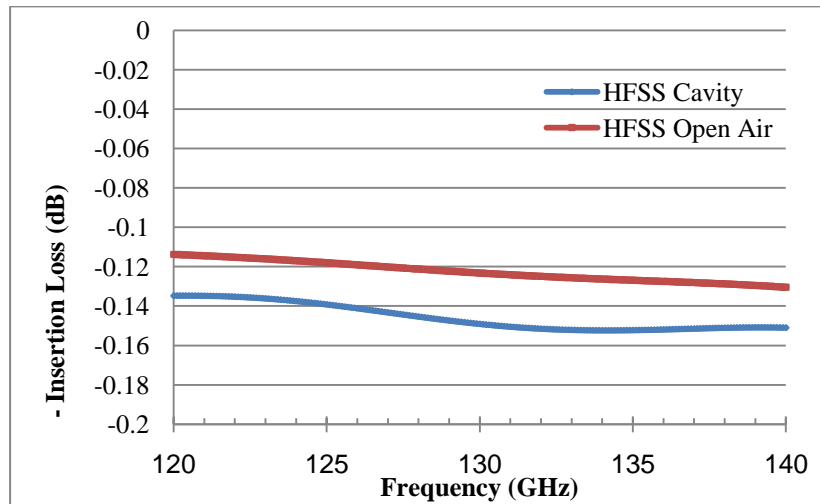


Figure 3.16: Insertion loss comparison between the cavity and open air HFSS simulations of the 130 GHz interconnects.

3.6.3.2 Interconnect Attenuator Design and Measurement

The interconnect attenuator design is simply a combination of the design methods discussed for the interconnect design in Section 3.6.3.1 and attenuator design in Section 2.6.4.1. The interconnect attenuators were designed on 3 mil thick alumina with 0.1 mil thick gold transmission lines. The thin film resistors are made of TaN and use 100 Ω /sq. These resistors do not follow Applied Thin Film's design guidelines, but they were able to fabricate them without any issues.

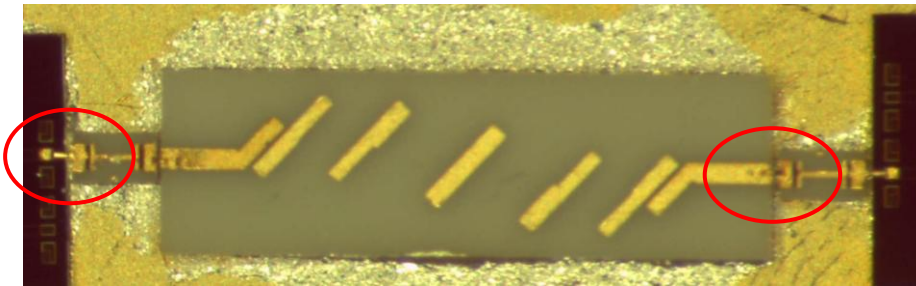


Figure 3.17: Measurement setup of the 130 GHz narrow bandpass filter with interconnect attenuators circled in red.

The interconnect attenuators were designed for approximately 3.5 dB of attenuation. The matching frequency response for the HFSS simulation with wire bonds from alumina substrates is shown in Figure 3.18. The input return loss is better than 15 dB, which is acceptable for their use.

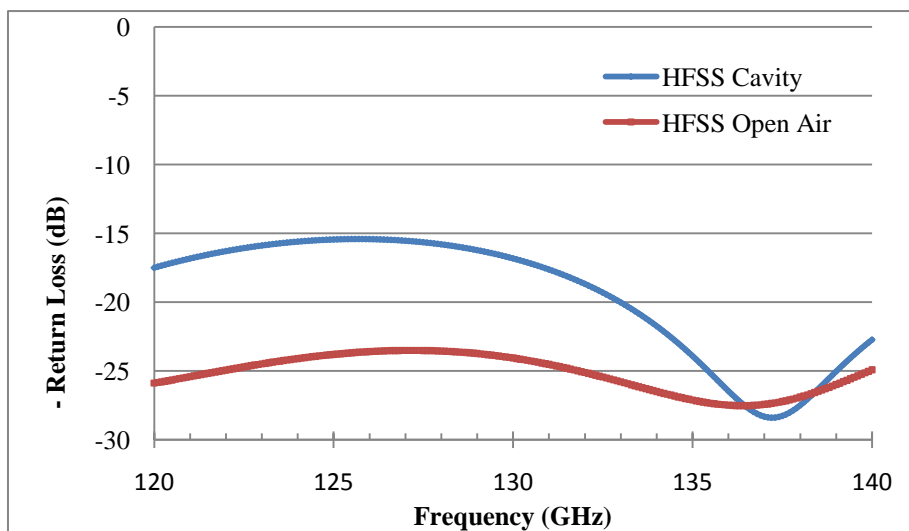


Figure 3.18: HFSS cavity and open air simulation comparison of the input return loss for the 130 GHz interconnect attenuators.

The comparison between insertion loss of the HFSS simulations and measured response is shown in Figure 3.19. The measured insertion loss has an average value of 3.6 dB. This value was obtained by measuring the narrow bandpass filter by itself and subtracting its insertion loss to obtain that of the interconnect attenuators. The difference between the measured and the simulated results is due to errors introduced by removing or de-embedding the insertion loss of

the CPW to microstrip transitions, bandpass filter, and wire bonds. This was done because of the limitations in the availability of custom CPW to microstrip transitions above 100 GHz. Overall, the agreement between the HFSS simulation results for the insertion loss and the de-embedded measurement is good, considering the previously mentioned sources of error.

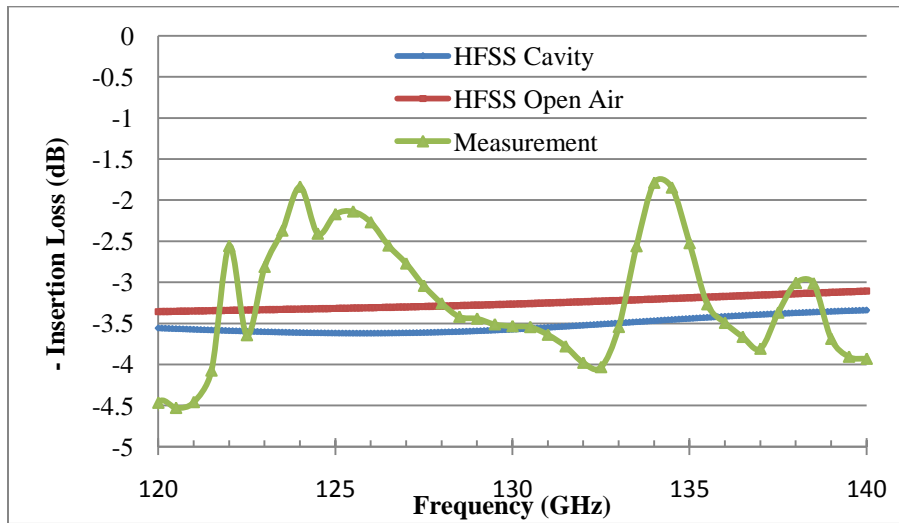


Figure 3.19: HFSS cavity and open air simulation comparison to the de-embedded measured results of the insertion loss for the 130 GHz interconnect attenuators.

3.6.4 Narrow Edge-Coupled Bandpass Filter

3.6.4.1 Design and Optimization

A 5th order Chebyshev bandpass filter configuration was selected for the 130 GHz bandpass filter, which is the same topology as used for the 92 GHz bandpass filter. The 130 GHz filter was designed on 3 mil thick alumina with 0.1 mil thick gold microstrip lines.

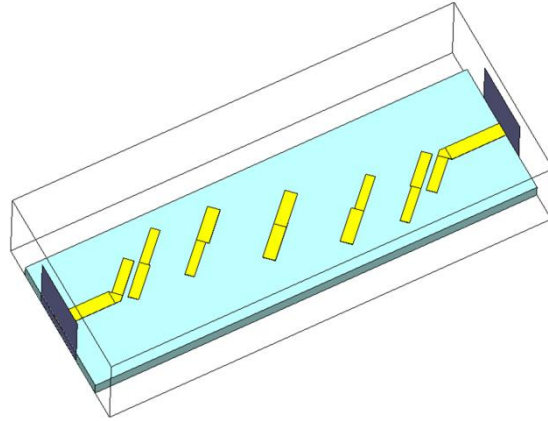


Figure 3.20: HFSS 3-D model of 130 GHz narrow bandpass filter.

The design approach of the 130 GHz bandpass filter utilized the optimization features available in Ansoft Designer and HFSS, while the 92 GHz bandpass filter design employed a more brute force or manual approach. The design of the 130 GHz narrow bandpass filter with a 5 GHz bandwidth followed three main steps, i.e. 1D modeling in Designer, 2.5D modeling in Designer, and 3D modeling in HFSS. The methodology for this design is subsequently described. This approach can be utilized for all microstrip coupled line bandpass filter designs, especially for designs operating on the order of 100 GHz.

Table 3.3: Theoretical bandpass filter calculations for a center frequency of 130 GHz.

Z_o (Ω)	50
Bandwidth (GHz)	5
f_o (GHz)	130
f (GHz)	127.5
Δ	0.0385
ω (rad/s)	1.0098

n	g_n	$Z_o J_n$	$Z_{oe}(\Omega)$	$Z_{oo}(\Omega)$
0	1.0000			
1	0.6180	0.3127	70.52	39.25
2	1.6180	0.0604	53.20	47.16
3	2.0000	0.0336	51.74	48.38
4	1.6180	0.0336	51.74	48.38
5	0.6180	0.0604	53.20	47.16
6	1.0000	0.3127	70.52	39.25

Initially a 1D simulation was performed in Ansoft Designer using the TRL (Through-Reflect-Line) calculator, which is part of the distributed microstrip 2-coupled line model. The values of frequency, bandwidth, Z_{oe} , and Z_{oo} used are shown in Table 3.3. The simulation resulted in a bandpass filter shifted higher in frequency from the desired 130 GHz center frequency. The bandpass filter was shifted lower in frequency to the desired 130 GHz by using the Optimetrics feature of Designer. The length, width, and spacing of the coupled lines are defined in the simulation. The Optimetrics feature allows variables to be altered within a certain range of values to obtain a desired frequency response such as a specific level of input return loss or insertion loss. While this last step is not strictly necessary as it can be combined with the following step, it enables the user to obtain a better understanding of the Optimetrics feature. Then Planar EM, which is the 2.5D feature of Ansoft Designer, can be used with a 3 mil thick alumina substrate and 20 mil high cavity. An angled microstrip bend is used to rotate the coupled line bandpass filter by approximately 46 degrees so that the overall filter width is

reduced at the expense of increasing its length. The filter then was re-simulated and optimized before exporting to HFSS, Ansoft's 3D electromagnetic simulator. While these steps are essentially the same procedure followed during the design of the 92 GHz bandpass filter, one important addition to the procedure was the addition of variables in the rotated coupled line bandpass filter, which enables optimization to be performed automatically with Ansoft's Optimetrics feature. Even though the rotation was performed using simple geometric manipulation, optimization is important due to the large number of variables, as defined in Appendix D. The offset coupled line topology, shown in Appendix D.2 can be used instead of the traditional centered topology, as shown in Appendix D.1. The difference between the two is shown in Figure 3.21. The spacing between coupled lines was so small at 130 GHz with a 5 GHz bandwidth that the ability of Applied Thin Film to successfully manufacture the design was questioned, so the offset topology was used because it increases the spacing between coupled lines.

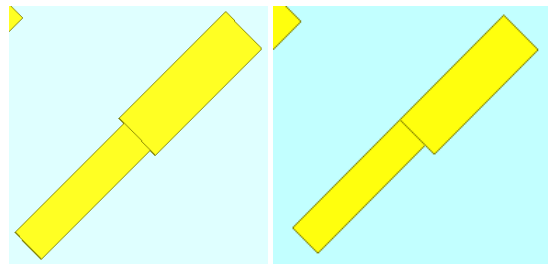


Figure 3.21: Centered coupled line topology (left) and offset coupled line topology (right).

Once the widths, lengths, and spacing values of the filter from Planar EM had been imported into HFSS, the design could be re-simulated. Upon simulating in this 3D environment, the frequency response of the filter was neither centered at 130 GHz nor had a 5 GHz bandwidth. Consequently, further optimization was needed. Fortunately, this process can be automated, unlike it was at 92 GHz, because of a better understanding of the available features and tools in

HFSS. A 3 mil thick alumina substrate was defined using HFSS's Djordjevic-Sarkar model input, as described in Section 3.6.1, with 0.1 mil thick gold microstrip lines. The cavity is 20 mils high and 37.2 mils wide. The other key parameter in the model setup is the size of the waveguide port in HFSS, which is 14.6 by 14.6 mils [23]. The waveguide port size has a major effect on the frequency response of the filter. The filter is then centered at 130 GHz and made to have a 5 GHz bandwidth by optimizing certain variables relating to insertion loss and input return loss. This optimization process is not an exact science and requires subtle changes in the insertion loss and input return loss criteria as well as which variables are optimized. Also, a key factor in the optimization process is to have a sufficiently capable computer to perform these tasks. One optimization pass took approximately 1 hour on an Intel Quad-Core i7 processor with 12 GB of RAM⁶, which was purchased to enable the filter optimization to be performed in a reasonable amount of time. This is especially important because dozens of optimization runs are necessary to obtain the desired filter response. Also, the optimization does not always change the filter in the expected way, so parameters need to be changed before the optimization is re-run.

3.6.4.2 Measurement

The narrow bandpass filter was designed to have an input return loss of better than 15 dB, as shown in Figure 3.23, and a bandwidth of 5 GHz, as shown in Figure 3.24. As shown in Figure 3.23, the open air measured input return loss is worse than simulated by at least 5 dB. The measurement of the insertion loss and its corresponding bandwidth compares favorably with

⁶ Intel Core i7-950 Bloomfield 3.06 GHz LGA 1366 130W Quad-Core Processor BX80601950, two sets of Corsair XMS3 6GB (3 x 2 GB) 240-pin DDR3 SDRAM DDR3 1333 (PC3 10666), ATI 100-505505 FireGL V7700 512 MB PCI Express 2.0 x16 workstation video card, Gigabyte GA-X58A-US3R LGA 1366 Intel X58 SATA 6Gb/s USB 3.0 ATX Intel Motherboard.

the simulated response, as shown in Figure 3.24. This is especially true once the losses of the CPW to microstrip transitions used for testing purposes are de-embedded, referred to as “measured corrected” in Figure 3.24.

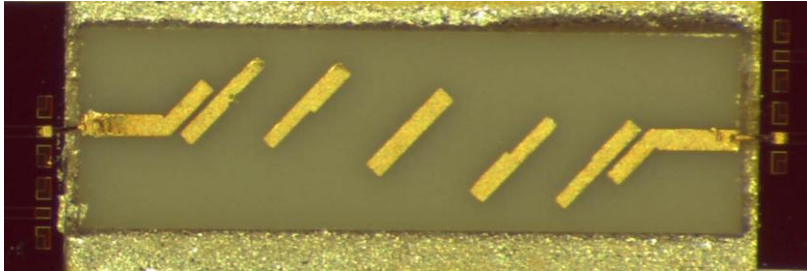


Figure 3.22: Measurement configuration of the 130 GHz narrow bandpass filter.

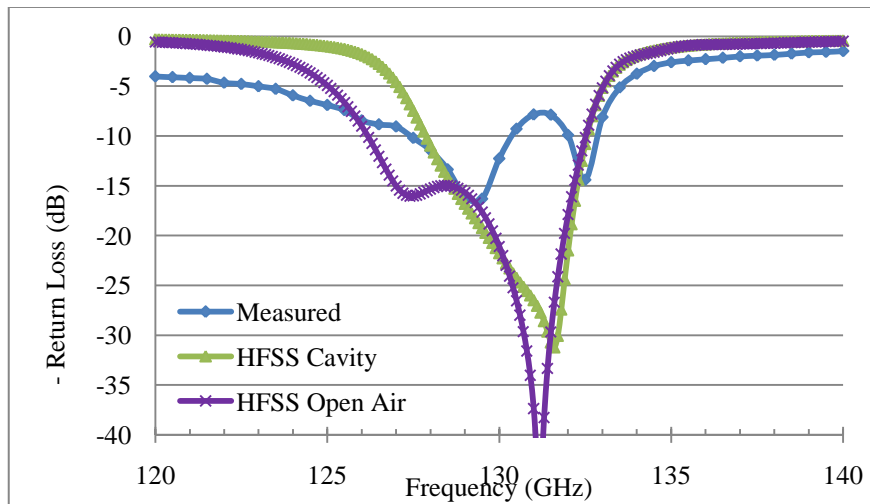


Figure 3.23: Input return loss comparison between HFSS simulations and measured results for the 130 GHz narrow bandpass filter.

The lack of sharp roll off in frequency when in open air is evident in Figure 3.24, similar to that of the 92 GHz bandpass filter. The zoomed in view in Figure 3.25 shows very good agreement between the HFSS open air simulation and the measured corrected open air insertion loss.

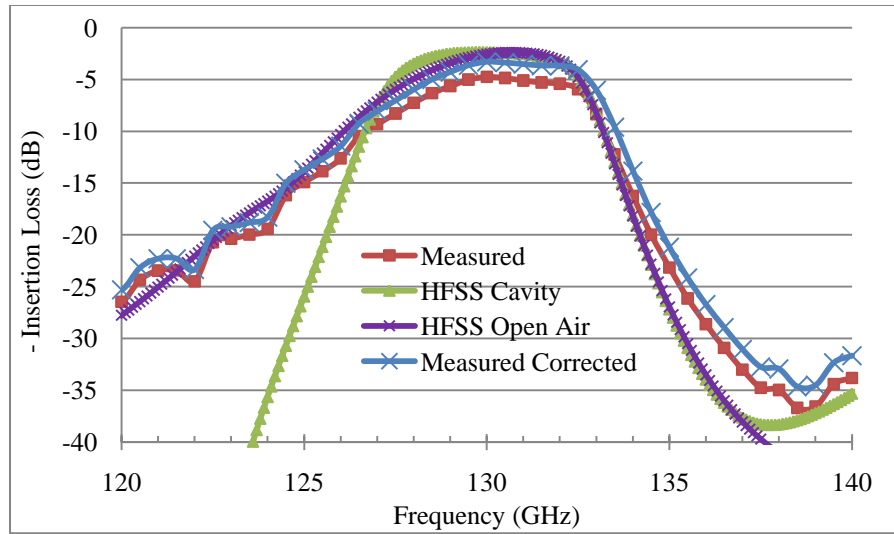


Figure 3.24: Insertion loss comparison between HFSS simulations and measured results for the 130 GHz narrow bandpass filter.

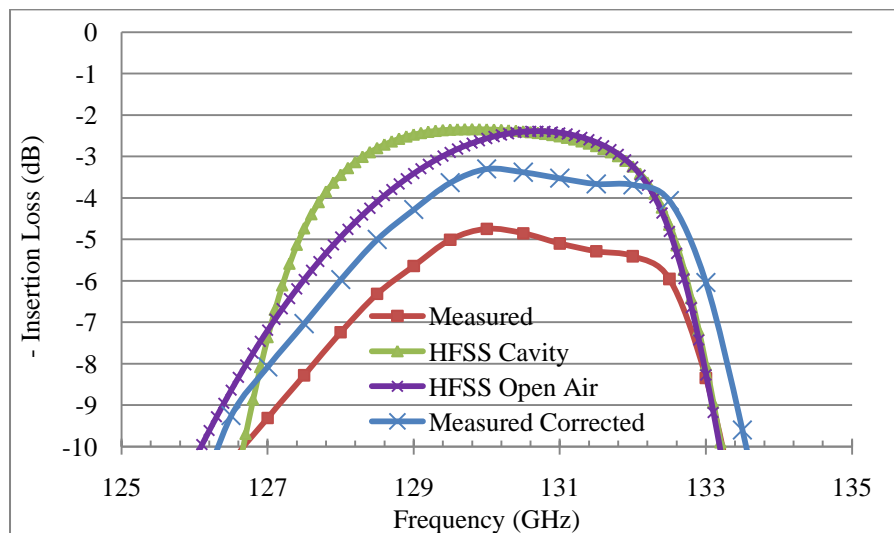


Figure 3.25: Zoomed in view of the insertion loss comparison between HFSS simulations and measured results for the 130 GHz narrow bandpass filter.

A measurement of the narrow bandpass filter was also performed with the addition of interconnect attenuators to determine the effect of tuning out the wire bond inductance. The measured input return loss results with and without interconnect attenuators are shown for the 130 GHz narrow bandpass filter in Figure 3.27. Unfortunately, the results are inconclusive in terms of whether or not the interconnect attenuators improved the matching of the filter. This

lack of improvement could be because the wire bonds used in assembly do not match those modeled in HFSS, the cavity has a significant effect on tuning out the wire bond inductance, or the interconnects do not work as designed.

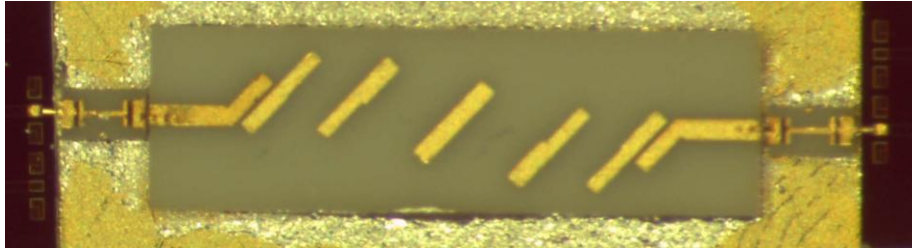


Figure 3.26: Measurement configuration of the 130 GHz narrow BPF with interconnect attenuators for improving matching and reducing gain.

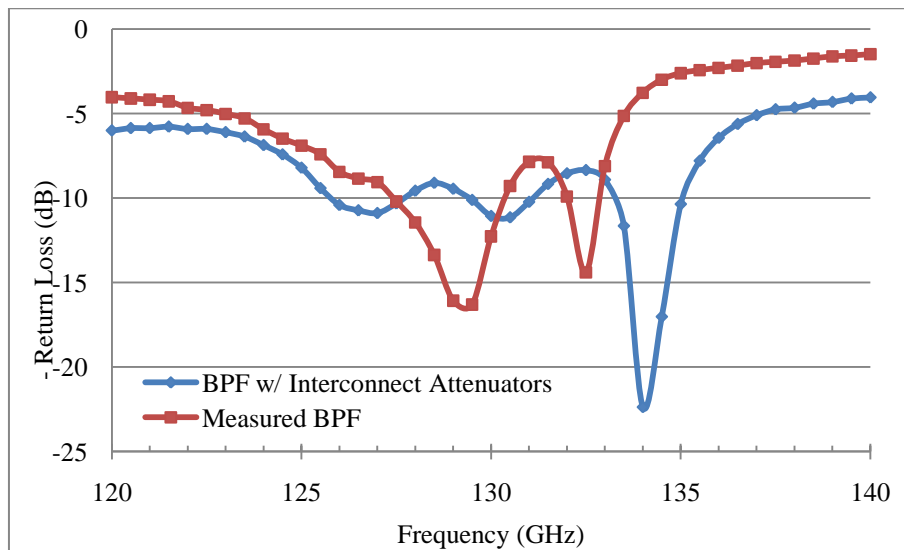


Figure 3.27: Input return loss comparison between measured 130 GHz narrow bandpass filter with and without interconnect attenuators.

3.6.5 Wide Edge-Coupled Bandpass Filter – Design and Measurement

The design of the 130 GHz wide bandpass filter follows the same procedure as for the narrow bandpass filter described in Section 3.6.4. This wider bandpass filter with a bandwidth of 10 GHz is necessary to reduce the out of band RF signal so that the LNAs will not become saturated due to out of band signals. To prevent this, a BPF will be placed in front of every two LNAs to ensure they do not become saturated.

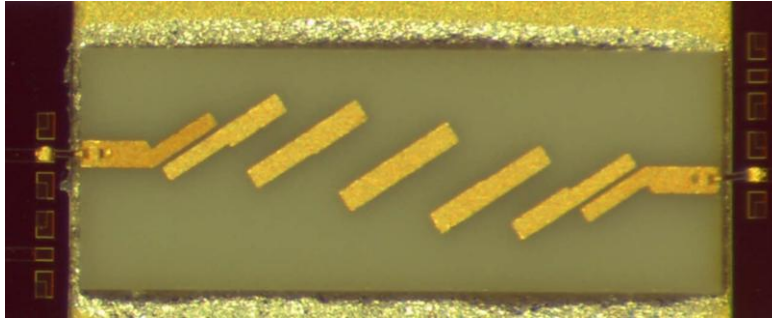


Figure 3.28: Measurement configuration of the 130 GHz wide bandpass filter.

Two narrow BPFs cannot be used because even though each filter has the same design parameters, i.e. length, width, and spacing, manufacturing tolerances may result in slight variations to these parameters. These variations could shift each narrow bandpass filter in the opposite direction in frequency and result in some of the RF signal being lost. In addition, the bandwidth of the system would be less than the expected bandwidth of the narrow BPF. Using a wider BPF prior to the narrow BPF will prevent this loss of signal from becoming an issue.

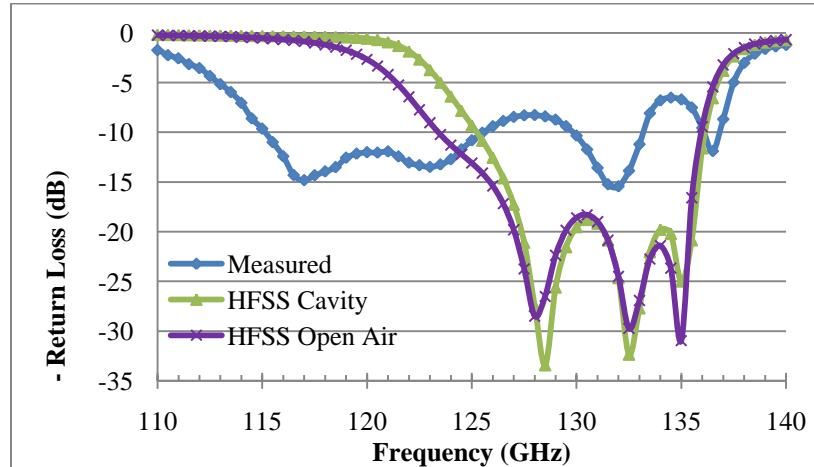


Figure 3.29: Input return loss comparison between HFSS simulations and measured results for the 130 GHz wide bandpass filter.

The input return loss for the HFSS simulations and measured results are shown in Figure 3.29. The matching is not as good as expected but is still acceptable for use in the radiometer. The bandwidth of the measured frequency response is also significantly larger than the design.

Comparison of the HFSS simulations to the measured results for the insertion loss show good agreement, as shown in Figure 3.30, especially when the losses due to the CPW to microstrip transitions are taken into account. The insertion loss at 130 GHz is greater for the measured open air response than for the simulated open air response by 1 dB. While the open air bandwidth of the wide bandpass filter is 13.5 GHz, the measured open air response is reasonably close at 16 GHz. The measured response shown in Figure 3.30 does not attenuate as sharply on its low frequency end as expected based upon simulation results. Since there is such good agreement between the simulated and measured responses of the 130 GHz narrow bandpass filter, manufacturing tolerances of the coupled lines are the probable cause of this discrepancy. The smallest differences between the widths of the coupled lines are approximately 0.21 mils for the narrow BPF and are only approximately 0.14 mils for the wide BPF. Even though the bandwidth of the wide bandpass filter is slightly larger than expected, it will accomplish the purpose of preventing LNA saturation.

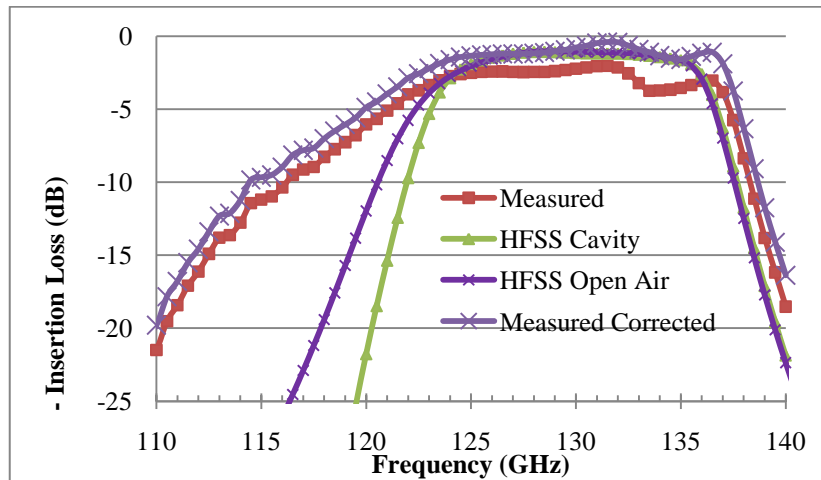


Figure 3.30: Insertion loss comparison between HFSS simulations and measured results for the 130 GHz wide bandpass filter.

The insertion loss at higher frequencies, especially near the 183 GHz strong water vapor absorption line, needs to be considered as well as the bandwidth of the bandpass filter centered at

130 GHz. This is only necessary if the bandwidth of the antenna includes 183 GHz, which is not the case for this radiometer because of waveguide cutoffs. While not necessary, this is a useful exercise so optimization was performed to ensure sufficient attenuation near 183 GHz. To ensure sufficient attenuation the insertion loss frequency response of the wide and narrow bandpass filters were offset. As shown in Figure 3.31, the wide BPF insertion loss response has a high level of attenuation near 183 GHz. This makes the attenuation level of the narrow BPF not as important at 183 GHz since the wide BPF already reduced the RF to negligible levels. The attenuation of the narrow bandpass filter is still a significant 30 dB at the strong water vapor absorption line. This would be acceptable by itself, but when used with the over 70 dB of attenuation from the wide bandpass filter, the response is excellent.

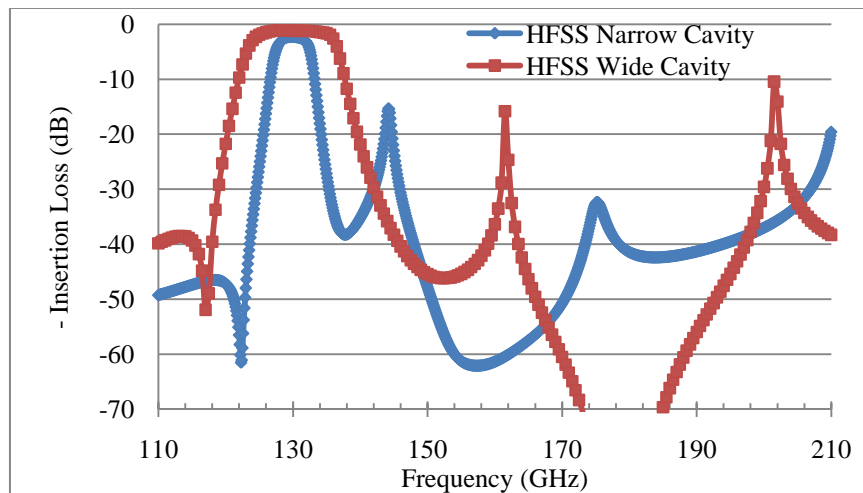


Figure 3.31: Insertion loss of wide and narrow bandpass filters at 130 GHz.

3.6.6 Attenuator – Design and Measurement

The 130 GHz attenuators are designed and fabricated on a 3 mil thick alumina substrate with 0.1 mil thick gold and TaN thin film resistors with a sq of 25 ohms/sq. The methodology used for their design is the same as the 92 GHz attenuators in Section 2.6.4.1.

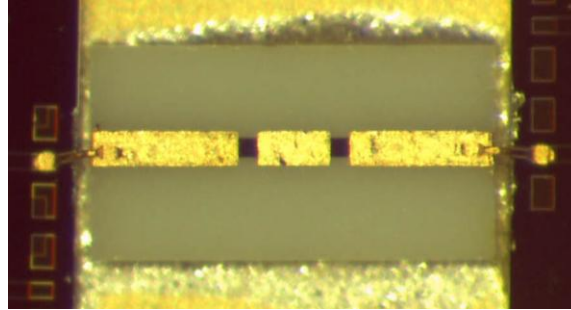


Figure 3.32: Measurement configuration of the 130 GHz attenuator.

The open air measurement used JPL’s F-band RF probe station along with the CPW to microstrip transitions shown in Figure 3.32. The input return loss results for the HFSS cavity simulation, HFSS open air simulation, and open air measurement are shown in Figure 3.33. The simulated input return loss is approximately 20 dB for both the cavity and open air models. The measured match is worse but is still better than 10 dB across the bandwidth of interest. This decreased input return loss stems in part from the CPW to microstrip transitions and wire bonds used in the testing of this component.

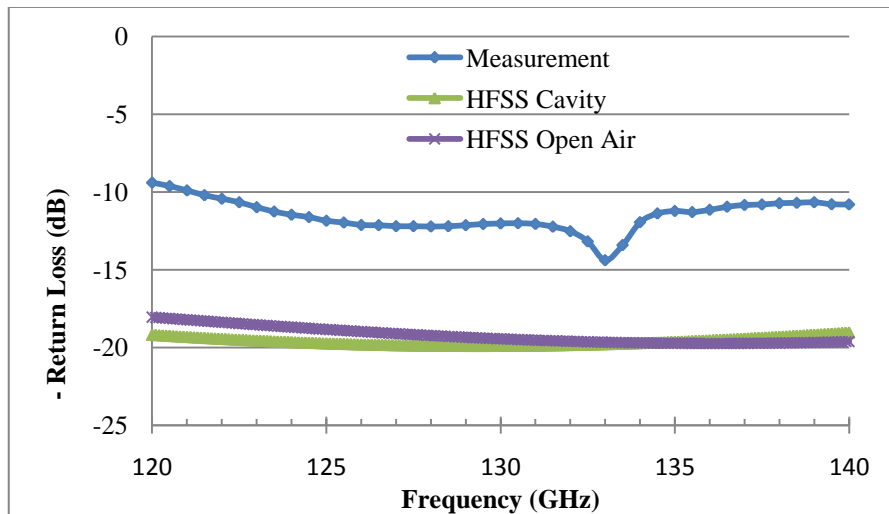


Figure 3.33: Input return loss comparison for the 130 GHz attenuator between the HFSS cavity simulation, HFSS open air simulation, and the measured component.

The insertion loss results for the simulations and measurements are shown in Figure 3.34. The simulated insertion loss is approximately 4.75 dB, which agrees fairly well with the

measured results. The measured results include the losses of the CPW to microstrip transitions which explains why the insertion loss is greater than simulated, while they were removed from the measured corrected curve. As discussed in Section 3.6.3, the de-embedding of CPW to microstrip transition losses has high potential for significant error. This error is the most likely reason for the slope of the measured results shown in Figure 3.34. The comparison of simulated and measured results for the 130 GHz attenuator indicates sufficient matching and an insertion loss close to the designed loss of 4.75 dB.

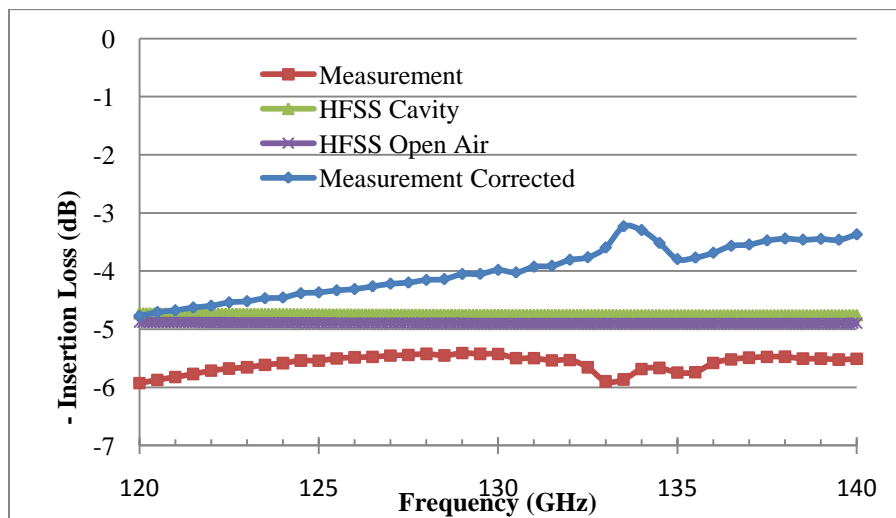


Figure 3.34: Insertion loss comparison for the 130 GHz attenuator among the HFSS cavity simulation, HFSS open air simulation, the measured component, and the measured corrected.

3.6.6.1 Multi-Chip Module Design and Assembly

The 130 GHz multi-chip module design is similar to the 92 GHz MCM discussed in Section 2.6.5. It was modeled in SolidWorks instead of AutoCAD. It is manufactured out of gold plated brass with a clamshell design. The bias printed circuit board, MMICs, and passive components are located in the bottom clamshell, with the top half completing their cavity. No fundamental changes were made to this MCM design from the 92 GHz version, but numerous improvements were implemented.

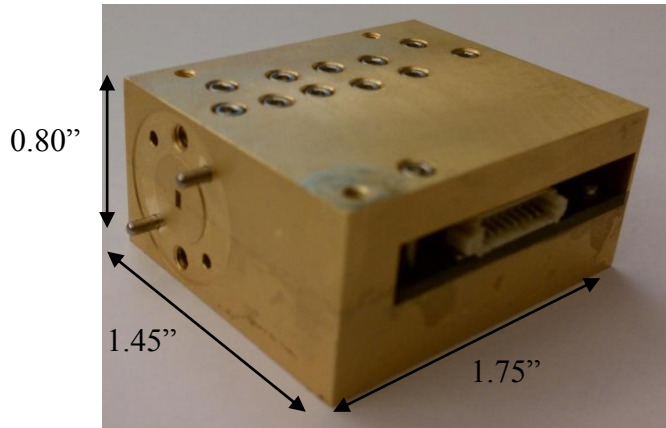


Figure 3.35: 130 GHz MCM clamshell.

The 130 GHz MCM has both input and output waveguides since the power detector is in waveguide packaging instead of a MMIC inside of the MCM. Figure 3.37 shows a CAD representation of the 130 GHz RF trench with components placed. This provides an excellent visualization for the assembly process.

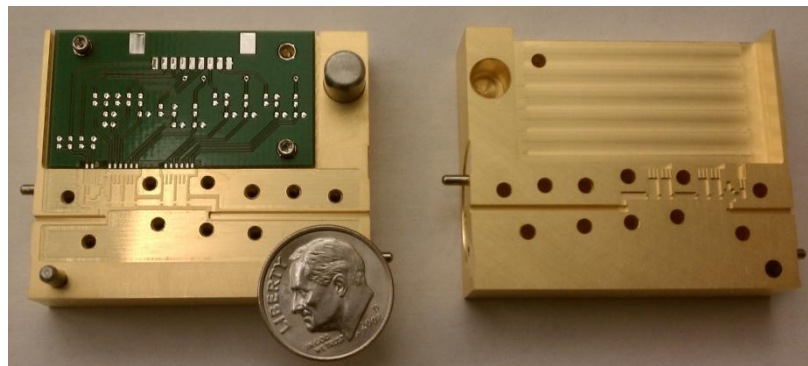


Figure 3.36: Unloaded view of the bottom (left) and top (right) halves of the 130 GHz clamshell with a dime for reference.

The placement of components in the MCM, as shown in Figure 3.37, follows from the radiometer block diagram shown in Figure 3.1 with the previously discussed passive and active MMIC-based components. Places for interconnects exist between all of the components except for those with built-in wire bond tuning, such as the waveguide-to-microstrip probe and the matched load.

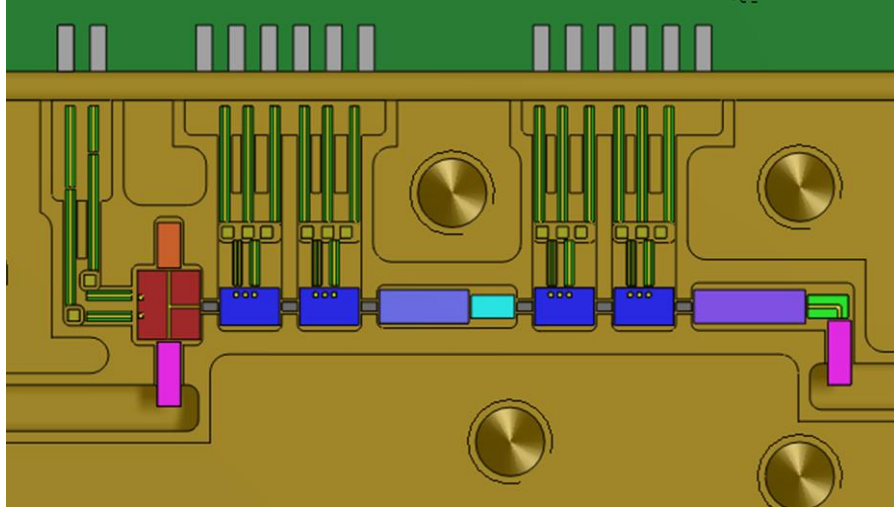


Figure 3.37: Zoomed in 3D CAD model of the 130 GHz MCM RF trench.

Figure 3.38 shows the assembled components in the CAD representation shown in Figure 3.37 and illustrates excellent assembly techniques. The assembly of the 130 GHz radiometer was completed by technicians at JPL. Flat ribbon wire bonds with 2 mil width were used between components wherever possible. 0.7 mil diameter wire bonds were used when making electrical connections to the switch or LNAs. The LNA bias transmission lines are circled in blue in Figure 3.38. The interesting difference between these lines and the 92 GHz MCM implementation is that they are placed in separate waveguide cavities with an unloaded cutoff frequency of 394 GHz. The 130 GHz evanescent mode will be attenuated by 110 dB along this path, which will prevent positive feedback of the RF signal along the bias transmission line path to the beginning of the RF chain.

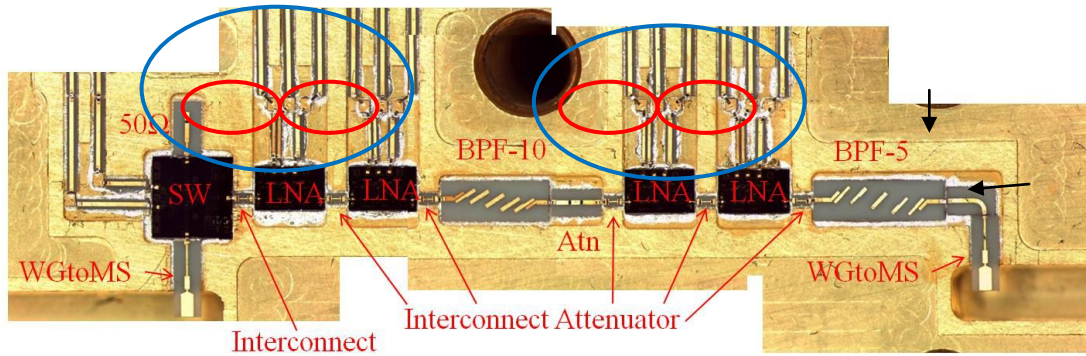


Figure 3.38: Assembled 130 GHz RF trench.

The capacitors used for filtering of the DC bias voltages circled in red in Figure 3.38 are 5x5x5 mils with a value of 51 pF from Dielectric Laboratories, Inc. Not only are these capacitors thinner than those used at 92 GHz, they are placed in a 2 mil depression so that they are the same height as the 3 mil thick alumina transmission lines for easier wire bonding. An example of the pressure ridges first described in Section 2.6.5 is shown with black arrows in Figure 3.38. The interconnect attenuators are located in a narrower waveguide cavity than the rest of the RF components. Even though its width is only 13 mils, its height is 20 mils, so the waveguide cutoff frequency for the interconnect cavity when unloaded is 295 GHz. This cutoff frequency combined with that of the bias transmission lines should be sufficient to prevent any positive RF feedback. The completely loaded RF trench for the 130 GHz MCM is shown in Figure 3.39. The bond pads on the bias PCB are electrically connected to the bias transmission lines by welding.

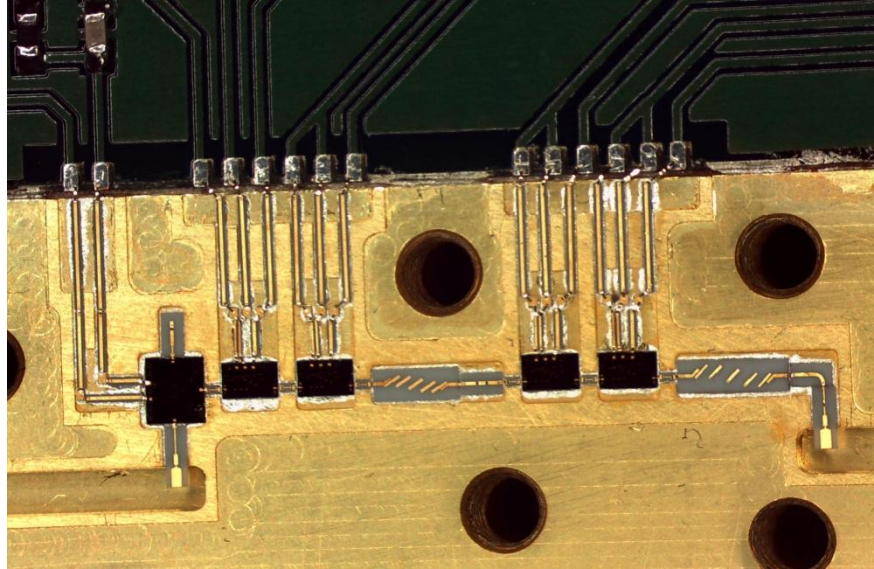


Figure 3.39: Zoomed view of the loaded RF trench in the bottom clamshell of the 130 GHz.

3.7 Testing

The switch and LNAs from JPL were integrated with the custom designed passive components into the 130 GHz radiometer with internal calibration. While all of the testing for the 92 GHz radiometer in Section 2.7 was performed for the 130 GHz radiometer, additional testing was also performed. Electromagnetic interference was noticed during the testing of the 130 GHz radiometer due to SPI communication. Consequently, the SPI baud rate was reduced so it did not couple noise onto the power detector output voltage.

3.7.1 Mass, Volume and Power Consumption

By producing a functioning MMIC-based microwave radiometer at the center frequency of 130 GHz with internal calibration, its size, mass, and power consumption can be characterized as baselines for future radiometer designs.

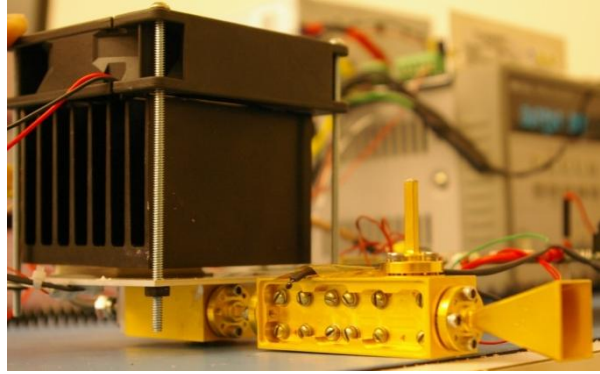


Figure 3.40: Photo of 130 GHz radiometer with a matched load on the coupled port and active thermal control.

The dimensions of the 130 GHz radiometer are shown in Figure 3.41. The radiometer does not include the thermal control or data acquisition system in its size of 7.78" L x 1.45 W x 2.53" H or volume of 28.54 in³. This radiometer test setup includes a 1" waveguide through line with the noise source. The MCM alone has dimensions of 1.75" L x 1.45 W x 0.08".

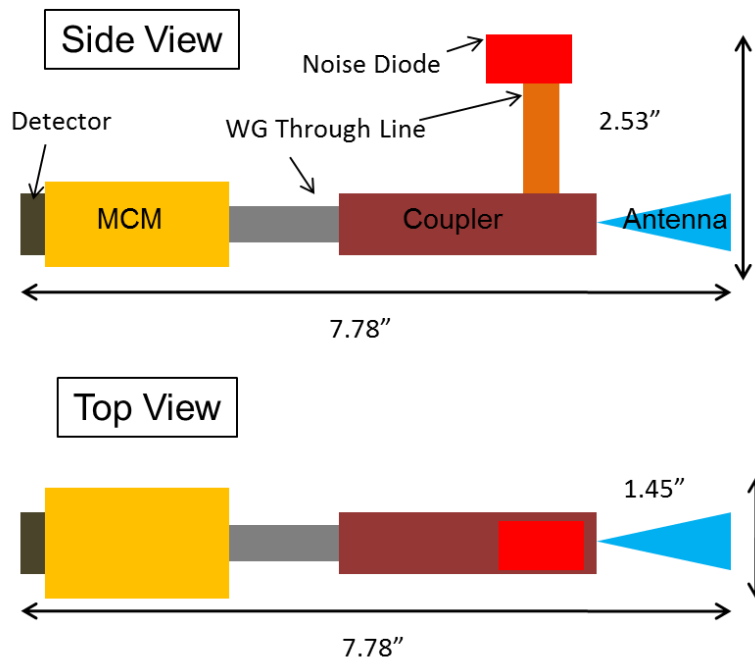


Figure 3.41: Diagram of 130 GHz radiometer dimensions.

The mass and power of the complete radiometer are included in Table 3.4 except for the passive thermal control. The mass of the MCM and waveguide components is less than 0.5 kg

and could be reduced further in a redesign of the system. The power consumed by the radiometer is 0.172 W, which is much less than the 3.368 W of the data acquisition and control board. The active thermal control would also contribute a substantial amount to the power budget if included.

Table 3.4: Power and mass analysis of the 130 GHz radiometer.

	Power (W)	Mass (g)
MCM and WG power detector	0.172	244.8
Waveguide components with a standard WR-08 horn antenna		227.8
Peltier, heat sink, and fan (no TCM)		494.0
Data Acquisition PCB	3.368	136.6
Microcontroller Board		196.9
Total	3.540	1300.5

3.7.2 Multi-Chip Module Bias Board

The bottom half of the 130 GHz clamshell is shown in Figure 3.42, which includes one bias board, as described in Appendix F.2. Only one bias board was necessary due to the bias layout of the switch and LNAs. This enabled the MCM to be smaller than the 92 GHz version.

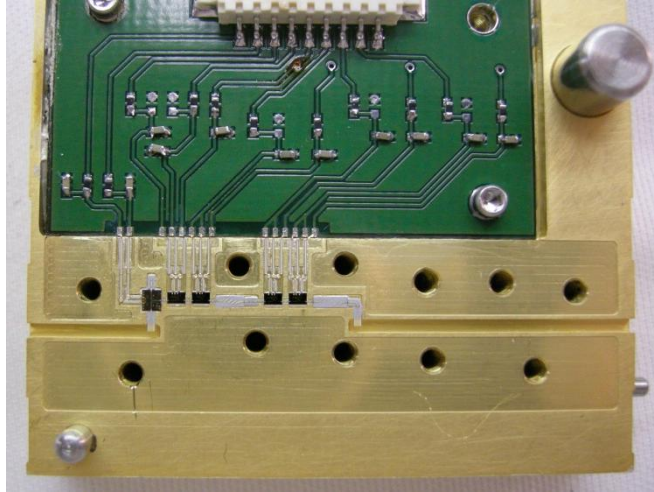


Figure 3.42: Loaded bottom clamshell of the 130 GHz MCM.

The bias board contains a PicoBlade connector, which is not recommended for future designs, as discussed in Section 2.7.2. Resistor divider options are placed for all gate biases, and capacitors are placed on all lines for filtering purposes, as shown in Appendix F.2. The gate biases were chosen by manually adjusting the voltage dividers for the gates until the drain current was 15-20 mA. This biasing was performed one LNA at a time in a serial fashion. Gate biases varied from 0.05 – 0.21 V with a drain voltage of 0.7 V. The one area of improvement for this 130 GHz MCM design would be to place the bias PCB on the reverse side of the RF trench and used feedthroughs to connect the biasing to the bias transmission lines. This would add robustness to the design by allowing resistors and capacitors to be changed on the PCB without the risk of damaging the MMIC components in the RF trench by accidentally breaking a wire bond or splattering solder and flux on them.

3.7.3 Thermal Control

The thermal control setup and implementation for the 130 GHz radiometer is nearly identical to the 92 GHz radiometer in Section 2.7.4. The active thermal control was

implemented using a Peltier unit with the TC-36-25 RS232 from TE Technologies, Inc. The PID control settings are provided in Appendix F.3. The thermistor from TE Technologies was used for the temperature feedback to the thermal control unit. The thermistors from Omega, Inc. were used to monitor the temperature of the MCM, data acquisition board, coupler, and an ambient microwave absorber. This thermal control setup involved using a Peltier unit sandwiched between a small metal plate directly attached to the 130 GHz MCM and a larger heat sink with a fan. This created a more stable thermal control system than that of the 92 GHz radiometer due to the better contact between the MCM, Peltier unit, heat sink, and fan. The thermal setup described is shown in Figure 3.43.

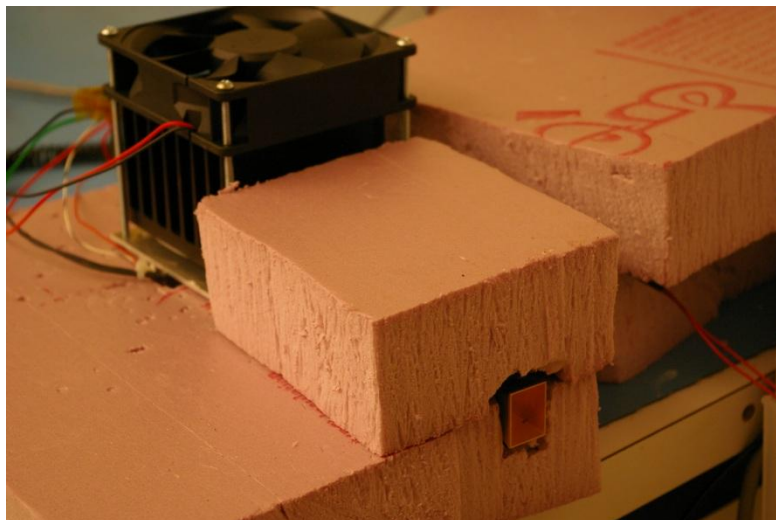


Figure 3.43: Thermal setup of the 130 GHz radiometer with insulating foam and Peltier control system.

The temperature data from overnight testing of the 130 GHz MCM shows approximately ± 0.05 K of temperature variability over 16 hours of testing, as shown in Figure 3.44. This level of control is better than the required ± 0.1 K, and the testing was conducted in a controlled laboratory environment with the system at temperature equilibrium.

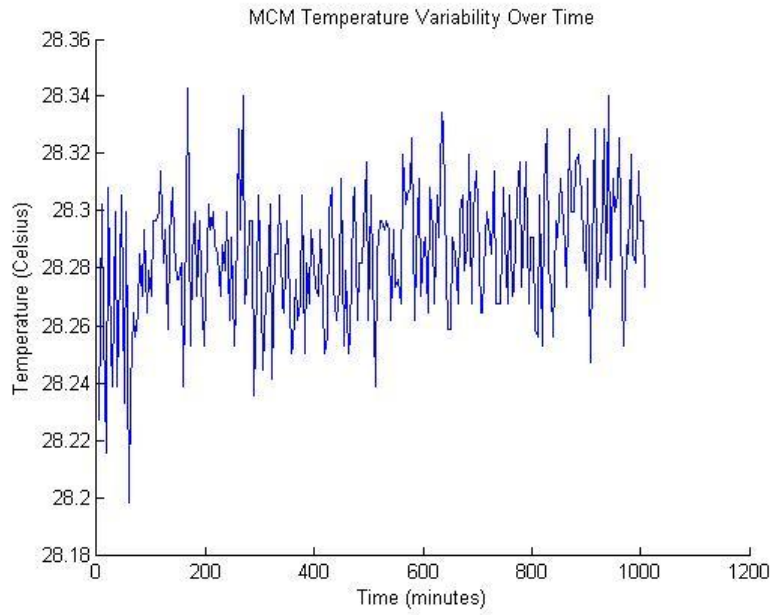


Figure 3.44: MCM temperature data of 130 GHz MCM.⁷

⁷ Antenna data of the room temperature microwave absorber from November 1 and 2, 2011.

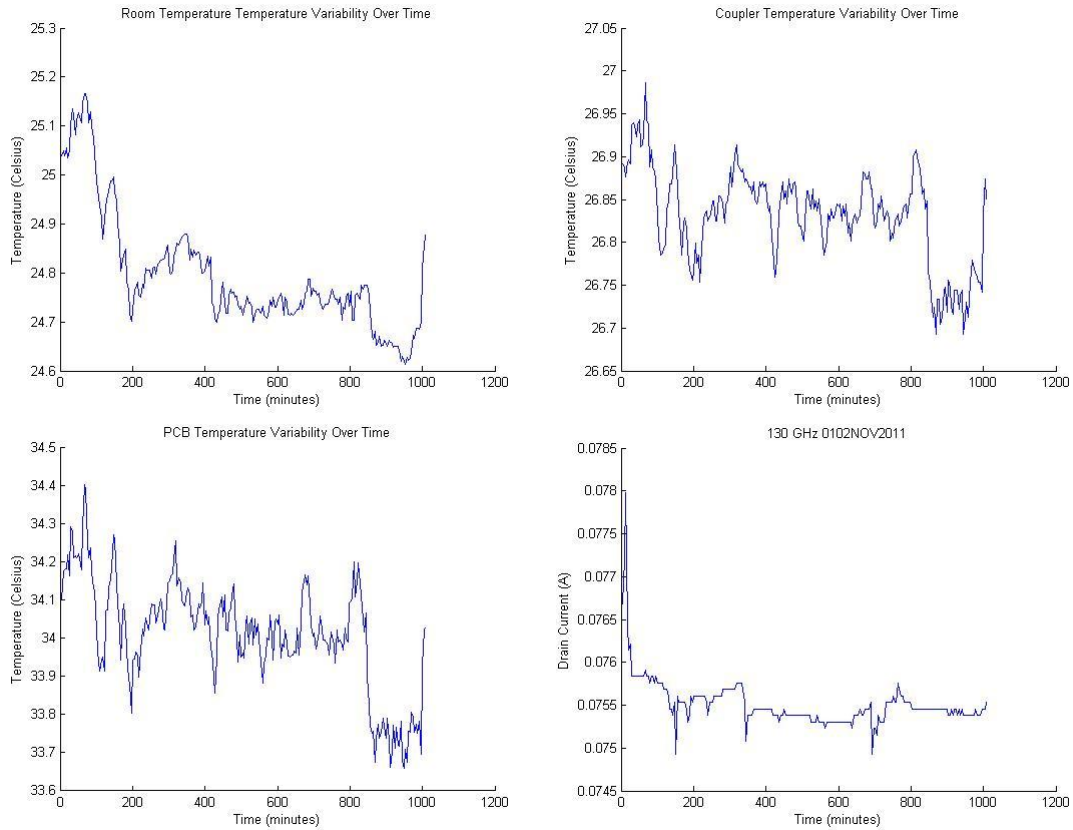


Figure 3.45: Temperature and drain current data for 16 hours of looking at room temperature microwave absorber.⁷

Temperature data measured at the directional coupler and on the PCB exhibit higher variability than that of the active thermally controlled MCM, as shown in Figure 3.45. This is to be expected due to the lack of active thermal control. Comparing this temperature data with the warm microwave absorber temperature data shows a strong correlation between them. The drain current is extremely stable and only varies by a few milliamperes over the course of 16 hours once initial equilibrium is obtained. This consistency partially stems from the active thermal control implemented on the 130 GHz MCM, which is better than that of the 92 GHz radiometer.

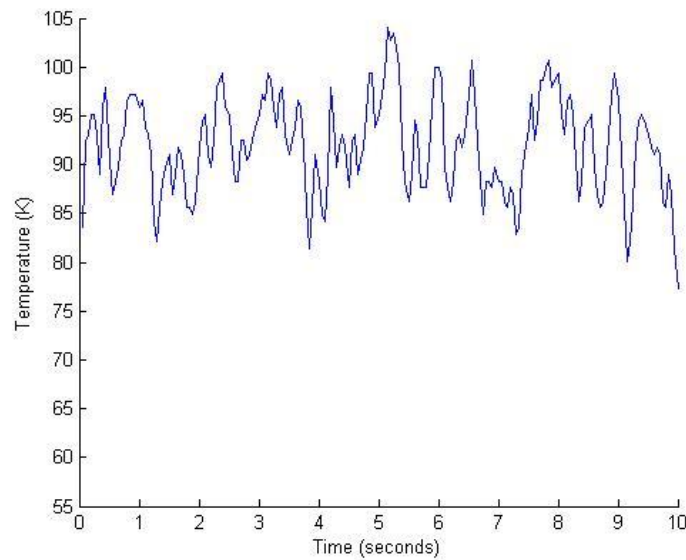


Figure 3.46: Cold microwave absorber data.⁸

The brightness temperature data of the cold microwave absorber is shown in Figure 3.46. The brightness temperature data of the warm microwave absorber is shown in Figure 3.47. The physical temperature of the cold absorber was 77.6 K and of the warm absorber was approximately 297 K. The brightness temperature data were externally calibrated. The significant temperature measurement variability improvements due to averaging and Dicke switching will be discussed in detail for Allan deviation measurements in Section 3.7.5.1.

⁸ Run 1 of Y-factor experiment 10 data on October 27, 2011 with $m = 0.0002223$ V/K and $b = -0.33325$.

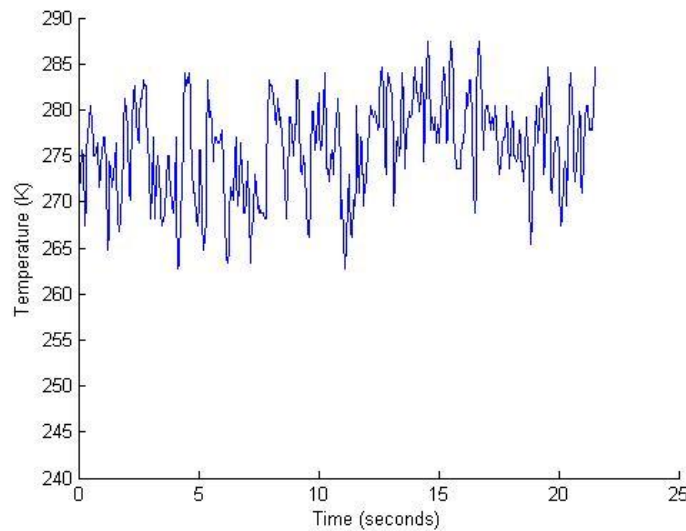


Figure 3.47: Room temperature microwave absorber temperatures.⁸

3.7.4 Results

The testing of the 130 GHz radiometer was conducted using passive and active thermal control. Measurements were acquired only after the system reached thermal equilibrium at a sampling rate of 20 Hz with a video gain of 4242. A shielded SMA cable was used to connect the power detector output to the video gain input on the data acquisition and control board. While this provides another potential ground loop, the shielding significantly reduced the noise associated with the measurements. Since the RF gain is less than expected, as discussed in Section 3.3, the radiometer is highly sensitive to test setup conditions.

3.7.4.1 Measured Receiver Noise Temperature

The receiver noise temperature of the 130 GHz radiometer was measured using the Y-factor method discussed in Section 2.7.5.1. The Y-factor test was performed at specified intervals with 20 s each of warm microwave absorber data followed by cold microwave absorber

data with results shown in Table 3.5. The cold data were truncated to 200 samples or 10 s of data due to warming of the microwave absorber.

Table 3.5: Receiver noise temperature measurements for the 130 GHz radiometer using the Y-factor method.⁹

			Y-factor	Noise Temperature (K)
Time (min)	Room (K)	LN2 (K)		
Test 1				
0	297.35	77.6	1.135873	1540
0	297.35	77.6	1.155388	1337
15	297.15	77.6	1.147005	1416
15	297.15	77.6	1.166362	1242
30	296.85	77.6	1.201972	1008
30	296.85	77.6	1.137192	1521
45	296.85	77.6	1.138558	1505
45	296.85	77.6	1.13765	1515
60	296.75	77.6	1.171852	1198
60	296.75	77.6	1.150423	1379
Test 2				
0	296.85	77.6	1.166042	1243
0	296.85	77.6	1.18339	1118
15	296.75	77.6	1.165678	1245
15	296.75	77.6	1.148497	1398
30	296.75	77.6	1.169818	1213
30	296.75	77.6	1.166793	1236

The measured receiver noise temperature of the 130 GHz radiometer is 1320 K with a standard deviation of 152 K, as shown in Table 3.6. This noise temperature of 1320 K is close to the predicted noise temperature of 1328 K discussed in Section 3.2. The 130 GHz radiometer has a standard deviation which is a factor of 25 larger than that of the 92 GHz radiometer. This is a direct consequence of less than expected pre-detection gain and makes receiver noise temperature measurements difficult to perform consistently.

⁹ Receiver noise temperature measurements using the Y-factor method on October 27, 2011.

Table 3.6: Receiver noise temperature summary for the 130 GHz radiometer.9

	Average Noise Temperature (K)	Standard Deviation (K)
Test 1	1366	165
Test 2	1242	82
Average	1320	152

The radiometric resolution in Figure 3.48 for the 130 GHz radiometer in a Dicke configuration with internal calibration is comparable to that of the 157 GHz channel of MHS and the 89 GHz channel of AMSU. An antenna temperature of 100 K, a receiver noise temperature of 1320 K, a 5.25 GHz bandwidth and a $\Delta G/G$ of 1.34×10^{-3} are used to calculate the radiometric resolution. The Dicke $NE\Delta T$ also uses a T_{REF} of 301 K. The $\Delta G/G$ was determined from (1.8) using the measured receiver noise of 1320 K and the measured Allan deviation minimum in total power mode of 1.9 K at 4 s, as shown in Section 3.7.5.1.

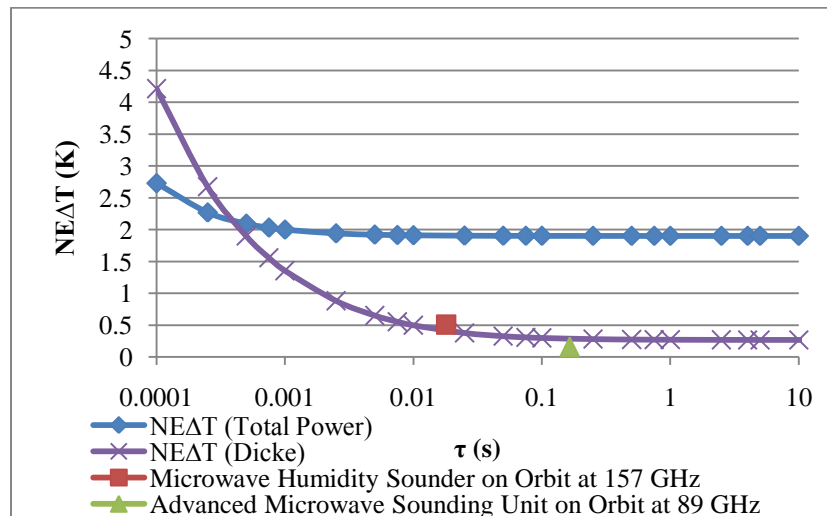


Figure 3.48: 130 GHz radiometric resolution in total power mode based on the measured receiver noise temperature of 1320 K and a 5.25 GHz bandwidth.

3.7.4.2 Internal Calibration

The 130 GHz radiometer's internal calibration testing consisted of performing an external calibration followed by measuring the coupled noise diode power. The noise diode was measured at JPL to have an average ENR of 4 dB over the bandwidth of 128-132 GHz with a detector bias of 30 mA at -9.0 V. The calculated noise diode temperature is listed in Table 3.7. Both the external calibration and noise diode measurements for one test were performed within a time period of 30 seconds. This short measurement duration helps to reduce the effects of radiometer variability due to temperature, less than expected pre-detection gain, and noise diode power variability as a function of frequency.

Table 3.7: 130 GHz calculated noise diode temperature.¹⁰

Description	Time (min)	Noise Diode Temperature (K)
External/Internal	0	423.2
External/Internal	5	411.9
External/Internal	10	424.7
External/Internal	15	391.1
External/Internal	20	408.7
External/Internal	25	449.4
External/Internal	30	410.5

The results of the noise diode temperature measurements are shown in Figure 3.49. The stability of the noise diode temperature measurements could be improved considerably by increasing the RF gain of the receiver as well as performing the internal calibration testing of the radiometer in Dicke mode instead of total power mode, which will be discussed in Section 4.4.

¹⁰ Data acquired on December 15, 2011.

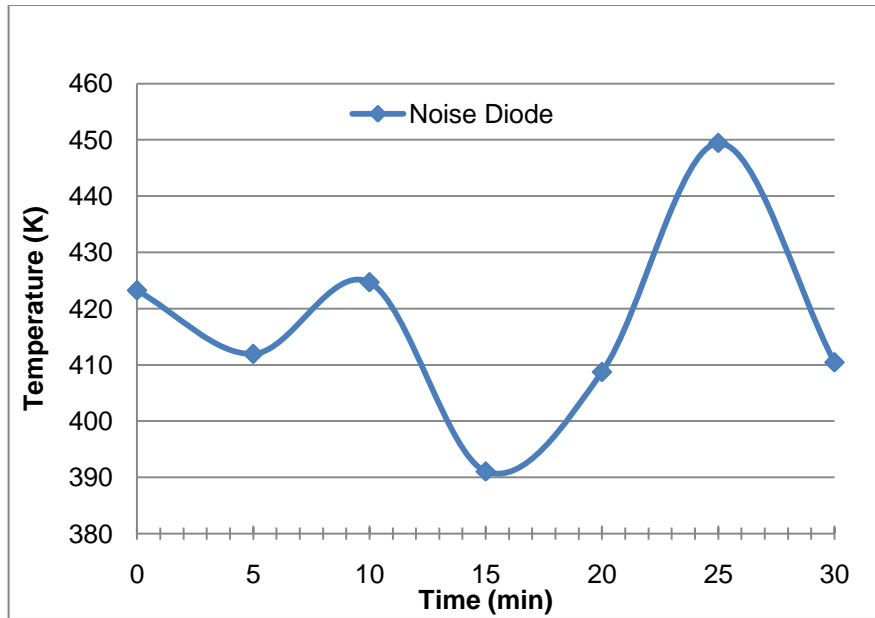


Figure 3.49: 130 GHz noise diode temperature.¹⁰

3.7.5 Long Term Radiometer Stability

Long term measurement data was taken for the 130 GHz radiometer in all three of its possible configurations: total power mode viewing the room temperature microwave absorber, total power mode looking at the internal matched load, and Dicke switching mode. The Allan deviation calculations were conducted for stable data from each of these operational modes and are discussed in Section 3.7.5.1.

3.7.5.1 Allan Deviation

The Allan deviation measurement approach is the same as that in Section 2.7.6.1 for the 92 GHz radiometer. The only difference is that different τ values were used due to the lower sampling rate. The τ values used were 0.25, 0.5, 1, 2, 4, 8, 16, 32, 64, 128, 256, 512, and 1024 s. The matched load equivalent noise temperature using previous calibration coefficients is shown in Figure 3.50. Its Allan deviation is shown in Figure 3.51 with a minimum at 1.9 K at an

integration time of 4 s. The warm microwave absorber brightness temperatures using previous calibration coefficients is shown in Figure 3.52. Its Allan deviation is shown in Figure 3.53 with a minimum at 1.9 K with an integration time of 4 s.

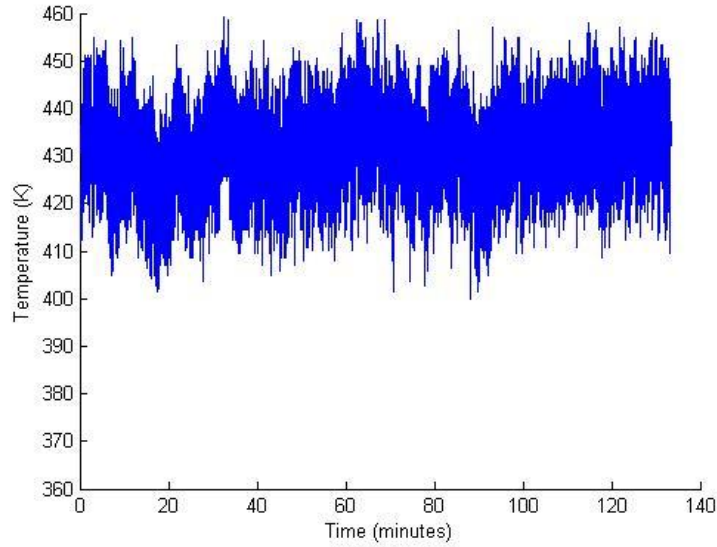


Figure 3.50: Matched load equivalent noise temperatures using previous calibration coefficients for the 130 GHz radiometer.¹¹

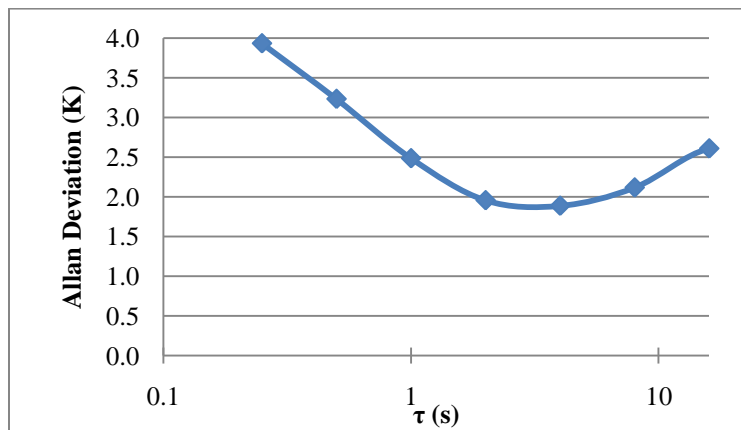


Figure 3.51: Allan deviation of 130 GHz radiometer while viewing the matched load.¹¹

¹¹ Second set of matched load data, samples (2×10^4 to 18×10^4) with -0.0129 offset, from October 27 and 28, 2011 with $m = 0.000208$ V/K and $b = -0.33218$.

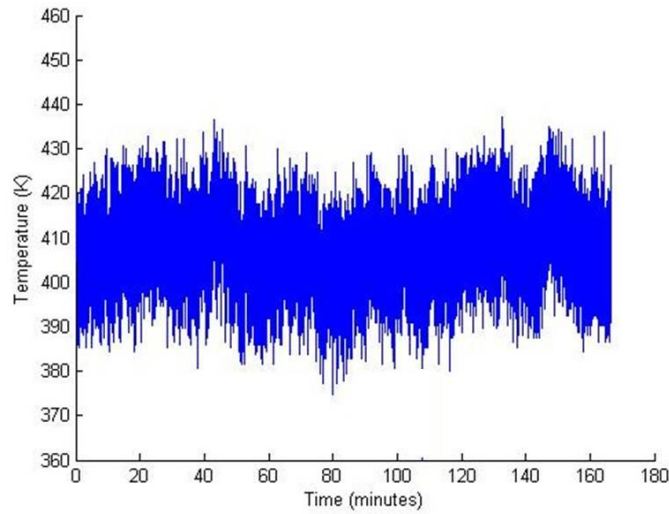


Figure 3.52: Warm microwave absorber brightness temperatures using previous calibration coefficients for the 130 GHz radiometer.¹²

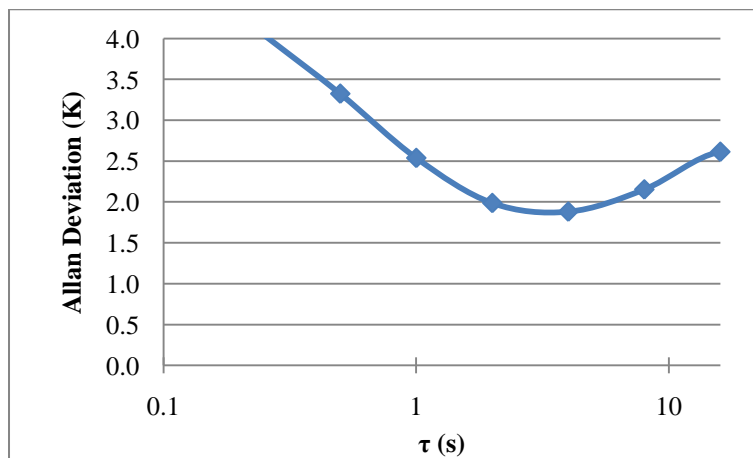


Figure 3.53: Allan deviation of the 130 GHz radiometer while viewing a warm microwave absorber.¹²

Measurements for Allan deviation were also carried out on the 130 GHz radiometer while it operated in Dicke mode. Considerable improvement in the minimum temperature is expected as a result of eliminating gain fluctuations and averaging samples. The sampling rate is still 20 Hz, but the Dicke switching occurs at a rate of 2 Hz. Due to response time of the low pass filter at the input of the difference amplifier, only the last five samples of every ten are averaged

¹² Antenna data, samples 2×10^5 to 4×10^5 , from October 27 and 28, 2011 with $m = 0.000208$ V/K and $b = -0.33218$.

and used in this analysis. The minimum Allan deviation from this analysis is 0.1 K with an Allan time of 1024 s. This result is considerably better than the $NE\Delta T$ of the 130 GHz radiometer with calculated gain variations while in total power mode.

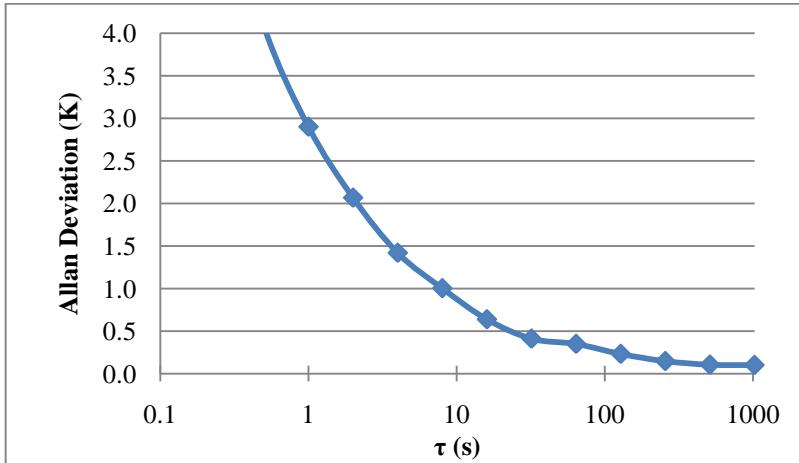


Figure 3.54: Allan deviation of the 130 GHz radiometer in Dicke mode.¹³

¹³ Dicke mode data, matched load and antenna samples 6 through 10 averaged and combined (2.2×10^4 to 4×10^4), from November 1 and 2, 2011.

Chapter 4

Summary and Future Work

4.1 Ocean Altimetry and Wet-tropospheric Path Delay

Satellite surface altimetry provides critical information for climatologists, weather forecasters, marine biologists, oceanographers, and even policy makers. Characterization of ocean mesoscale and sub-mesoscale circulation at spatial resolutions of 10 km and larger is a key science objective of NASA's Surface Water and Ocean Topography (SWOT) mission, planned for launch in 2020. The second key science objective of the SWOT mission is monitoring the height of inland bodies of water with areas as small as 250 m² and the flow rate of rivers at least 100 m wide. In order to obtain sea surface heights with better than 3 cm precision, altimeter measurements must account for wet-tropospheric path delay. Nadir viewing measurements using microwave radiometers on satellite altimeter missions are used to retrieve wet-tropospheric path delay. Microwave radiometers at 18-37 GHz currently enable wet-tropospheric path delay retrieval errors of less than 1 cm at distances 50 km or greater from the coasts. For the same antenna size, higher frequency (90-170 GHz), MMIC-based direct detection radiometers with internal calibration have been proposed to reduce the retrieved wet-tropospheric path delay error to better than 1 cm up to 3 km from the coasts. This thesis documented the design, fabrication, and testing of laboratory demonstration radiometers at 92 and 130 GHz, as well as associated component technology development, as part of a collaborative effort between the Microwave

Systems Laboratory at Colorado State University (CSU) and the Jet Propulsion Laboratory (JPL).

4.2 **92 GHz Radiometer**

A 92 GHz direct detection radiometer based on MMIC and microstrip components with low mass and low power consumption was integrated and tested at the Microwave Systems Laboratory (MSL) of CSU. This radiometer is internally calibrated using a coupled noise source and a switched matched load. Passive microstrip components and active MMIC-based components were designed and tested by MSL and JPL, respectively. The measured receiver noise temperature is 1271 K, which meets the design requirement of 1300 K. Its radiometric resolution ($NE\Delta T$) compares favorably with radiometers currently on orbit, such as the Advanced Microwave Sounding Unit (AMSU) and the Microwave Humidity Sounder (MHS) at 89 GHz. Neither of these two on-orbit radiometers are internally calibrated. The long term stability of the radiometer was demonstrated with an Allan deviation of 0.22 K and an Allan time of 8 s. This corresponds to radiometer gain variations ($\Delta G/G$) of 1.6×10^{-4} in total power mode. The size, power consumption, and performance of this radiometer provide a useful baseline for development of future ground-based, airborne and space-borne radiometers with internal calibration.

4.3 **130 GHz Radiometer**

A 130 GHz direct detection radiometer based on MMIC and microstrip components with low mass and low power consumption was developed and tested at MSL. Similar to the 92 GHz radiometer, the 130 GHz radiometer is internally calibrated using a coupled noise source and a switched matched load. MMIC-based active components and microstrip-based components were

developed at JPL and MSL, respectively. The measured receiver noise temperature of the 130 GHz radiometer is 1320 K, very close to the design requirement of 1300 K. Its radiometric resolution ($NE\Delta T$) compares favorably with the on-orbit AMSU and MHS at 89 and 157 GHz, respectively. Neither of these on orbit radiometers are internally calibrated. The minimum Allan deviation was determined to be 1.9 K with an Allan time of 4 s in total power mode and 0.1 K with an Allan time of 1024 s in Dicke mode. The gain variations ($\Delta G/G$) as a total power radiometer were calculated to be 1.34×10^{-3} . The size, power consumption, and performance of the 130 GHz radiometer will be used as a basis for the development of future ground-based, airborne and space-borne millimeter-wave direct detection radiometers with internal calibration.

4.4 Future Work

The noise temperature, radiometric resolution, and long term stability of the 92 and 130 GHz demonstration radiometers were found to compare favorably with on-orbit radiometers at lower frequencies without internal calibration. Suggestions for improvements in these and future radiometers are provided in this section.

- The 92 GHz receiver noise temperature and corresponding $NE\Delta T$ can be reduced by using the PIN-diode switch designed by JPL instead of the commercially available M/A-Com switch. This change will improve the switch insertion loss from 3.6 dB to 1.9 dB and would only require only minor changes to the MCM design to accommodate the JPL switch.
- The 92 GHz radiometer's MCM housing could be reduced in size, and feedback paths could be eliminated through the addition of high pass waveguide filters for the LNA bias trenches. The 92 and 130 GHz radiometers can be made more robust by using feedthroughs to apply bias voltages from the MCM bias boards to the MMIC

components. This arrangement would enable voltage dividers and other components to be modified without the risk of damaging the MMIC-based components in the RF trench. In addition, LNA gate voltage dividers and diode protection could be added to the MCM with a more robust connector.

- The 92 GHz bandpass filter could be optimized to eliminate the need for matching stubs and the corresponding low cavity lids. The filter's bandwidth can also be reduced to the desired 5 GHz. These redesigns would simplify the RF trench of the MCM and allow for more flexibility in filter placement.
- While the 92 GHz power detector from HRL is MMIC-based and can be placed directly in the RF trench to slightly reduce the overall radiometer's dimensions, the use of a waveguide detector would increase versatility and enable better radiometer characterization. A waveguide detector would allow a mixer to be attached to radiometer's output to characterize its response over frequency for both the 92 and 130 GHz radiometers. Commercially available waveguide detectors do not have the 15,000 V/W sensitivity of the W-band HRL detector, which helps to mitigate the effects of electromagnetic interference on the post-detection voltage signal. Consequently, a better option would be to package the HRL detector in a waveguide package with the transient voltage protection circuitry integrated into the packaging.
- The internal calibration testing of both the 92 and 130 GHz radiometers should be performed in Dicke mode. This requires hardware changes to the data acquisition and control board as well as simple software additions in order to bias and control the noise diode. Testing in Dicke mode will especially improve the stability of the noise diode measurements for the 130 GHz radiometer.

- Additional minor changes to the data acquisition and control board would reduce the amount of data discarded due to the low pass filter frequency response. The switch, lowpass filter, and difference amplifier used for averaging and Dicke subtraction would be removed. Subtraction would then be performed in data post processing.
- The radiometers and associated data acquisition system can be installed in robust packaging with active thermal control to increase their robustness for ground-based measurements.

Millimeter-wave radiometers at 92 and 130 GHz with internal calibration have been demonstrated in the laboratory to raise the technology readiness level in order to reduce the risk of and enable future satellite altimeter missions for wet-tropospheric path delay correction in coastal zones and over land water bodies.

Bibliography

- [1] Ernesto Rodriguez. (2009, March) SWOT: Mission. [Online].
http://swot.jpl.nasa.gov/files/SWOT_science_reqs_final.pdf
- [2] Jet Propulsion Laboratory. (2011, November) SWOT: Mission. [Online].
<http://swot.jpl.nasa.gov/science/technology/>
- [3] European Space Agency and Centre National d'Etudes Spatiales. (2011, November) Radar Altimetry Tutorial. [Online].
http://earth.eo.esa.int/brat/html/alti/welcome_en.html
- [4] J. Tournadre, J. Lambin-Artru, and N. Steunou, "Cloud and Rain Effects on AltiKa/SARAL Ka-Band Radar Altimeter—Part I: Modeling and Mean Annual Data Availability," *IEEE Trans. Geosci. Remote Sens.*, vol. 47, no. 6, pp. 1806-1817, March 2009.
- [5] M. Bevis, S. Businger, A. Herring, C. Rocken, R. Anthes, and R. Ware, "GPS Meteorology: Remote Sensing of Atmospheric Water Vapor Using the Global Positioning System," *J. Geophys. Res.*, vol. 97, no. D14, pp. 15,787-15,801, October 1992.
- [6] F. T. Ulaby, R. K. Moore, and A. K. Fung, *Microwave Remote Sensing: Active and Passive*. Reading, MA: Addison-Wesley Pub. Co., 1981, vol. 1.
- [7] M. A. Janssen, *Atmospheric Remote Sensing by Microwave Radiometry*. New York,

NY: John Wiley & Sons, Inc., 1993.

- [8] S. C. Reising et al. (2011, June) Development of Low-Mass, Low-Power, High-Frequency Microwave Radiometers with Internal Calibration to Provide High-Resolution Wet-Tropospheric Path delay Measurements for the SWOT Mission. [Online].
http://esto.nasa.gov/conferences/estf2011/presentations/Reising_ESTF2011_UPDATED.pdf
- [9] P. O. Lucas de Peslouan, C. Majek, T. Taris, Y. Deval, D. Belot, and J. B. Begueret, "A new frequency synthesizers stabilization method based on a mixed Phase Locked Loop and Delay Locked Loop architecture," in *Circuits and Systems, 2011 IEEE International Symposium on*, 2011, pp. 482-485.
- [10] J. Randa et al., "Recommended Terminology for Microwave Radiometry," National Institute of Standards and Technology, Boulder, 1551, 2008.
- [11] S. T. Brown, S. Desai, and A. B. Tanner, "On the Long-Term Stability of Microwave Radiometers Using Noise Diodes for Calibration," *IEEE Trans. Geosci. Remote Sens.*, vol. 45, no. 7, pp. 1908-1920, July 2007.
- [12] D. M. Pozar, *Microwave Engineering*, 3rd ed. United States of America: John Wiley & Sons, Inc., 2005.
- [13] Agilent Technologies. (2010, May) Noise Figure Measurement Accuracy - The Y-Factor Method. pdf. [Online]. <http://cp.literature.agilent.com/litweb/pdf/5952-3706E.pdf>
- [14] P. Kangaslahti and S. Padmanabhan, , 2010, Personal Communication.

- [15] O. Montes, D. E. Dawson, P. Kangaslahti, and S. Reising, "High Frequency PIN-Diode Switches for Radiometer Applications," in *ESTF2011*, Pasadena, 2011.
[Online]. http://esto.nasa.gov/conferences/estf2011/papers/Montes_ESTF2011.pdf
- [16] P. MacDonald, , 2010, HRL Laboratories.
- [17] HRL Laboratories. (2010) LN5-100. pdf. [Online].
www.hrl.com/capabilities/mmics/products/pdf/LN5-100.pdf
- [18] F. Iturbide-Sanchez, "Design, fabrication, and deployment of a miniaturized spectrometer radiometer based on MMIC technology for tropospheric water vapor profiling," Univ. Mass-Amherst, Amherst, PhD Disertation Fall 2007.
- [19] HRL Laboratories. (2011) V1A. pdf. [Online].
<http://www.hrl.com/capabilities/mmics/products/pdf/V1A.pdf>
- [20] S. C. Reising et al., "Advanced Component Development to Enable Low-Mass, Low-Power High Frequency Microwave Radiometers for Coastal Wet-Tropospheric Correction on SWOT," in *ESTF2010*, Washington D.C., 2010. [Online].
http://esto.nasa.gov/conferences/estf2010/papers/Reising_Steven_ESTF2010.pdf
- [21] Y. Leong and S. Weinreb, "Full band waveguide-to-microstrip probe transitions," in *1999 IEEE MTT-S International Microwave Symposium Digest*, vol. 4, Anaheim, 1999, pp. 1435-1438.
- [22] Applied Thin Film, Inc. ATP. [Online]. www.thinfilm.com
- [23] Ansys, Inc. (2009, February) Ansys. [Online].
http://www1.ansys.com/customer/content/content/HFSS_User-Guide.pdf
- [24] TE Technologies, Inc. Thermoelectric coolers. [Online].

<http://www.tetech.com/Temperature-Controllers/TC-36-25-RS232.html>

- [25] D. W. Allan, "Statistics of atomic frequency standards," *Proceeding of the IEEE*, vol. 54, no. 2, pp. 221-230, Feb 1966.
- [26] K. Auge and H. H. Richardson. (2011, September) Denver Post. [Online].
http://www.denverpost.com/search/ci_18827753
- [27] P. Kangaslahti et al. (2010, June) Radiometer Testbed Development for SWOT. ESTF 2010. [Online].
http://esto.nasa.gov/conferences/estf2010/presentations/Kangaslahti_SWOT_ESTF2010_B8P2.pdf
- [28] Techni-Tool. Techni-Tool. [Online]. www.techni-tool.com
- [29] Atmel Corporation. Atmel Corporation. [Online]. <http://www.atmel.com/>
- [30] Analog Devices. (1994, March) Analog Devices: Rarely Asked Questions. [Online].
http://www.analog.com/static/imported-files/rarely_asked_questions/moreInfo_raq_analogBreadboarding.html
- [31] H. Ott. Henry Ott Consultants. [Online]. <http://www.hottconsultants.com/>

Appendix A

MMIC Assembly

Proper MMIC assembly requires the use of specialized tools and assembly techniques. Fine tipped tweezers are essential to being able to place MMICs in the RF trench. This is due to less than a 5 mil gap existing on each side of the part when placed in the trench as well as some active MMICs being manufactured on 2 mil thick substrates. Both the curved and straight diamond-like carbon-coated fine tipped tweezers from Techni-Tool Inc. [28] work well for this type of work. Microspatula oilers from Techni-Tool Inc. are versatile and essential for MMIC assembly. Their ends are easily sharpened flat to aid in the application of silver epoxy and the lifting of wire bonds. A diamond scribe allows for substrates such as transmission lines to be cut to size. This eliminates the need for transmission lines of various lengths to be fabricated, thus reducing the cost and complexity of the MCM design. "Yellow tape" which has a removable adhesive can be applied to the oilers to more easily lift wire bonds and clean loose excess epoxy. Capillaries inserted into a wooden cotton swap can be used for detailed cleaning and lifting wire bonds. The wooden cotton swap can also be broken and sharpened to act as a larger version of the oiler spatulas. A digital scale is essential for mixing the proper 1:1 weight ratio of silver epoxy, parts A and B. Pre-mixed silver epoxy forms a harder and more stable bond than the self-mixed type but has special storage requirements involving temperature and humidity. Once the silver epoxy is mixed and applied, an oven is necessary to properly cure it. 15 minutes at 150°C is sufficient to cure the silver epoxy. The MSL has a West-Bond Inc. wedge wire bonder, model 7476E-79, which uses 1 mil diameter gold wire. This type and diameter of gold wire electrically connects passive and MMIC components, but several wire bonds are normally placed to reduce the inductance from the wire bonds. Inductance of wire bonds

proves to be especially problematic at frequencies higher than 100 GHz and will be taken into consideration during the design of those passive components. At 90-170 GHz it can be difficult to place two wire bonds due to the width of the gold transmission lines. Instead a wire bonder which uses flat 2 mil thick gold ribbon can be used i.e. flat gold wire. The flat gold ribbon provides a lower inductance electrical connection than the 1 mil diameter gold wire and a more robust connection. In order to perform most of this detailed MMIC assembly work, a microscope with an optical zoom of at least 20x should be utilized.

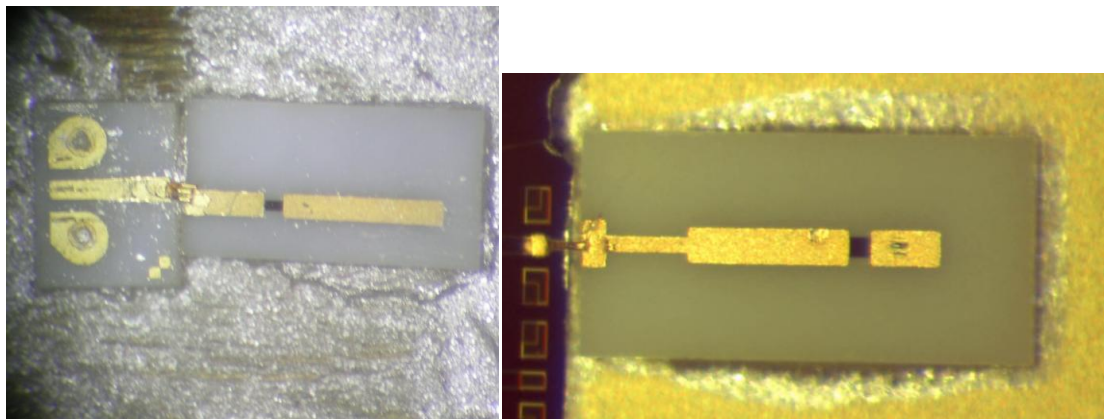


Figure A.1: Excess silver epoxy on 92 GHz matched load (*left*) and proper amount of silver epoxy on 130 GHz matched load (*right*).

Having the proper tools for high frequency MMIC assembly makes assembly possible, but significant practice is also necessary. Epoxying down passive and MMIC components on gold plated alumina substrates or pieces of brass enables a person to learn how much epoxy is necessary. The silver epoxy should be 1-2 mils thick and evenly distributed underneath the part using an oiler or wooden spatula. Once the part is placed on the silver epoxy, a wooden spatula can be used to push the part down by its corners to prevent damage. A small amount of epoxy should be around the edges of the part, but if too much epoxy was deposited then it may get on the MMIC and short it to ground. This

excess should be removed using an oiler spatula only after the silver epoxy has been cured in the oven. Isopropyl alcohol should be used sparingly when cleaning because it spreads the silver epoxy on top of the MMIC and weakens the bond created. Attempting to remove the silver epoxy before curing results in silver epoxy spreading all over the part, sometimes making it unusable. GSGs usually need to be epoxied down and wire bonded to the MMICs. The wire bonds should be short as possible and with some arc, especially if in the RF path where wire bond inductance may adversely affect the match between parts. The tails of the wire bonds should be cleaned or removed using an oiler spatula with “yellow tape” on it to prevent it from acting like an antenna. All of these techniques can be applied to assembling parts in the RF trench. Placing parts in the RF trench requires more precision as the spacing between parts is less than 2 mils and some of the parts are fabricated on 2 mil thick substrates which are easy to snap and flip into the silver epoxy. The waveguide-to-microstrip transition requires particular attention when installing in the MCM because the paddle of the transition needs to be placed perfectly into the waveguide for the best frequency response. Proper placement can be ensured by adding gold position lines on top of the waveguide-to-microstrip transition to line up with the edge of the waveguide and RF trench. Since the backside of the paddle of the probe lacks metallization, no silver epoxy can get on it or the probe performance will be adversely affected. A piece of a polished semiconductor wafer of GaAs can be used as a mirror and a bent capillary on a wooden stick can be used like a dentist’s cleaning tool to remove the excess silver epoxy on the underside of the probe. This cleaning process is difficult to perform and can only be performed by an expert MMIC assembly technician. MMIC assembly is a highly specialized and technical process at

these frequencies, which can be performed by graduate students with difficulty.

Inexperienced graduate students will destroy passive and MMIC components while trying to assemble them in the RF trench and waste considerable time during the process. A more cost effective alternative is to have an experienced technician perform the MMIC assembly. This will be a more efficient use of resources and time as well as resulting in a more reliable finished assembly. It is reasonable, however, to have a graduate student epoxy and wire bond individual passive and MMIC parts for testing on an RF probe station.

Appendix B

Backend Board I

The data acquisition and control system described previously was not the first version created. The first iteration of this PCB had several minor schematic issues and more significant layout issues. .

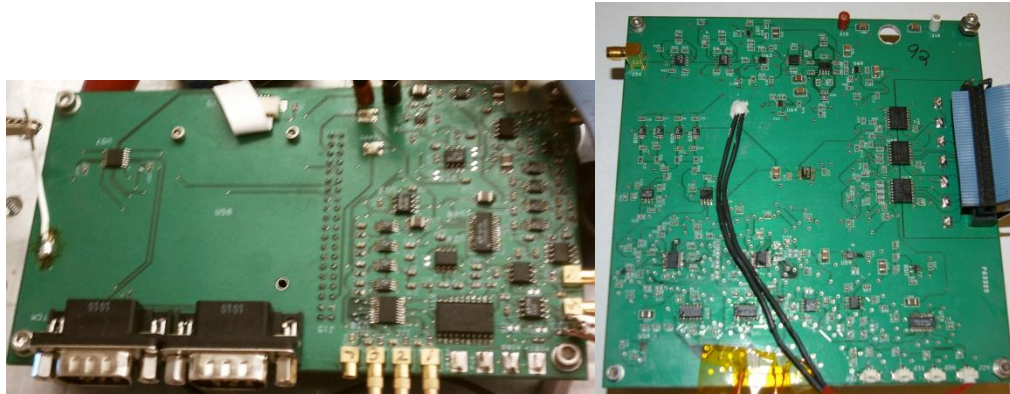


Figure B.1: Photos of the original data acquisition and control system PCB (*left*) and the final version (*right*).

The LT2439 ADC was initially used to sample the 92 GHz radiometer output voltage as well as the drain current. This implementation did not utilize the differential input capability of the ADC, which limited the amount of video gain, which could be applied. Consequently, a standalone ADC was used to record the measured voltage output of the power detector. Another change revolved around adding the option of connecting different voltages for the LNA gate bias voltage dividers instead of only the digital potentiometer. A voltage divider is a simpler and lower noise option than a digital potentiometer and ideally would be placed inside of the MCM near the biasing transmission lines. The only other major schematic change is also related to layout. AD4400 digital isolators were added to decouple any digital noise from the SAM3U-EK microcontroller development board. The SAM3U-EK uses an Atmel 32-bit ARM Cortex-M3 processor with 256 kB of flash and a 96 MHz maximum operating frequency [29]. The development board has support for NAND flash, SD card interface, three

USARTs, four SPIs, an eight channel 10-bit ADC, and an eight channel 12-bit ADC to name some of its pertinent features. The digital isolators bridged separate ground planes i.e. digital and analog grounds to prevent digital noise such as the microcontroller clock from coupling onto any of the analog measurements.

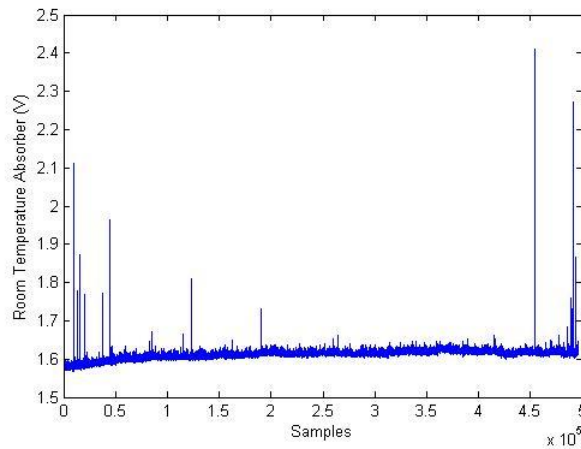


Figure B.2: Data viewing room temperature absorber with the original data acquisition board.¹⁴

The layout of the first PCB for the data acquisition and control system was produced on a 2-layer FR4 PCB. The main goal of the layout was to produce as compact of a system as possible. While this PCB did accomplish this task, it did so at the expense of a low noise and stable system, as shown in Figure B.2. It only shows the measurements in terms of voltage and not equivalent noise temperatures because a calibration wasn't performed. This noise resulted in the relaying out of the data acquisition and control board. The major takeaways from these PCB layout guidelines revolve around the ground plane. Digital traces such as clocks and data lines should ideally be sandwiched between ground or power layers [30] [31]. Any digital traces run on outer layers should have capacitors to ground as close as possible to this transition to

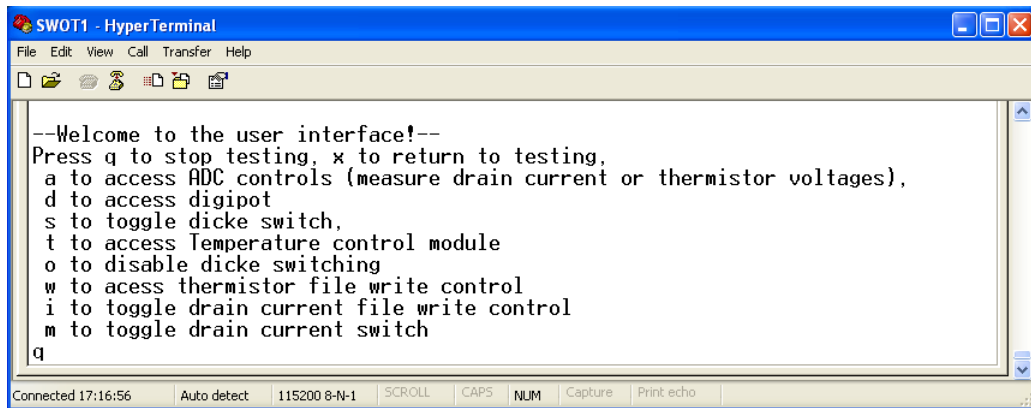
¹⁴ Overnight data from December 2 and 3, 2010.

provide a short return path for ground current. Sensitive analog components should be physically kept far away from noisy digital components or switching power supplies to prevent the coupling of noise. The biggest PCB layout lesson is to always consider what path the signal return ground current will take. The shortest return path for ground current is directly beneath the signal path because it is the lowest circuit loop inductance. This layout approach will prevent problematic ground loops and eliminate the formation of antennas which can pick up unwanted noise.

Appendix C

User Interface

The ability to control the switching, biasing, and see the measured data during testing of the radiometer is performed through a user interface (UI). This simple text based UI controls these features using Microsoft Window's Hyperterminal and an RS-232 serial port connection.



```
--Welcome to the user interface!--
Press q to stop testing, x to return to testing.
a to access ADC controls (measure drain current or thermistor voltages),
d to access digipot
s to toggle dicke switch,
t to access Temperature control module
o to disable dicke switching
w to access thermistor file write control
i to toggle drain current file write control
m to toggle drain current switch
q
```

Figure C.1: Menu for radiometer control and testing.

As shown in **Error! Reference source not found.**, Dicke switching can be enabled or disabled and the radiometer set to view either the antenna or matched load with a key press. The ability to record the thermistor readings and drain current is also configurable. The LNA gate biasing can be set if the digital potentiometers are being utilized instead of discrete resistor dividers. The most important feature is the ability to apply the LNA drain biasing after the gate bias to prevent damage to them. An option for configuring the active temperature control is shown as implemented in the code but was not ultimately used due to hardware limitations. Instead the default temperature control UI for the temperature controller was used from TE Technologies. The ADC option in the UI allows for the user to read the MCM voltages output, thermistor, and drain current values without recording the data to the SD card.

Several brief notes regarding the software architecture behind the UI and control of the radiometer. The software is written in the programming language of C on the SAM3U-EK microcontroller development board. When data is being recorded to the SD card, it is also being streamed to the Hyperterminal for viewing. Also, no data is written to the SD card while in the menus. The MCM voltage measurements are written to the SD card every 10 samples, and the Dicke switching rate is set to 56 Hz for the 92 GHz radiometer. Thermal and drain current measurements are recorded every 90 s as well as when entering and leaving the main menu. All of these sampling rates are easily configurable in software.

Appendix D

Bandpass Filter Design

D.1 Center BPF for HFSS

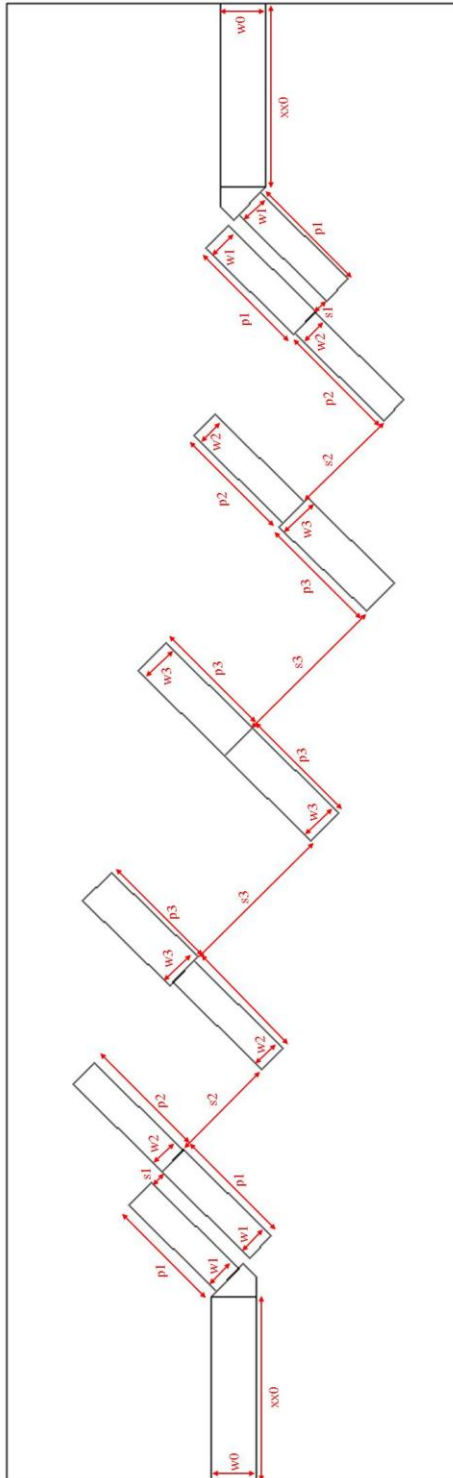


Figure D.1: Center BPF dimension variables for Ansoft HFSS.

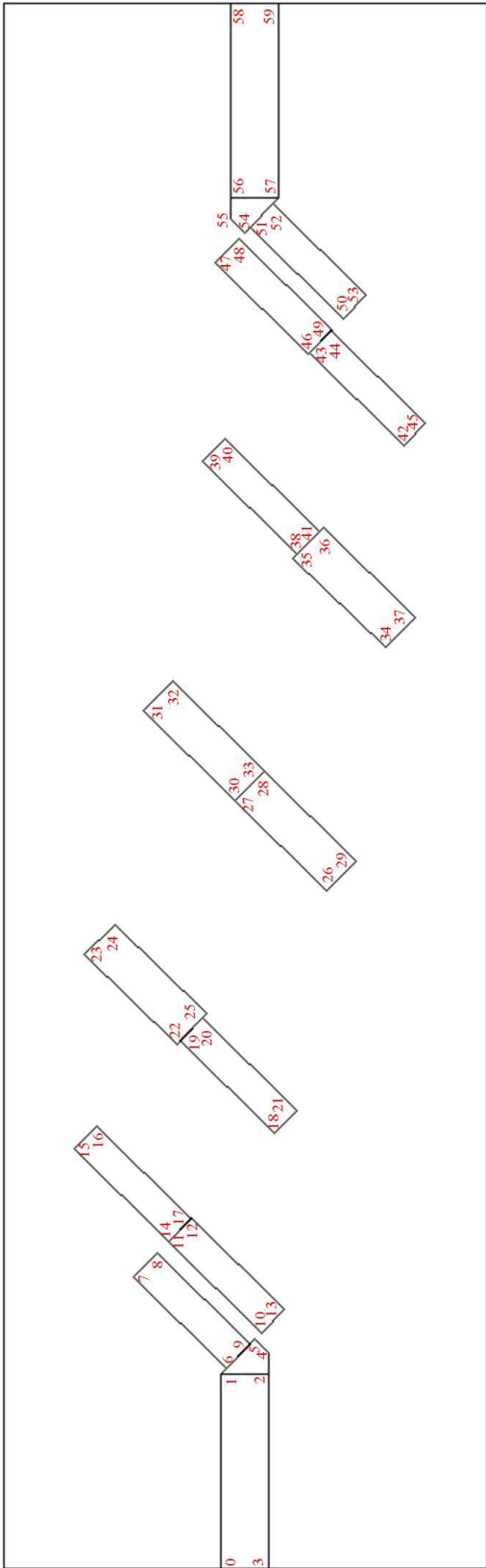


Figure D.2: Center BPF position coordinates for Ansoft HFSS.

xx = starting x coordinate
yy = starting y coordinate
sub_t = substrate thickness

$$\text{th} = \text{atan}((2*s1 + 2*s2 + 2*s3 + w1 + 2*w2 + 2*w3)/(2*p1 + 2*p2 + 2*p3))$$

$$x0 = \text{xx} + (w0 + w1)/2 * \sin(\text{th})$$

$$x1 = x0 + (s1 + w1) * \sin(\text{th})$$

$$x2 = x1 + p1 * \cos(\text{th}) - 0.5 * w1 * \sin(\text{th}) + 0.5 * w2 * \sin(\text{th})$$

$$x3 = x2 + (s2 + w2) * \sin(\text{th})$$

$$x4 = x3 + p2 * \cos(\text{th}) - 0.5 * w2 * \sin(\text{th}) + 0.5 * w3 * \sin(\text{th})$$

$$x5 = x4 + (s3 + w3) * \sin(\text{th})$$

$$x6 = x5 + p3 * \cos(\text{th})$$

$$x7 = x6 + (s3 + w3) * \sin(\text{th})$$

$$x8 = x7 + p3 * \cos(\text{th}) - 0.5 * w3 * \sin(\text{th}) + 0.5 * w2 * \sin(\text{th})$$

$$x9 = x8 + (s2 + w2) * \sin(\text{th})$$

$$x10 = x9 + p2 * \cos(\text{th}) - 0.5 * w2 * \sin(\text{th}) + 0.5 * w1 * \sin(\text{th})$$

$$x11 = x10 + (s1 + w1) * \sin(\text{th})$$

$$x12 = x11 + p1 * \cos(\text{th})$$

$$y0 = \text{yy} + w0 - (w0 + w1)/2 * \cos(\text{th})$$

$$y1 = y0 - (s1 + w1) * \cos(\text{th})$$

$$y2 = y1 + p1 * \sin(\text{th}) + 0.5 * w1 * \cos(\text{th}) - 0.5 * w2 * \cos(\text{th})$$

$$y3 = y2 - (s2 + w2) * \cos(\text{th})$$

$$y4 = y3 + p2 * \sin(\text{th}) + 0.5 * w2 * \cos(\text{th}) - 0.5 * w3 * \cos(\text{th})$$

$$y5 = y4 - (s3 + w3) * \cos(\text{th})$$

$$y6 = y5 + p3 * \sin(\text{th})$$

$$y7 = y6 - (s3 + w3) * \cos(\text{th})$$

$$y8 = y7 + p3 * \sin(\text{th}) + 0.5 * w3 * \cos(\text{th}) - 0.5 * w2 * \cos(\text{th})$$

$$y9 = y8 - (s2 + w2) * \cos(\text{th})$$

$$y10 = y9 + p2 * \sin(\text{th}) + 0.5 * w2 * \cos(\text{th}) - 0.5 * w1 * \cos(\text{th})$$

$$y11 = y10 - (s1 + w1) * \cos(\text{th})$$

$$y12 = y11 + p1 * \sin(\text{th})$$

$$0 = x12 + (w0 - w1)/2 * \cos(90\text{deg} - \text{th}) + \text{xx}0, y12 - (w0 - w1)/2 * \sin(90\text{deg} - \text{th}), \text{sub_t}$$

$$1 = x12 + (w0 - w1)/2 * \cos(90\text{deg} - \text{th}), y12 - (w0 - w1)/2 * \sin(90\text{deg} - \text{th}), \text{sub_t}$$

$$2 = x12 + (w0 - w1)/2 * \cos(90\text{deg} - \text{th}), y12 - (w0 - w1)/2 * \sin(90\text{deg} - \text{th}) + w0, \text{sub_t}$$

$$3 = x12 + (w0 - w1)/2 * \cos(90\text{deg} - \text{th}) + \text{xx}0, y12 - (w0 - w1)/2 * \sin(90\text{deg} - \text{th}) + w0, \text{sub_t}$$

$$4 = x12 + (w0 - w1)/2 * \cos(90\text{deg} - \text{th}) - w0 * \tan(\text{th}/2), y12 - (w0 - w1)/2 * \sin(90\text{deg} - \text{th}) + w0, \text{sub_t}$$

$$5 = x12 + (w0 - w1)/2 * \cos(90\text{deg} - \text{th}) - w0 * \tan(\text{th}/2) - w0 * \tan(\text{th}/2) * \cos(\text{th}), y12 - (w0 - w1)/2 * \sin(90\text{deg} - \text{th}) + w0 - w0 * \tan(\text{th}/2) * \sin(\text{th}), \text{sub_t}$$

$$6 = x11 + p1 * \cos(\text{th}), y11 + p1 * \sin(\text{th}), \text{sub_t}$$

$$7 = x11, y11, \text{sub_t}$$

$$8 = x11 - w1 * \sin(\text{th}), y11 + w1 * \cos(\text{th}), \text{sub_t}$$

$$9 = x11 - w1 * \sin(\text{th}) + p1 * \cos(\text{th}), y11 + w1 * \cos(\text{th}) + p1 * \sin(\text{th}), \text{sub_t}$$

$$10 = x10 + p1 * \cos(\text{th}), y10 + p1 * \sin(\text{th}), \text{sub_t}$$

$$11 = x10, y10, \text{sub_t}$$

12 = $x_{10} - w_1 \sin(\theta), y_{10} + w_1 \cos(\theta), \text{sub_t}$
 13 = $x_{10} - w_1 \sin(\theta) + p_1 \cos(\theta), y_{10} + w_1 \cos(\theta) + p_1 \sin(\theta), \text{sub_t}$
 14 = $x_9 + p_2 \cos(\theta), y_9 + p_2 \sin(\theta), \text{sub_t}$
 15 = $x_9, y_9, \text{sub_t}$
 16 = $x_9 - w_2 \sin(\theta), y_9 + w_2 \cos(\theta), \text{sub_t}$
 17 = $x_9 - w_2 \sin(\theta) + p_2 \cos(\theta), y_9 + w_2 \cos(\theta) + p_2 \sin(\theta), \text{sub_t}$
 18 = $x_8 + p_2 \cos(\theta), y_8 + p_2 \sin(\theta), \text{sub_t}$
 19 = $x_8, y_8, \text{sub_t}$
 20 = $x_8 - w_2 \sin(\theta), y_8 + w_2 \cos(\theta), \text{sub_t}$
 21 = $x_8 - w_2 \sin(\theta) + p_2 \cos(\theta), y_8 + w_2 \cos(\theta) + p_2 \sin(\theta), \text{sub_t}$
 22 = $x_7 + p_3 \cos(\theta), y_7 + p_3 \sin(\theta), \text{sub_t}$
 23 = $x_7, y_7, \text{sub_t}$
 24 = $x_7 - w_3 \sin(\theta), y_7 + w_3 \cos(\theta), \text{sub_t}$
 25 = $x_7 - w_3 \sin(\theta) + p_3 \cos(\theta), y_7 + w_3 \cos(\theta) + p_3 \sin(\theta), \text{sub_t}$
 26 = $x_6 + p_3 \cos(\theta), y_6 + p_3 \sin(\theta), \text{sub_t}$
 27 = $x_6, y_6, \text{sub_t}$
 28 = $x_6 - w_3 \sin(\theta), y_6 + w_3 \cos(\theta), \text{sub_t}$
 29 = $x_6 - w_3 \sin(\theta) + p_3 \cos(\theta), y_6 + w_3 \cos(\theta) + p_3 \sin(\theta), \text{sub_t}$
 30 = $x_5 + p_3 \cos(\theta), y_5 + p_3 \sin(\theta), \text{sub_t}$
 31 = $x_5, y_5, \text{sub_t}$
 32 = $x_5 - w_3 \sin(\theta), y_5 + w_3 \cos(\theta), \text{sub_t}$
 33 = $x_5 - w_3 \sin(\theta) + p_3 \cos(\theta), y_5 + w_3 \cos(\theta) + p_3 \sin(\theta), \text{sub_t}$
 34 = $x_4 + p_3 \cos(\theta), y_4 + p_3 \sin(\theta), \text{sub_t}$
 35 = $x_4, y_4, \text{sub_t}$
 36 = $x_4 - w_3 \sin(\theta), y_4 + w_3 \cos(\theta), \text{sub_t}$
 37 = $x_4 - w_3 \sin(\theta) + p_3 \cos(\theta), y_4 + w_3 \cos(\theta) + p_3 \sin(\theta), \text{sub_t}$
 38 = $x_3 + p_2 \cos(\theta), y_3 + p_2 \sin(\theta), \text{sub_t}$
 39 = $x_3, y_3, \text{sub_t}$
 40 = $x_3 - w_2 \sin(\theta), y_3 + w_2 \cos(\theta), \text{sub_t}$
 41 = $x_3 - w_2 \sin(\theta) + p_2 \cos(\theta), y_3 + w_2 \cos(\theta) + p_2 \sin(\theta), \text{sub_t}$
 42 = $x_2 + p_2 \cos(\theta), y_2 + p_2 \sin(\theta), \text{sub_t}$
 43 = $x_2, y_2, \text{sub_t}$
 44 = $x_2 - w_2 \sin(\theta), y_2 + w_2 \cos(\theta), \text{sub_t}$
 45 = $x_2 - w_2 \sin(\theta) + p_2 \cos(\theta), y_2 + w_2 \cos(\theta) + p_2 \sin(\theta), \text{sub_t}$
 46 = $x_1 + p_1 \cos(\theta), y_1 + p_1 \sin(\theta), \text{sub_t}$
 47 = $x_1, y_1, \text{sub_t}$
 48 = $x_1 - w_1 \sin(\theta), y_1 + w_1 \cos(\theta), \text{sub_t}$
 49 = $x_1 - w_1 \sin(\theta) + p_1 \cos(\theta), y_1 + w_1 \cos(\theta) + p_1 \sin(\theta), \text{sub_t}$
 50 = $x_0 + p_1 \cos(\theta), y_0 + p_1 \sin(\theta), \text{sub_t}$
 51 = $x_0, y_0, \text{sub_t}$
 52 = $x_0 - w_1 \sin(\theta), y_0 + w_1 \cos(\theta), \text{sub_t}$
 53 = $x_0 - w_1 \sin(\theta) + p_1 \cos(\theta), y_0 + w_1 \cos(\theta) + p_1 \sin(\theta), \text{sub_t}$
 54 = $xx + w_0 \tan(\theta/2) + w_0 \tan(\theta/2) \cos(\theta), yy + w_0 \tan(\theta/2) \sin(\theta), \text{sub_t}$
 55 = $xx + w_0 \tan(\theta/2), yy, \text{sub_t}$
 56 = $xx, yy, \text{sub_t}$
 57 = $xx, yy + w_0, \text{sub_t}$

58 = xx - xx0 ,yy ,2.9mil

59 = xx - xx0 ,yy + w0 ,2.9mil

D.2 Offset BPF for HFSS

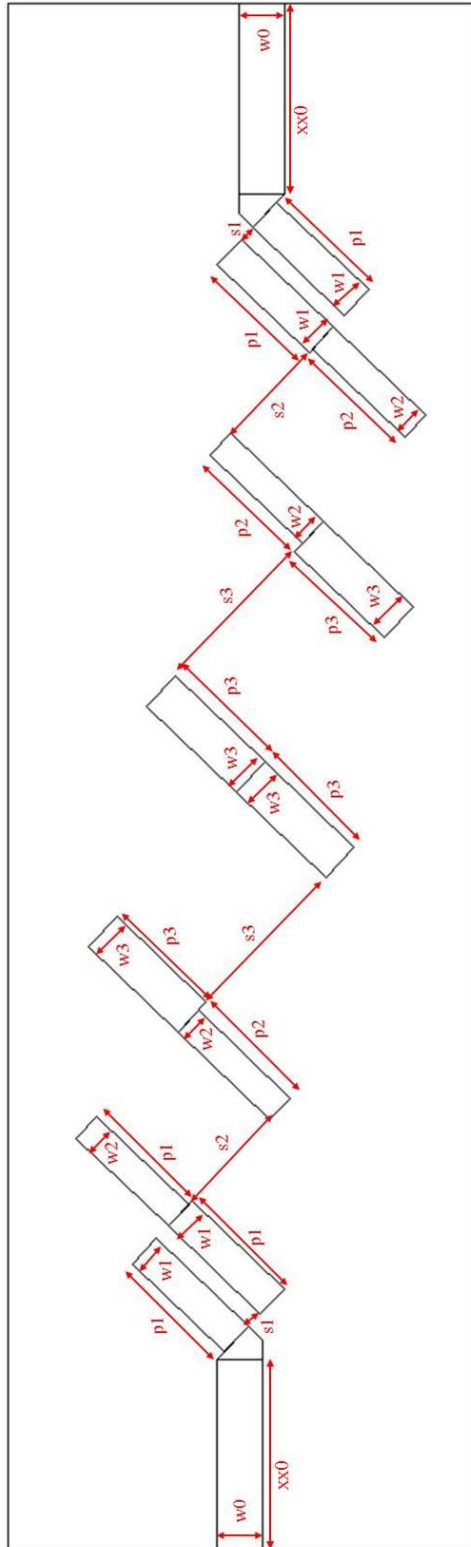


Figure D.3: Offset BPF dimension variables for Ansoft HFSS.

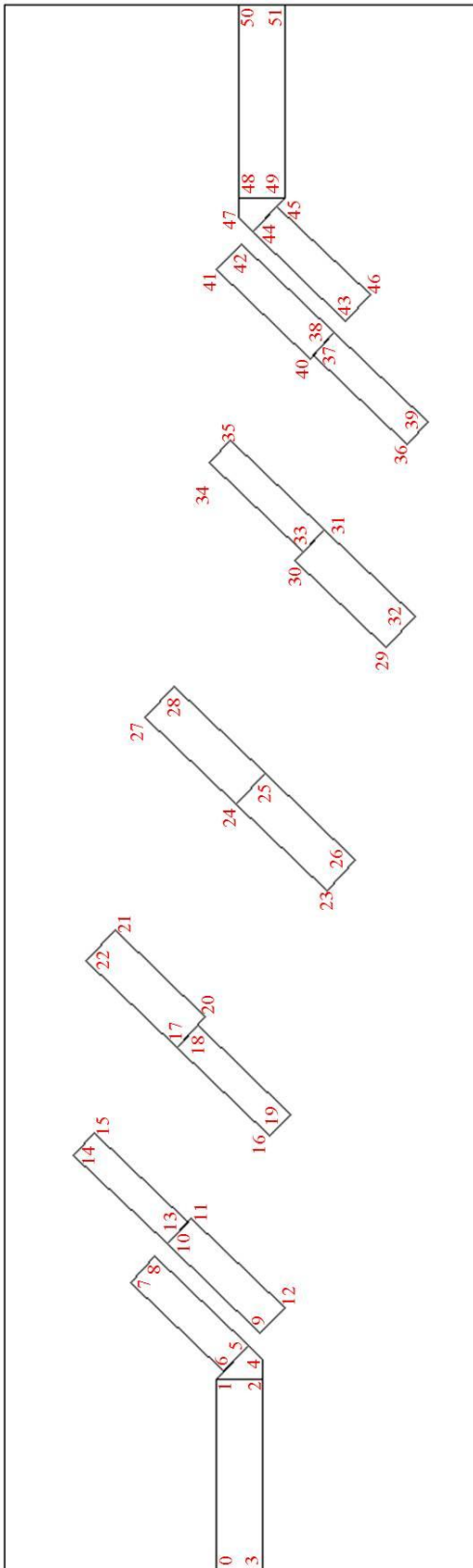


Figure D.4: Offset BPF position coordinates for Ansoft HFSS.

xx = starting x coordinate
yy = starting y coordinate
sub_t = substrate thickness

$$\text{th} = \text{atan}((2*s1 + 2*s2 + 2*s3 + w1 + 2*w2 + 2*w3)/(2*p1 + 2*p2 + 2*p3))$$

$$x0 = \text{xx} + w0 * \tan(\text{th}/2) + w0 * \tan(\text{th}/2) * \cos(\text{th})$$

$$x1 = x0 + (s1 + w1) * \sin(\text{th})$$

$$x2 = x1 + p1 * \cos(\text{th}) - w1 * \sin(\text{th}) + w2 * \sin(\text{th})$$

$$x3 = x2 + (s2 + w2) * \sin(\text{th})$$

$$x4 = x3 + p2 * \cos(\text{th}) - w2 * \sin(\text{th}) + w3 * \sin(\text{th})$$

$$x5 = x4 + (s3 + w3) * \sin(\text{th})$$

$$x6 = x5 + p3 * \cos(\text{th})$$

$$x7 = x6 + (s3 + w3) * \sin(\text{th})$$

$$x8 = x7 + p3 * \cos(\text{th})$$

$$x9 = x8 + (s2 + w2) * \sin(\text{th})$$

$$x10 = x9 + p2 * \cos(\text{th})$$

$$x11 = x10 + (s1 + w1) * \sin(\text{th})$$

$$x12 = x11 + p1 * \cos(\text{th})$$

$$y0 = \text{yy} + w0 - (w0 + w1) / 2 * \cos(\text{th})$$

$$y1 = y0 - (s1 + w1) * \cos(\text{th})$$

$$y2 = y1 + p1 * \sin(\text{th}) + w1 * \cos(\text{th}) - w2 * \cos(\text{th})$$

$$y3 = y2 - (s2 + w2) * \cos(\text{th})$$

$$y4 = y3 + p2 * \sin(\text{th}) + w2 * \cos(\text{th}) - w3 * \cos(\text{th})$$

$$y5 = y4 - (s3 + w3) * \cos(\text{th})$$

$$y6 = y5 + p3 * \sin(\text{th})$$

$$y7 = y6 - (s3 + w3) * \cos(\text{th})$$

$$y8 = y7 + p3 * \sin(\text{th})$$

$$y9 = y8 - (s2 + w2) * \cos(\text{th})$$

$$y10 = y9 + p2 * \sin(\text{th})$$

$$y11 = y10 - (s1 + w1) * \cos(\text{th})$$

$$y12 = y11 + p1 * \sin(\text{th})$$

$$0 = x12 + (w0 - w1) * \cos(90\text{deg} - \text{th}), y12 - (w0 - w1) * \sin(90\text{deg} - \text{th}), \text{sub_t}$$

$$1 = x12 + (w0 - w1) * \cos(90\text{deg} - \text{th}), y12 - (w0 - w1) * \sin(90\text{deg} - \text{th}) + w0, \text{sub_t}$$

$$2 = x12 + (w0 - w1) * \cos(90\text{deg} - \text{th}) + \text{xx}0, y12 - (w0 - w1) * \sin(90\text{deg} - \text{th}) + w0, \text{sub_t}$$

$$3 = x12 + (w0 - w1) * \cos(90\text{deg} - \text{th}) + \text{xx}0, y12 - (w0 - w1) * \sin(90\text{deg} - \text{th}), \text{sub_t}$$

$$4 = x12 + (w0 - w1) * \cos(90\text{deg} - \text{th}) - w0 * \tan(\text{th}/2), y12 - (w0 - w1) * \sin(90\text{deg} - \text{th}) + w0, \text{sub_t}$$

$$5 = x12 + (w0 - w1) * \cos(90\text{deg} - \text{th}) - w0 * \tan(\text{th}/2) - w0 * \tan(\text{th}/2) * \cos(\text{th}), y12 - (w0 - w1) * \sin(90\text{deg} - \text{th}) + w0 - w0 * \tan(\text{th}/2) * \sin(\text{th}), \text{sub_t}$$

$$6 = x12 + (w0 - w1) * \cos(90\text{deg} - \text{th}), y12 - (w0 - w1) * \sin(90\text{deg} - \text{th}), \text{sub_t}$$

$$7 = x11, y11, \text{sub_t}$$

$$8 = x11 - w1 * \sin(\text{th}), y11 + w1 * \cos(\text{th}), \text{sub_t}$$

$$9 = x10 + p1 * \cos(\text{th}), y10 + p1 * \sin(\text{th}), \text{sub_t}$$

$$10 = x10, y10, \text{sub_t}$$

$$11 = x10 - w1 * \sin(\text{th}), y10 + w1 * \cos(\text{th}), \text{sub_t}$$

$$12 = x10 - w1 * \sin(\text{th}) + p1 * \cos(\text{th}), y10 + w1 * \cos(\text{th}) + p1 * \sin(\text{th}), \text{sub_t}$$

13 = $x_9 - w_2 \sin(\theta) + p_2 \cos(\theta)$, $y_9 + w_2 \cos(\theta) + p_2 \sin(\theta)$,sub_t
14 = x_9 , y_9 ,sub_t
15 = $x_9 - w_2 \sin(\theta)$, $y_9 + w_2 \cos(\theta)$,sub_t
16 = $x_8 + p_2 \cos(\theta)$, $y_8 + p_2 \sin(\theta)$,sub_t
17 = x_8 , y_8 ,sub_t
18 = $x_8 - w_2 \sin(\theta)$, $y_8 + w_2 \cos(\theta)$,sub_t
19 = $x_8 - w_2 \sin(\theta) + p_2 \cos(\theta)$, $y_8 + w_2 \cos(\theta) + p_2 \sin(\theta)$,sub_t
20 = $x_7 - w_3 \sin(\theta) + p_3 \cos(\theta)$, $y_7 + w_3 \cos(\theta) + p_3 \sin(\theta)$,sub_t
21 = $x_7 - w_3 \sin(\theta)$, $y_7 + w_3 \cos(\theta)$,sub_t
22 = x_7 , y_7 ,sub_t
23 = $x_6 + p_3 \cos(\theta)$, $y_6 + p_3 \sin(\theta)$,sub_t
24 = x_6 , y_6 ,sub_t
25 = $x_6 - w_3 \sin(\theta)$, $y_6 + w_3 \cos(\theta)$,sub_t
26 = $x_6 - w_3 \sin(\theta) + p_3 \cos(\theta)$, $y_6 + w_3 \cos(\theta) + p_3 \sin(\theta)$,sub_t
27 = x_5 , y_5 ,sub_t
28 = $x_5 - w_3 \sin(\theta)$, $y_5 + w_3 \cos(\theta)$,sub_t
29 = $x_4 + p_3 \cos(\theta)$, $y_4 + p_3 \sin(\theta)$,sub_t
30 = x_4 , y_4 ,sub_t
31 = $x_4 - w_3 \sin(\theta)$, $y_4 + w_3 \cos(\theta)$,sub_t
32 = $x_4 - w_3 \sin(\theta) + p_3 \cos(\theta)$, $y_4 + w_3 \cos(\theta) + p_3 \sin(\theta)$,sub_t
33 = $x_3 + p_2 \cos(\theta)$, $y_3 + p_2 \sin(\theta)$,sub_t
34 = x_3 , y_3 ,sub_t
35 = $x_3 - w_2 \sin(\theta)$, $y_3 + w_2 \cos(\theta)$,sub_t
36 = $x_2 + p_2 \cos(\theta)$, $y_2 + p_2 \sin(\theta)$,sub_t
37 = x_2 , y_2 ,sub_t
38 = $x_2 - w_2 \sin(\theta)$, $y_2 + w_2 \cos(\theta)$,sub_t
39 = $x_2 - w_2 \sin(\theta) + p_2 \cos(\theta)$, $y_2 + w_2 \cos(\theta) + p_2 \sin(\theta)$,sub_t
40 = $x_1 + p_1 \cos(\theta)$, $y_1 + p_1 \sin(\theta)$,sub_t
41 = x_1 , y_1 ,sub_t
42 = $x_1 - w_1 \sin(\theta)$, $y_1 + w_1 \cos(\theta)$,sub_t
43 = $x_0 + p_1 \cos(\theta)$, $y_0 + p_1 \sin(\theta)$,sub_t
44 = x_0 , y_0 ,sub_t
45 = $x_0 - w_1 \sin(\theta)$, $y_0 + w_1 \cos(\theta)$,sub_t
46 = $x_0 - w_1 \sin(\theta) + p_1 \cos(\theta)$, $y_0 + w_1 \cos(\theta) + p_1 \sin(\theta)$,sub_t
47 = $xx + w_0 \tan(\theta/2)$, $y_0 + w_0 \cos(\theta) - w_0$,sub_t
48 = $x_0 - w_0 \sin(\theta)$, $y_0 + w_0 \cos(\theta) - w_0$,sub_t
49 = $x_0 - w_0 \sin(\theta)$, $y_0 + w_0 \cos(\theta)$,sub_t
50 = $x_0 - w_0 \sin(\theta) - xx_0$, $y_0 + w_0 \cos(\theta) - w_0$, sub_t
51 = $x_0 - w_0 \sin(\theta) - xx_0$, $y_0 + w_0 \cos(\theta)$, sub_t

Appendix E

92 GHz Radiometer

E.1 Passive Components

All units are in mils and the passive components are produced on 5 mil thick alumina substrate with 0.125 mil thick gold microstrip lines. All resistors are TaN with an *sq* of

25 Ω /sq.

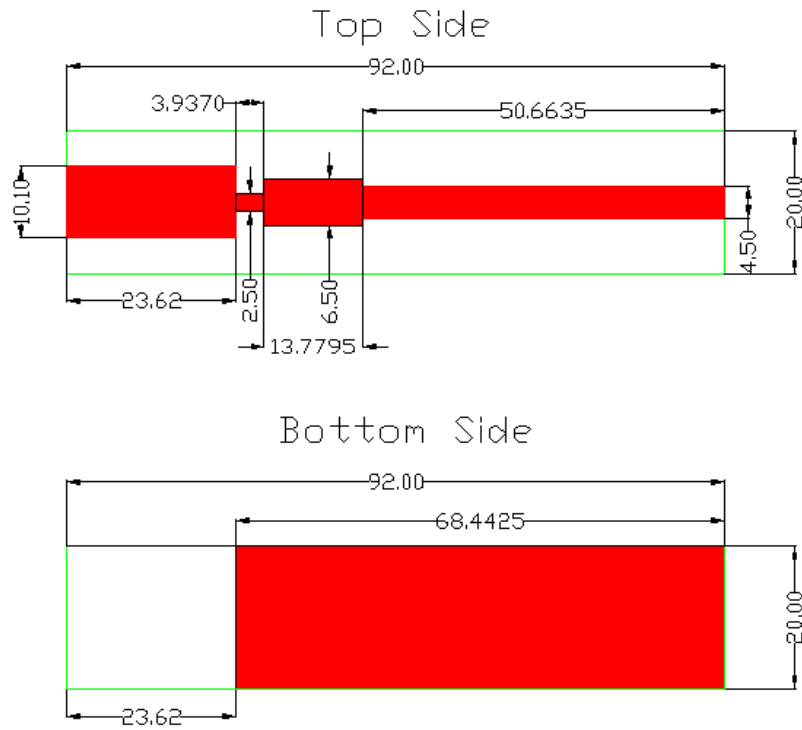


Figure E.1: Waveguide-to-Microstrip

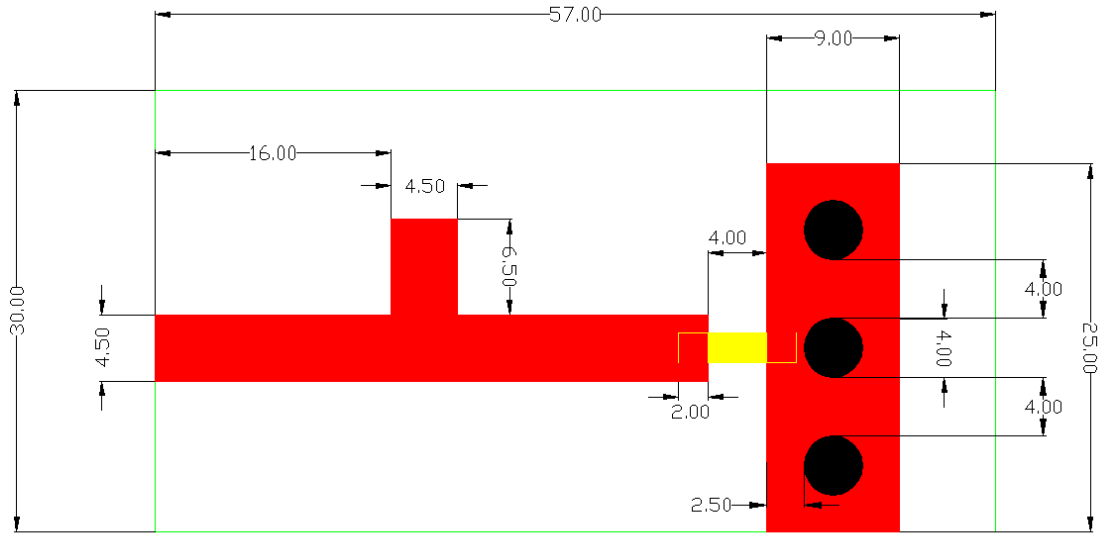


Figure E.2: 50Ω matched load with ground vias

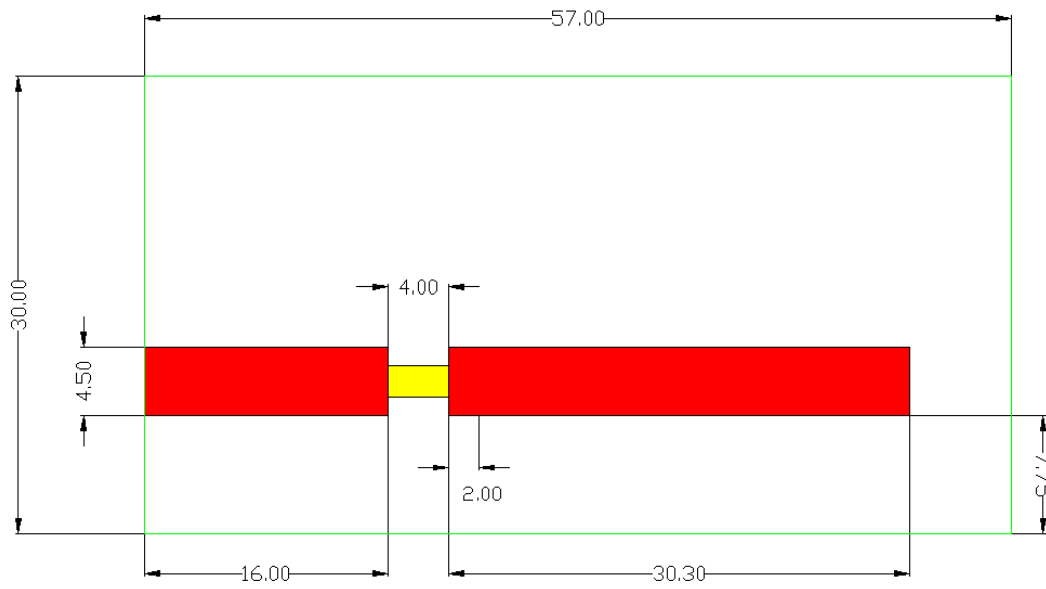


Figure E.3: 50 Ω matched load with virtual ground

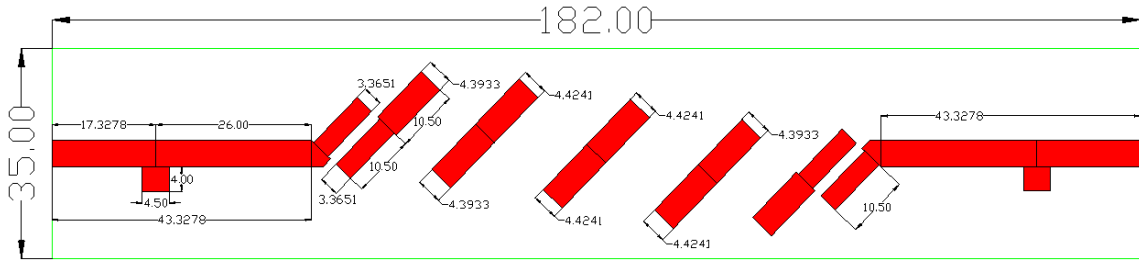


Figure E.4: Bandpass filter

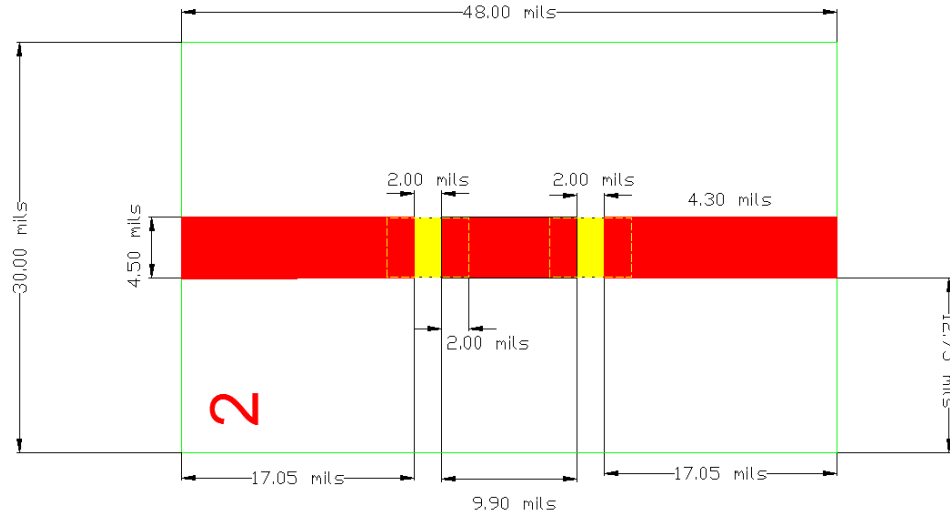


Figure E.5: 2 dB attenuator

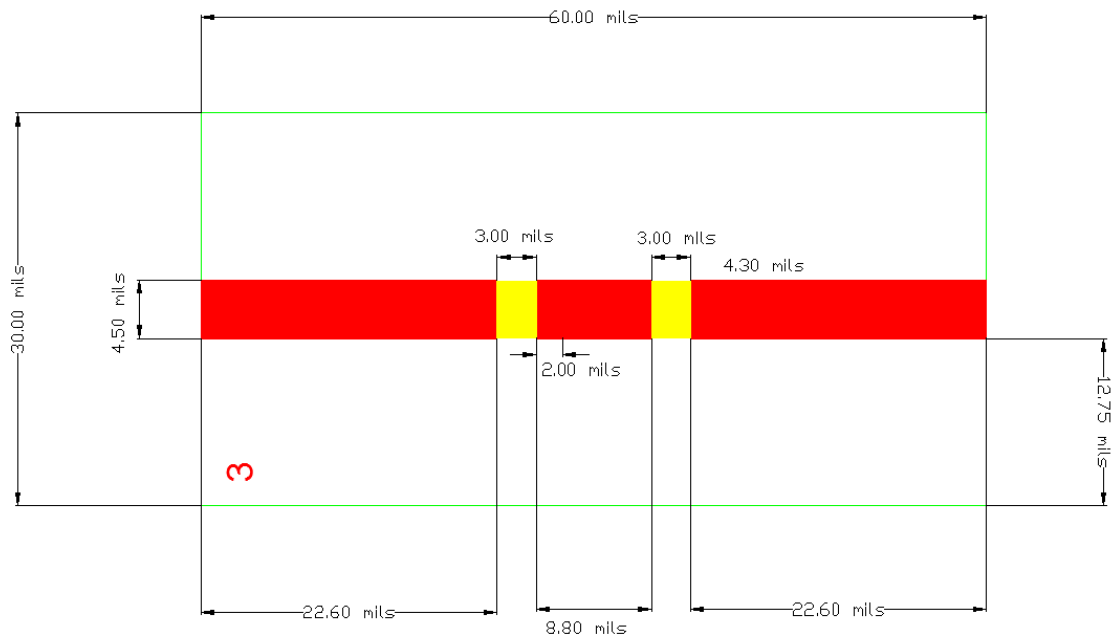


Figure E.6: 3 dB attenuator

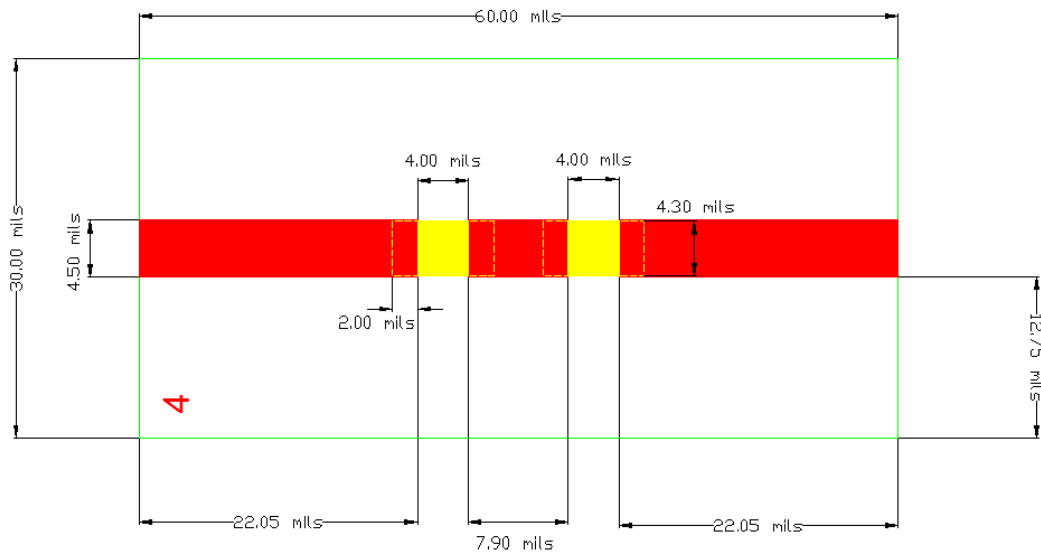


Figure E.7: 4 dB attenuator

E.2 92 GHz Bias Boards

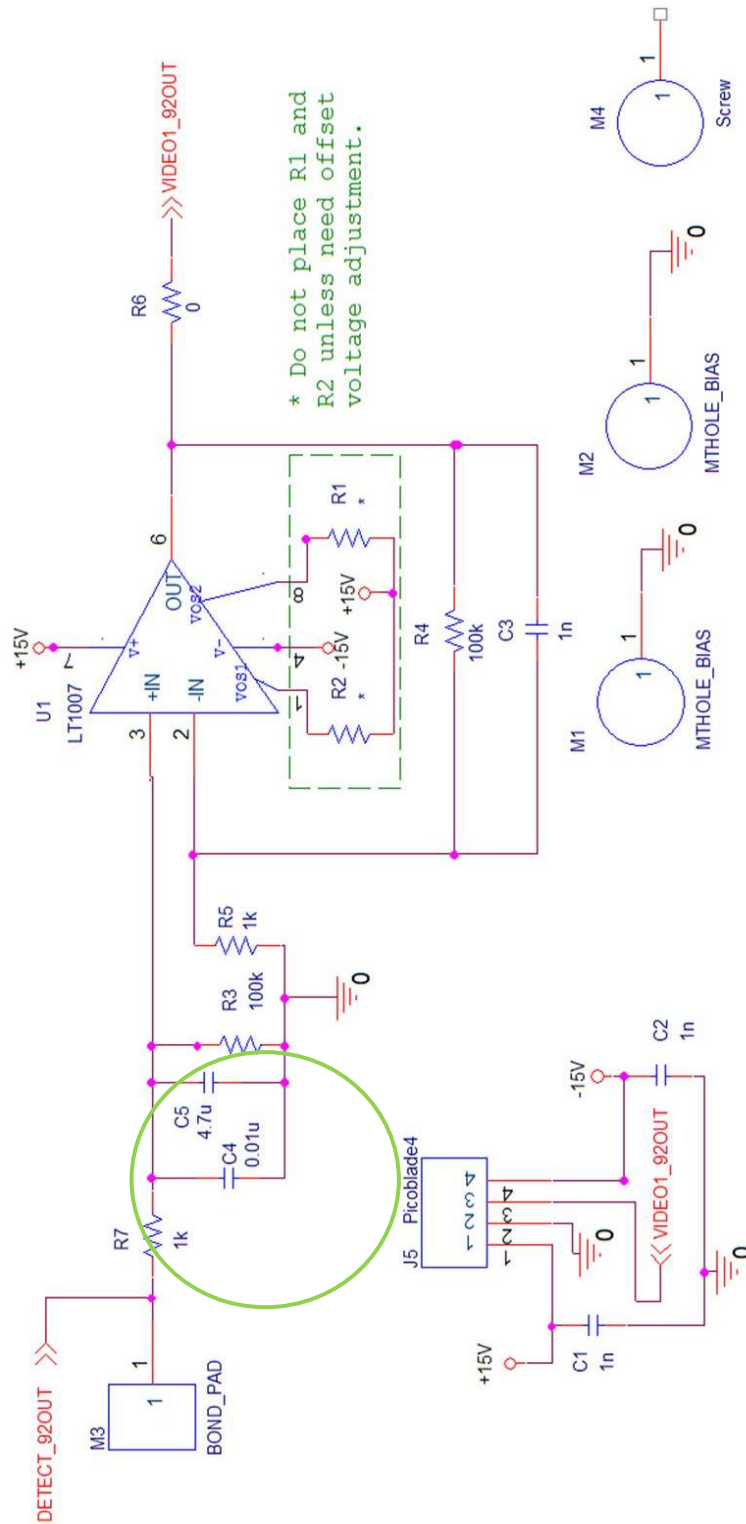


Figure E.8: 92 GHz MCM bias board with video gain. Green circle not implemented in layout of ordered PCB.

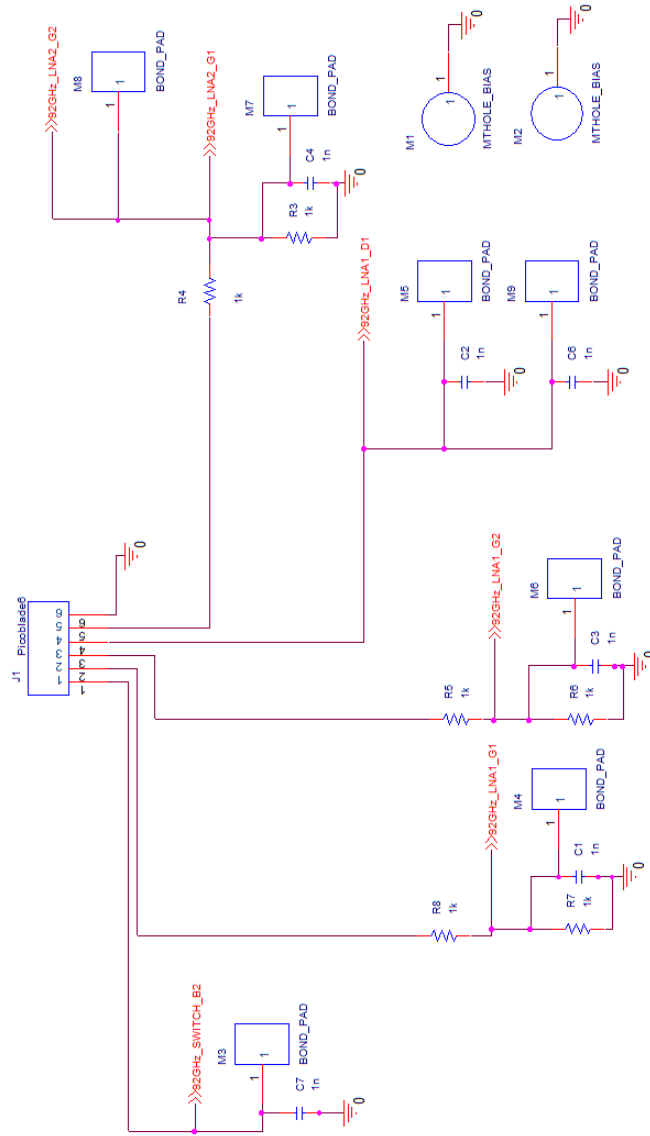


Figure E.9: 92 GHz MCM bias board with LNA drain and gate bias as well as switch bias.

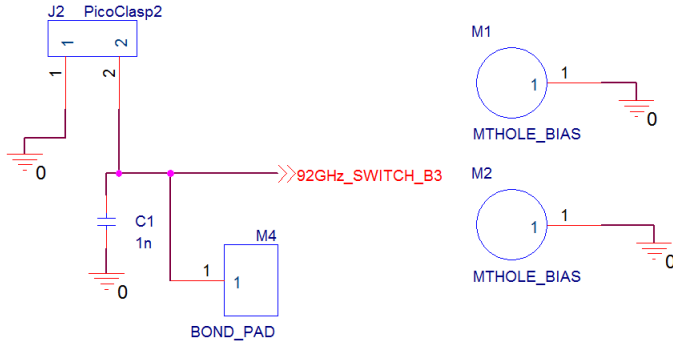


Figure E.10: 92 GHz MCM bias board with switch bias.

E.3 Temperature Control Module Settings

The screenshot displays the 'SETUP PROGRAM FOR TC-36-25 RS232 - TC-36-25 RS232 REVA' software interface. The window title bar includes 'File' and 'Help' menus. The main content area is divided into several functional sections:

- TUNING:** Contains input fields for 'FIXED SET TEMP.' (28.00), 'PROPORTIONAL BANDWIDTH' (5.5), 'INTEGRAL GAIN' (0.98), 'DERIVATIVE GAIN' (0.00), and 'CONTROL DEADBAND' (2.00). A 'Send Box Values' button is present.
- CALIBRATE:** Contains input fields for 'INPUT1 OFFSET' (0.00), 'INPUT2 OFFSET' (0.00), 'HEAT SIDE MULTIPLIER' (1.00), and 'COOL SIDE MULTIPLIER' (1.00). A 'Send Box Values' button is present.
- PC COMMUNICATIONS:** Includes a 'SELECT COMM PORT' dropdown set to 'COM1', 'INITIALIZE' and 'CommCheck' buttons, and a checked 'EEPROM WRITE ENABLE' checkbox.
- CONFIGURE:** This is the largest section, containing:
 - 'COMPUTER SET VALUE' dropdown and 'SET TEMP TYPE' dropdown.
 - 'SET TEMP HIGH RANGE' (30.00) and 'SET TEMP LOW RANGE' (20.00) input fields, with a 'DISPLAY FUNCTION ENABLE' checkbox.
 - 'PID CONTROL' dropdown and 'CONTROL TYPE' dropdown, with a 'Send Box Values' button.
 - 'HEAT W/P1+ AND W/P2-' dropdown and 'CONTROL MODE' dropdown.
 - 'NO ALARMS PICKED' dropdown and 'ALARM TYPE' dropdown.
 - 'NO SHUTDOWN IF ALARM' dropdown and 'POWER OUT SHUT DOWN IF ALARM' dropdown.
 - 'HIGH ALARM SETTING' (35.00) and 'LOW ALARM SETTING' (20.00) input fields, with an 'OUTPUT ON/OFF' dropdown set to 'ON'.
 - 'ALARM DEADBAND' (1.00) input field.
 - 'ALARM LATCH OFF' dropdown and 'ALARM LATCH' dropdown, with a 'SEND LATCH CLEAR' button.
 - 'TS-67.TS132.15K' dropdown and 'SENSOR TYPE' dropdown.
 - 'CONTROL SENSOR' dropdown and 'CHOOSE SENSOR FOR ALARM' dropdown.
 - 'DEG C' dropdown and 'CHOOSE DEGC OR DEGF UNITS' dropdown.
 - 'OVER-CURRENT LEVEL: 17.5' dropdown and 'AMPS (APPROXIMATE)' dropdown.
 - 'OVER-CURRENT RESTART ATTEMPTS: 100' input field and a checked 'CONTINUOUS' checkbox.
- DATA ACQUISITION:** Contains:
 - 'SAMPLE TIME IN SECONDS' (1) input field.
 - 'DATA LOG BOX' and 'BOX ENABLE' checkbox.
 - 'SAMPLE' and 'SAMPLING INDICATOR' radio buttons.
 - Log enable checkboxes for 'TEMP' (28.00), 'SET TEMP' (28.00), 'OUTPUT' (7.8), and 'INPUT 2 AS TEMP.' (155.86).
 - 'OVER CURRENT' and 'LOW VOLTAGE' radio buttons.

On the right side of the interface, there are buttons for 'SEND SET RANGE TO DISPLAY', 'DOWNLOAD DEFAULTS', and 'VERIFY DEFAULTS'. At the bottom right, an 'OVER CURRENT COUNT' field shows the value '137'.

Figure E.11: TCM settings for 92 GHz radiometer.

Appendix F

130 GHz Radiometer

F.1 Passive Components

All units are in mils and the passive components are produced on 3 mil thick alumina substrate with 0.1 mil thick gold microstrip lines.

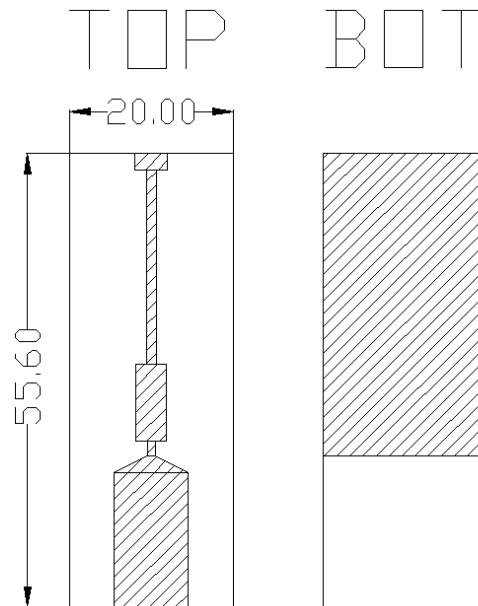


Figure F.1: Waveguide-to-microstrip

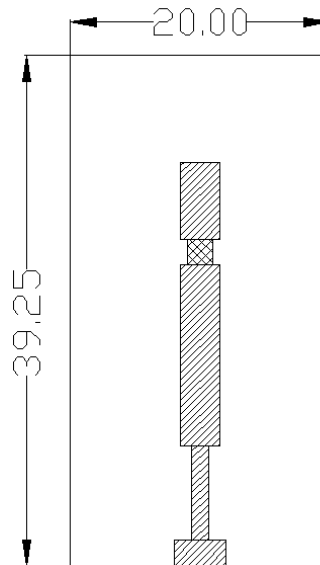


Figure F.2: Matched load with virtual grounds and TaN resistors of $50 \Omega/\text{sq}$

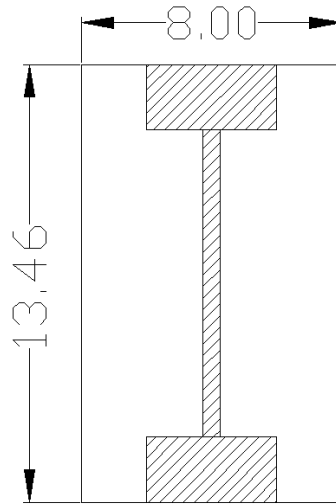


Figure F.3: Interconnect

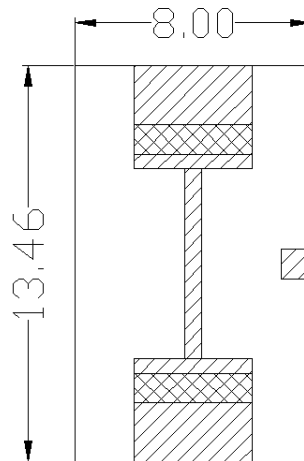


Figure F.4: Interconnect with attenuation and TaN resistors of $100 \Omega/\text{sq}$

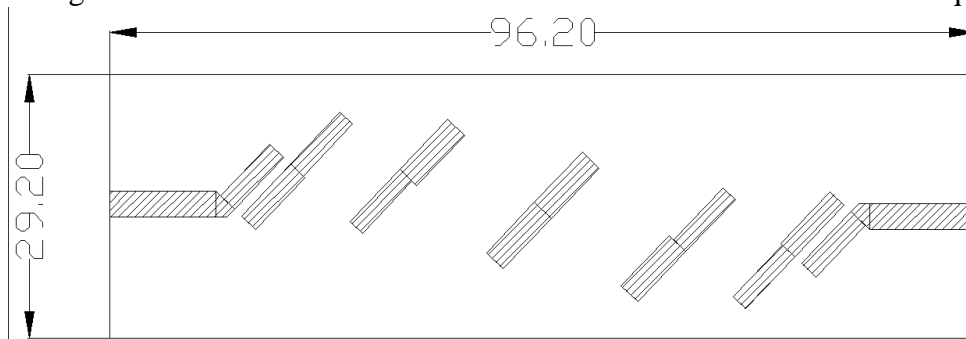


Figure F.5: 5 GHz bandpass filter

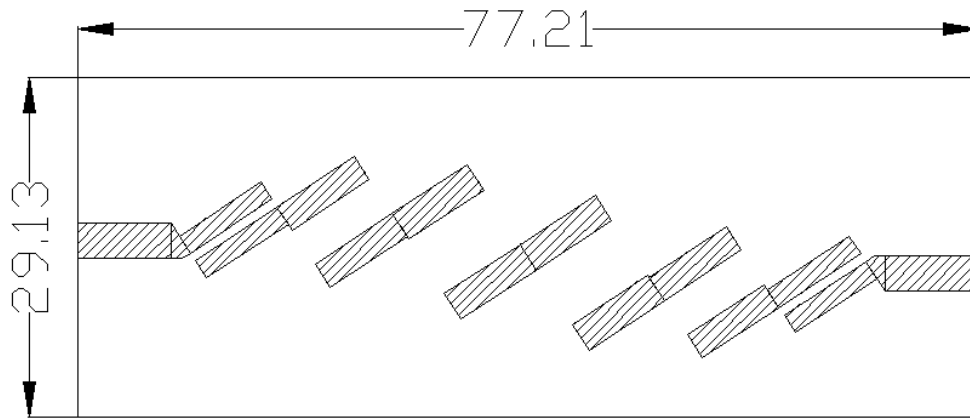


Figure F.6: 10 GHz bandpass filter

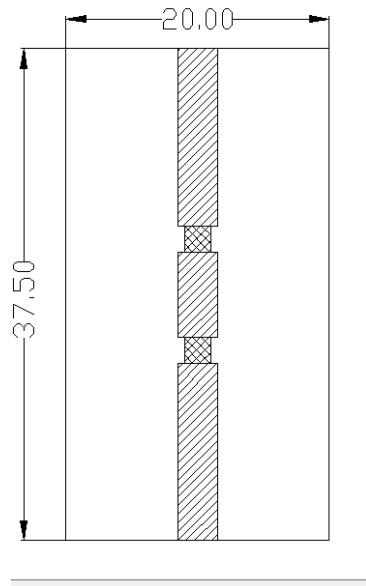


Figure F.7: Attenuator with TaN resistors of $25 \Omega/\text{sq}$

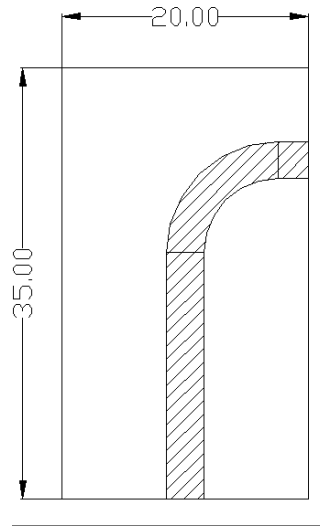


Figure F.8: Right angle bend

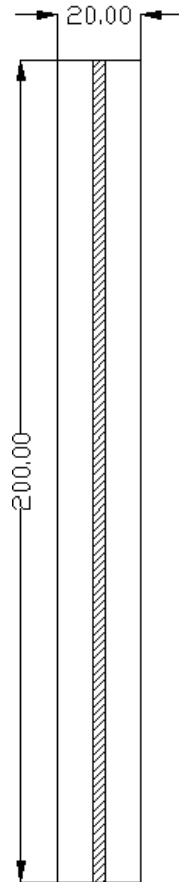


Figure F.9: Transmission line

F.2 130 GHz Bias Board

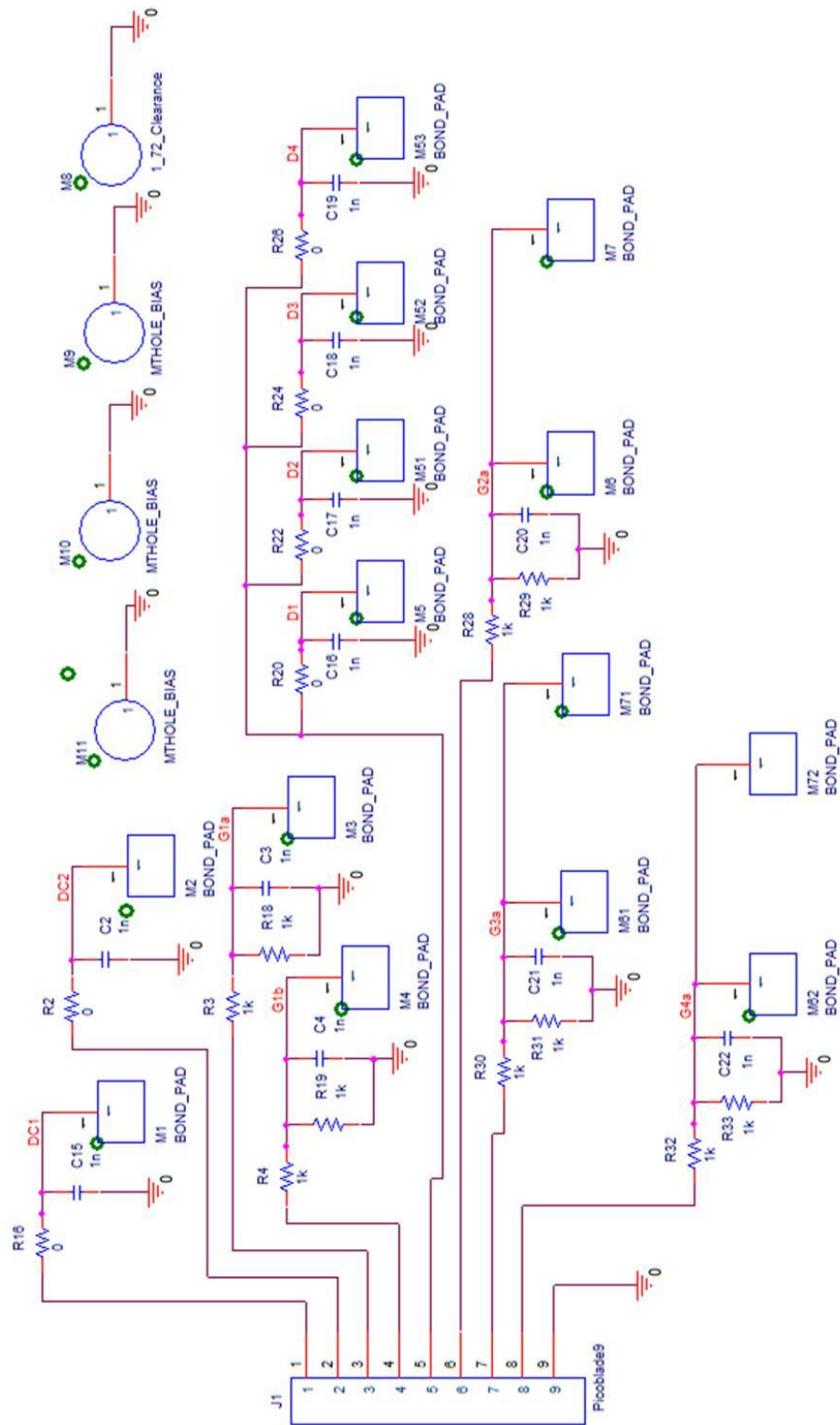


Figure F.10: 130 GHz MCM bias board.

F.3 Temperature Control Module Settings

The screenshot shows the 'SETUP PROGRAM FOR TC-36-25 RS232 - TC-36-25 RS232 REVA' window. It features several configuration panels:

- TUNING:** Includes fields for FIXED SET TEMP (28.00), PROPORTIONAL BANDWIDTH (19.80), INTEGRAL GAIN (0.94), DERIVATIVE GAIN (0.00), and CONTROL DEADBAND (2.00). A 'Send Box Values' button is present.
- CALIBRATE:** Includes fields for INPUT1 OFFSET (0.00), INPUT2 OFFSET (0.00), HEAT SIDE MULTIPLIER (1.00), and COOL SIDE MULTIPLIER (1.00). A 'Send Box Values' button is present.
- PC COMMUNICATIONS:** Includes a 'SELECT COMM PORT' dropdown (COM1), an 'INITIALIZE' button, and a 'CommCheck' button.
- CONFIGURE:** This is the largest panel, containing:
 - COMPUTER SET VALUE dropdown, SET TEMP TYPE dropdown, SET TEMP HIGH RANGE (30.00), SET TEMP LOW RANGE (20.00), and a 'DISPLAY FUNCTION ENABLE' checkbox.
 - PID CONTROL dropdown, CONTROL TYPE dropdown, and a 'Send Box Values' button.
 - HEAT WP1+ AND WP2- dropdown, CONTROL MODE dropdown.
 - NO ALARMS PICKED dropdown, ALARM TYPE dropdown.
 - NO SHUTDOWN IF ALARM dropdown, POWER OUT SHUT DOWN IF ALARM dropdown.
 - HIGH ALARM SETTING (35.00), LOW ALARM SETTING (20.00), and an 'OUTPUT ON/OFF' dropdown (ON).
 - ALARM DEADBAND (1.00).
 - ALARM LATCH OFF dropdown, ALARM LATCH dropdown, and a 'SEND LATCH CLEAR' button.
 - TS-67.TS132.15K dropdown, SENSOR TYPE dropdown.
 - CONTROL SENSOR dropdown, CHOOSE SENSOR FOR ALARM dropdown.
 - DEG C dropdown, CHOOSE DEGC OR DEGF UNITS dropdown.
 - OVER-CURRENT LEVEL: 17.5 AMPS (APPROXIMATE) dropdown.
 - OVER-CURRENT RESTART ATTEMPTS: 100, and a 'CONTINUOUS' checkbox.
- DATA ACQUISITION:** Includes a 'SAMPLE TIME IN SECONDS' field (1), a 'DATA LOG BOX' with a 'BOX ENABLE' checkbox, and a 'SAMPLE' section with 'SAMPLING INDICATOR' selected. Below this are fields for TEMP (28.15), SET TEMP (28.00), OUTPUT (7.4), and INPUT 2 AS TEMP (155.88), each with a 'LOG ENABLE' checkbox. There are also radio buttons for 'OVER CURRENT' and 'LOW VOLTAGE'.

At the bottom right, there are buttons for 'SEND SET RANGE TO DISPLAY', 'DOWNLOAD DEFAULTS', 'VERIFY DEFAULTS', and an 'OVER CURRENT COUNT' field showing '137'.

Figure F.11: TCM settings for 130 GHz radiometer.

Appendix G

Base Data acquisition and control PCB

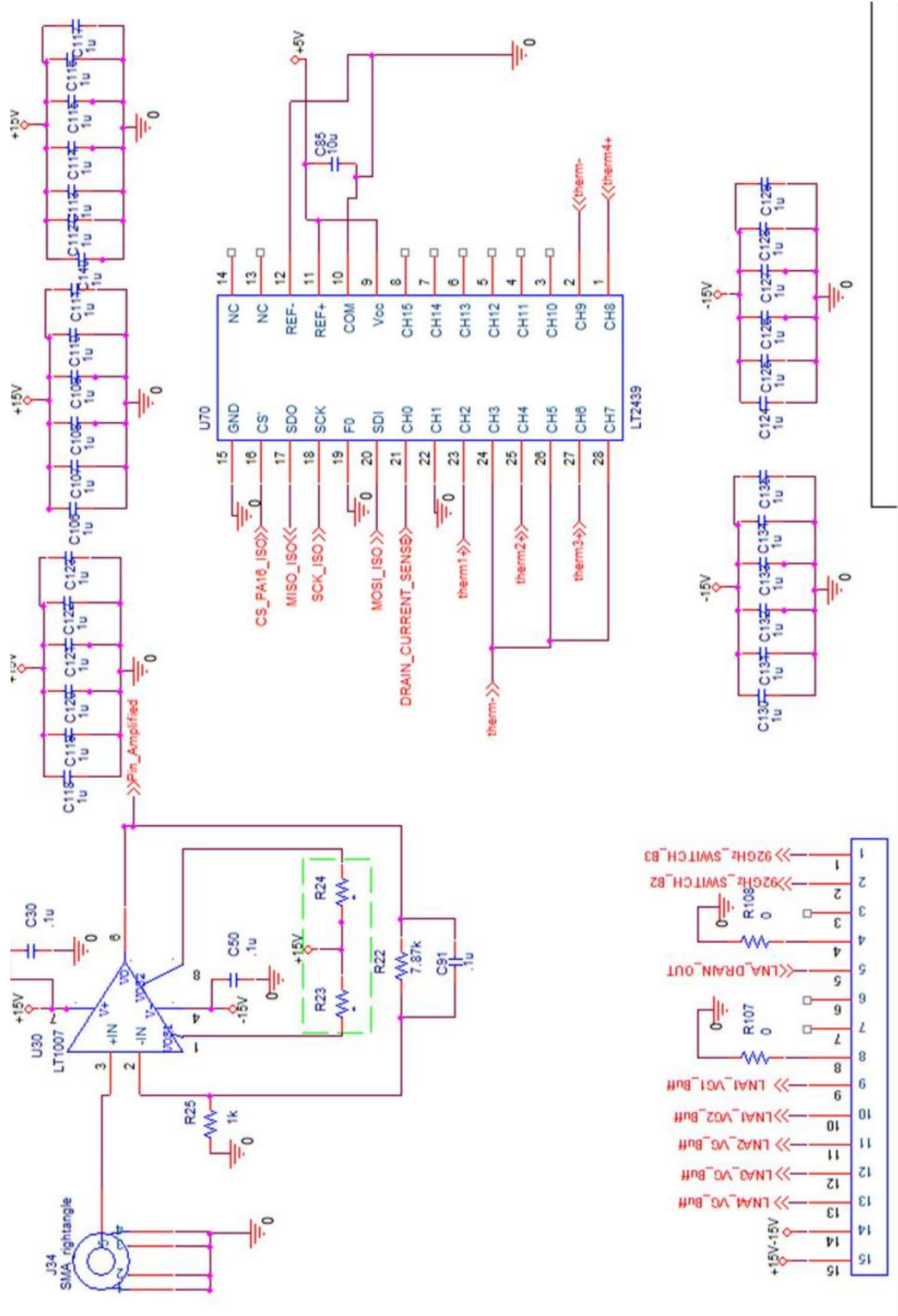


Figure G.1: Page 0 of data acquisition PCB.

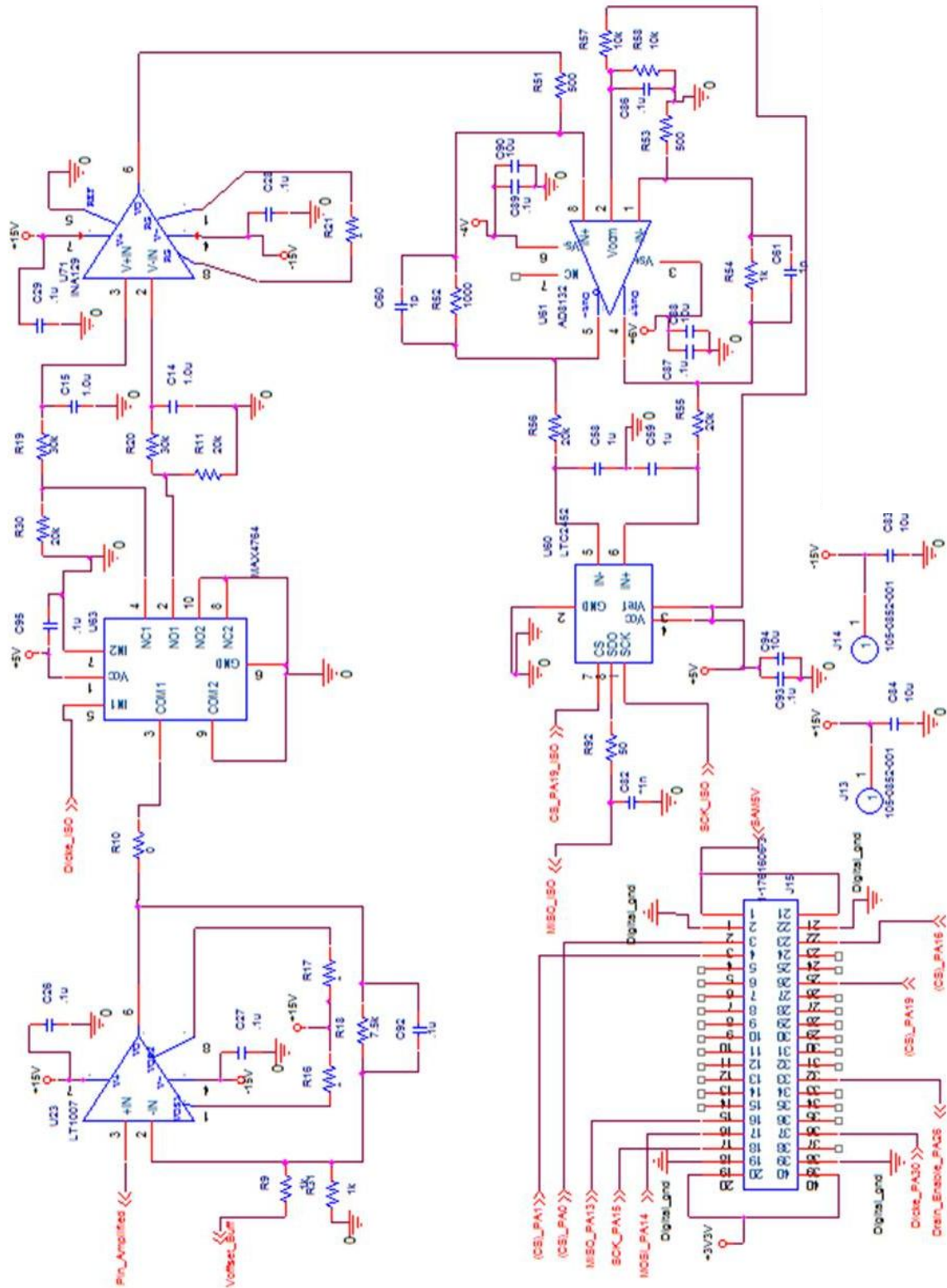


Figure G.2: Page 1 of data acquisition PCB.

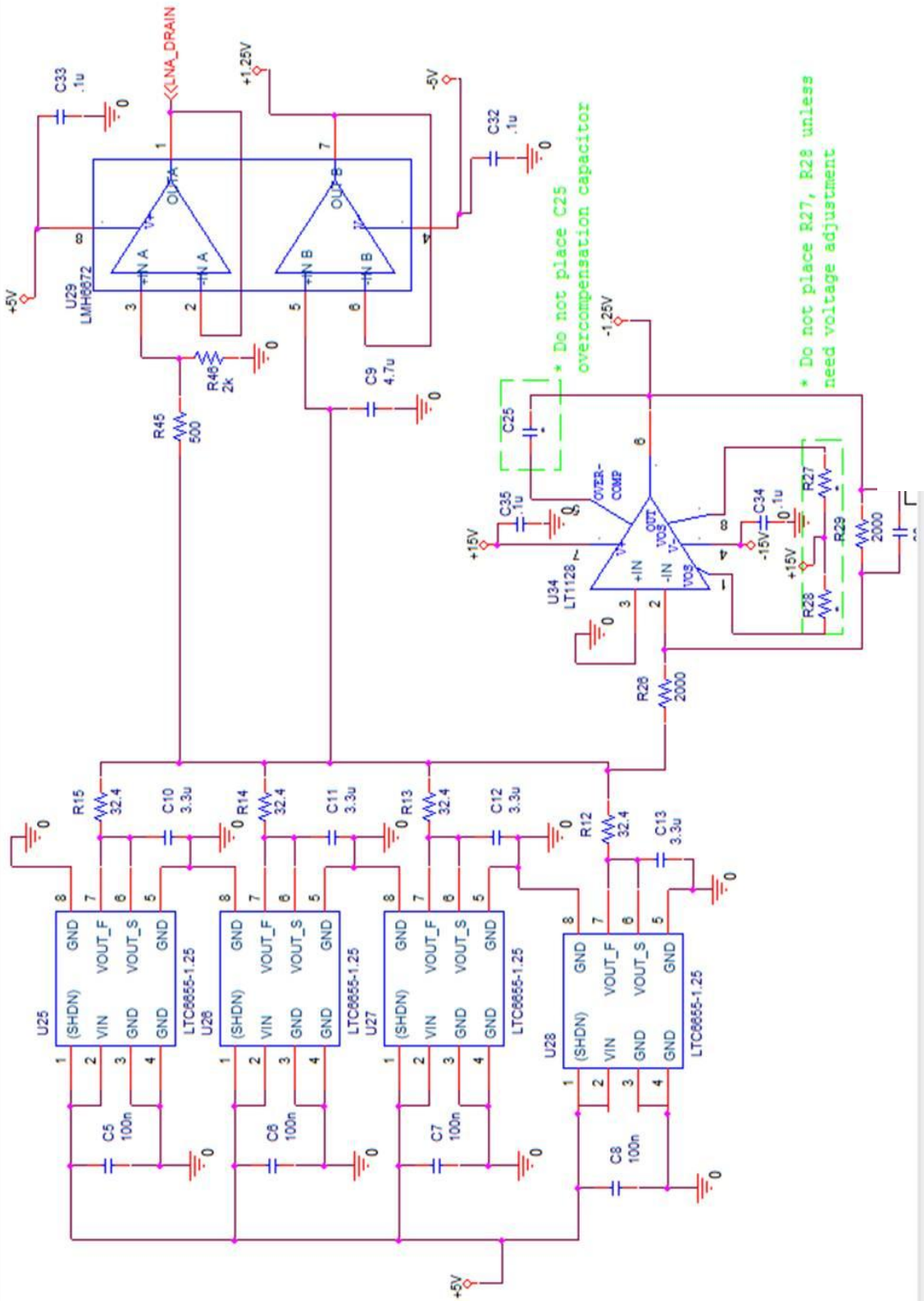


Figure G.3: Page 2 of data acquisition PCB.

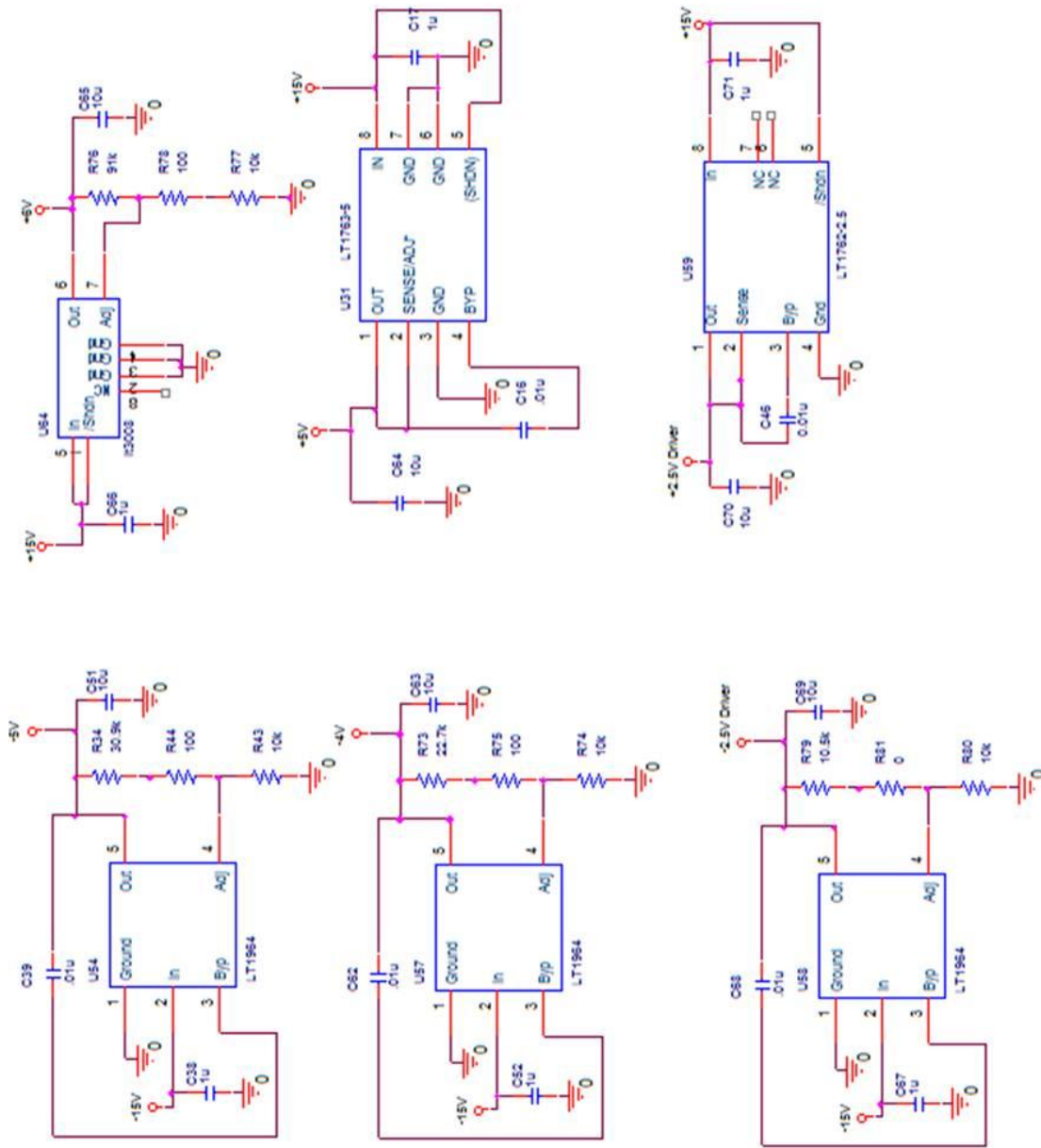


Figure G.4:Page 3 of data acquisition PCB.

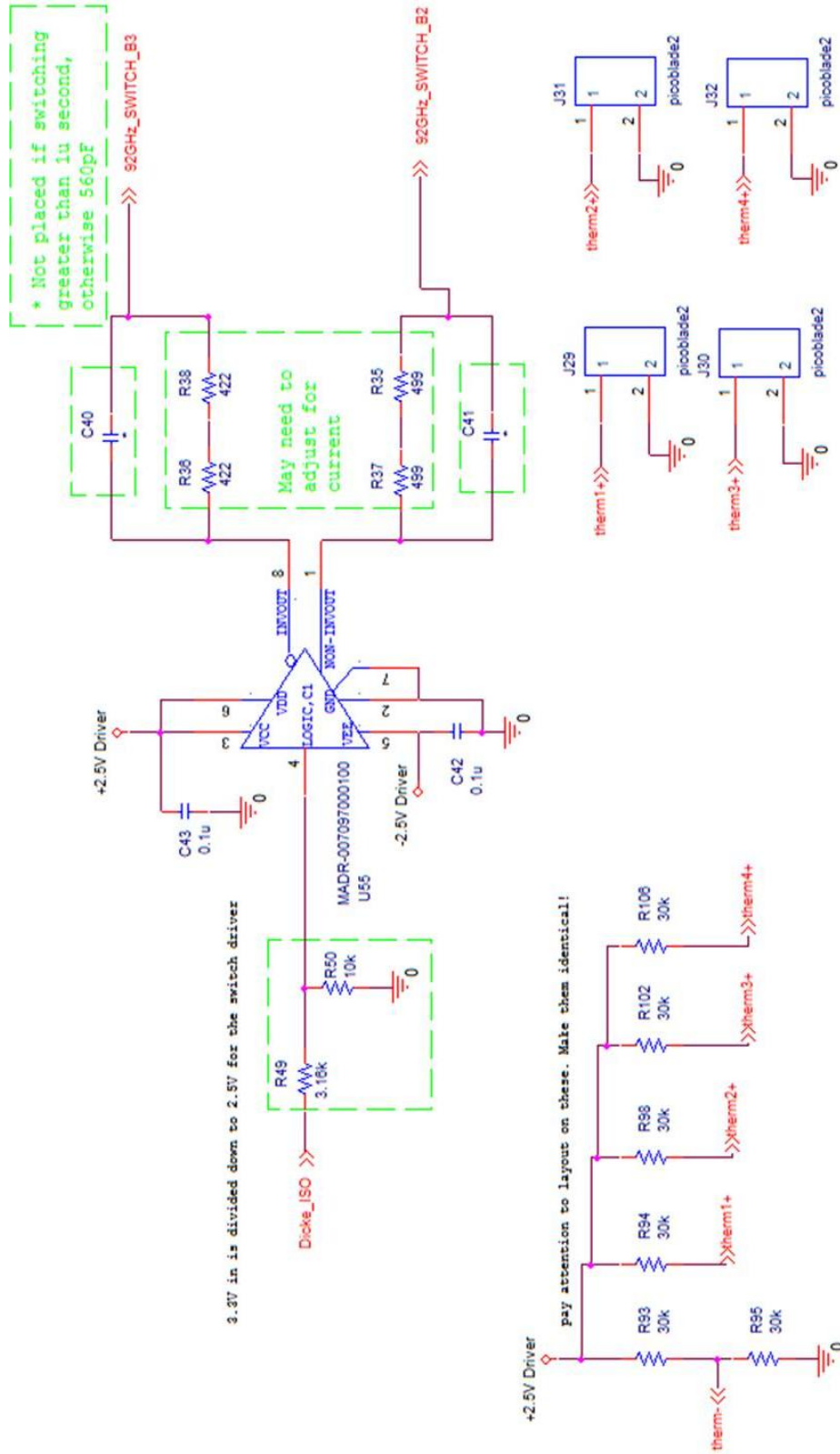


Figure G.5: Page 4 of data acquisition PCB.

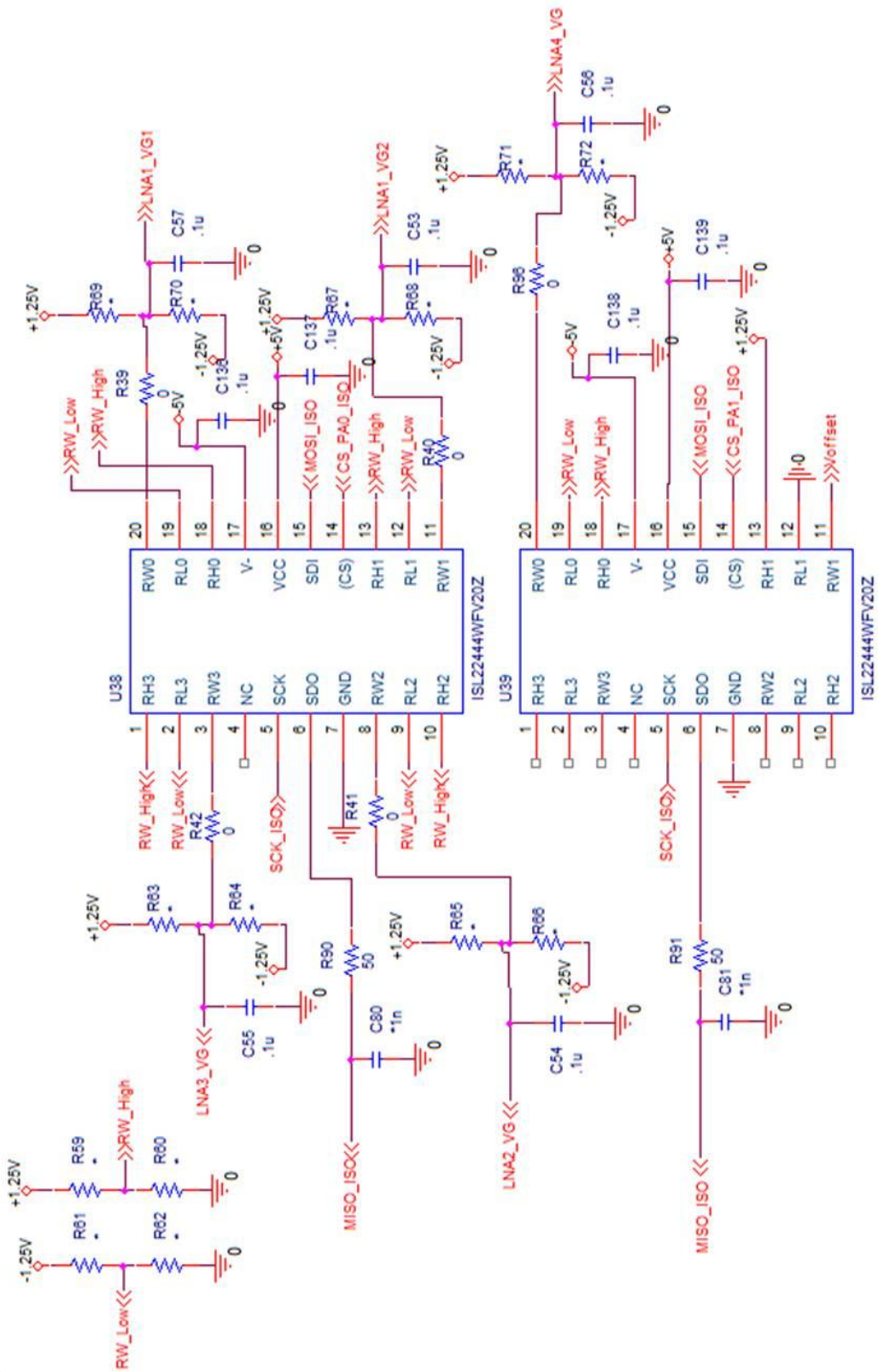


Figure G.6: Page 5 of data acquisition PCB.

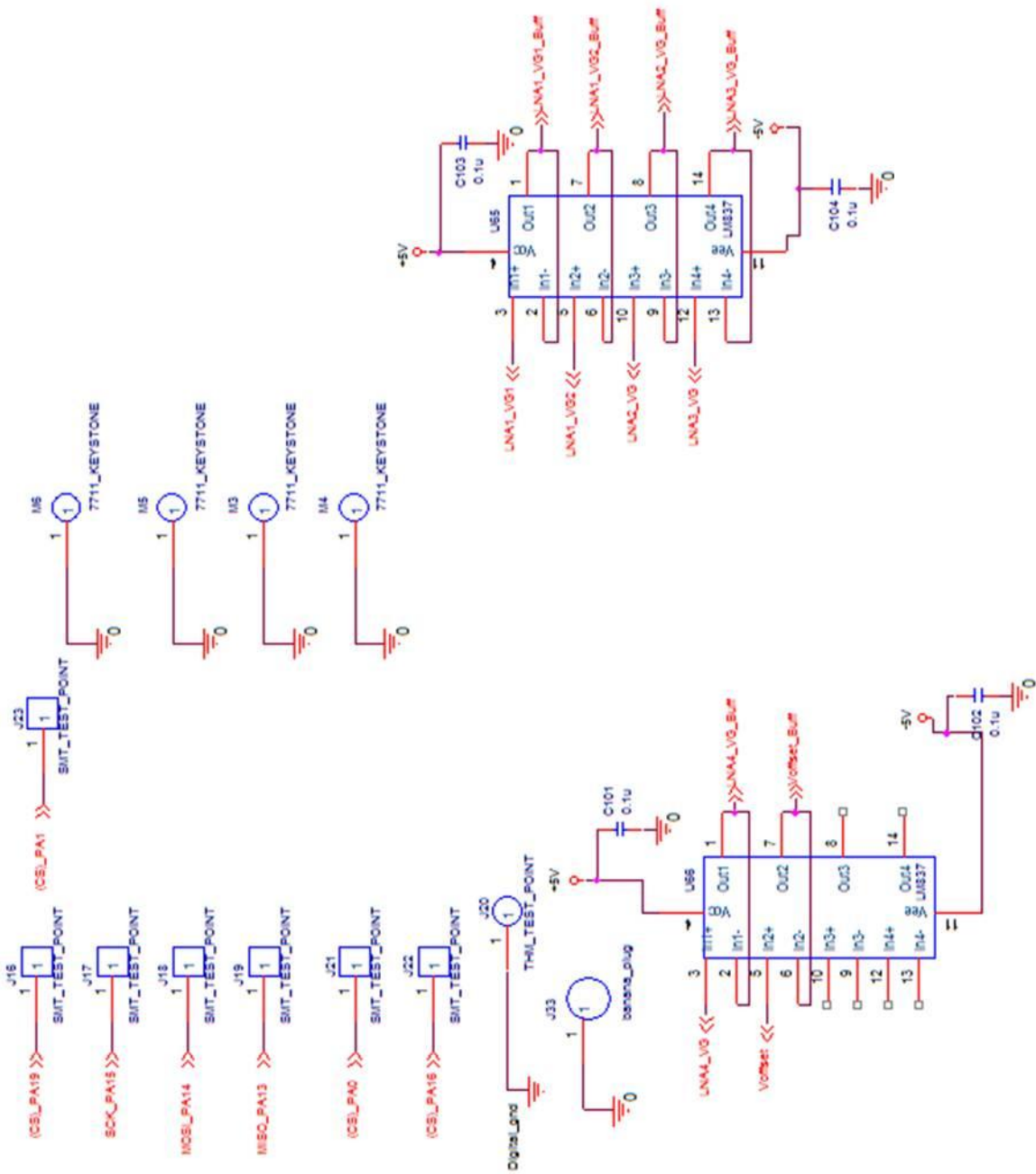


Figure G.7: Page 6 of data acquisition PCB.

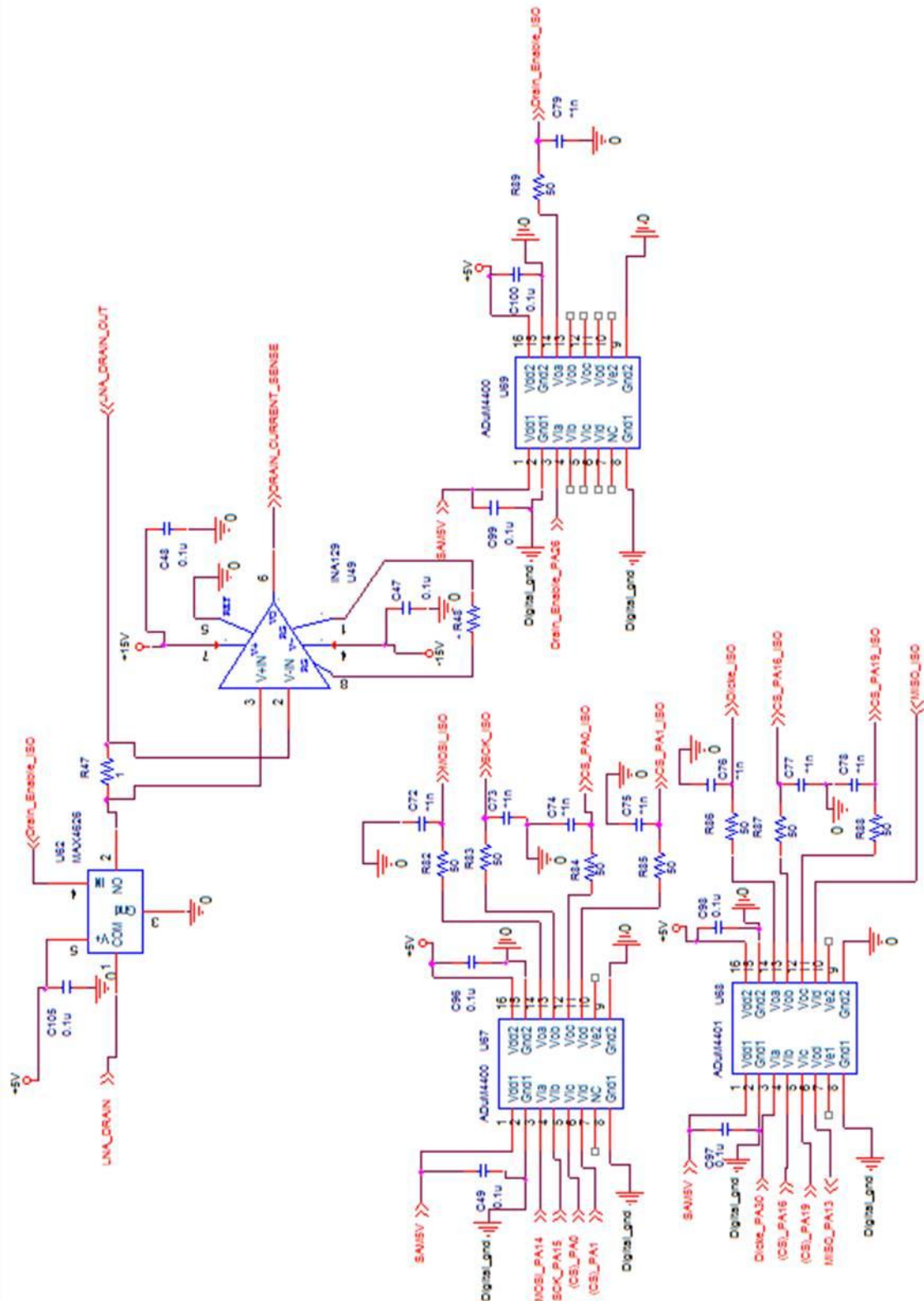


Figure G.8: Page 7 of data acquisition PCB.

List of Abbreviations

T_o	290 K
ACT	Advanced Component Technology
AMSU	Advanced Microwave Sounding Unit
ADC	Analog to Digital Converter
T_A	Antenna Temperature
ATP	Applied Thin Film
B	Bandwith
CSU	Colorado State University
CPW	Coplanar waveguide
ESD	Electrostatic Discharge
T_e	Equivalent temperature
ENR	Excess Noise Ration
$\Delta G/G$	Gain Variations
GSG	Ground-Signal-Ground
HEMT	High Electron Mobility Transistor
τ	Integration Time
IF	Intermediate Frequency
JPL	Jet Propulsion Laboratory
KaRIN	Ka-band Radar Interferometer
LO	Local Oscillator
LNA	Low Noise Amplifier
MHS	Microwave Humidity Sounder
MSL	Microwave Systems Laboratory
MMIC	Monolithic Microwave Integrated Circuits
MCM	Multi-Chip Module
NASA	National Aeronautics and Space Administration
NRC	National Research Council
PML	Perfectly Matched Layer
T_{ph}	Physical Temperature
PID	Proportional, Integral, and Differential
RF	Radio Frequency
NEAT	Radiometric Resolution
TPW	Total Precipitable Water
TREC	Receiver Temperature
TREF	Reference Temperature